REPORT DOCUMENTATION PAGE

Public reporting burden for this collection of information is estimated to average 1 hour per response, including the time for reviewing instructions, searching existing data sources, gathering and maintaining the data needed, and completing and reviewing the collection of information. Send comments regarding this burden estimate or any other aspect of this collection of information, including suggestions for reducing this burden, to Washington Headquarters Services, Directorate for Information Operations and Reports, 1215 Jefferson Davis Highway, Suite 1204, Arlington, VA 22202-4302, and to the Office of Management and Budget, Paperwork Reduction Project (0704-0188), Washington, DC 20503.

1. AGENCY USE ONLY (Leave blank)	2. REPORT DATE	3. REPORT TYPE AND DATES COVERED
	July 1996	

4. TITLE AND SUBTITLE

Interactions of a Quasi-Two-Dimensional Vortex with a Stationary and Oscillating Leading-Edge

5. FUNDING NUMBERS

6. AUTHOR(S)

Rhett William Jefferies

7. PERFORMING ORGANIZATION NAME(S) AND ADDRESS(ES)

Lehigh University

8. PERFORMING ORGANIZATION REPORT NUMBER

96-027D

9. SPONSORING/MONITORING AGENCY NAME(S) AND ADDRESS(ES)

DEPARTMENT OF THE AIR FORCE
AFIT/CI
2950 P STEET, BLDG 125
WRIGHT-PATTERSON AFB OH 45433-7765

10. SPONSORING/MONITORING AGENCY REPORT NUMBER

11. SUPPLEMENTARY NOTES

12a. DISTRIBUTION/AVAILABILITY STATEMENT

Unlimited

DISTRIBUTION STATEMENT A
Approved for public release
Distribution Unlimited

12b. DISTRIBUTION CODE

13. ABSTRACT (Maximum 200 words)

19960809 050

14. SUBJECT TERMS

15. NUMBER OF PAGES

165

16. PRICE CODE

17. SECURITY CLASSIFICATION OF REPORT	18. SECURITY CLASSIFICATION OF THIS PAGE	19. SECURITY CLASSIFICATION OF ABSTRACT	20. LIMITATION OF ABSTRACT

DISCLAIMER NOTICE

UNCLASSIFIED

Technical Report
distributed by

**DEFENSE
TECHNICAL
INFORMATION
CENTER**

DTIC Acquiring Information-
Imparting Knowledge

Cameron Station
Alexandria, Virginia 22304-6145

UNCLASSIFIED
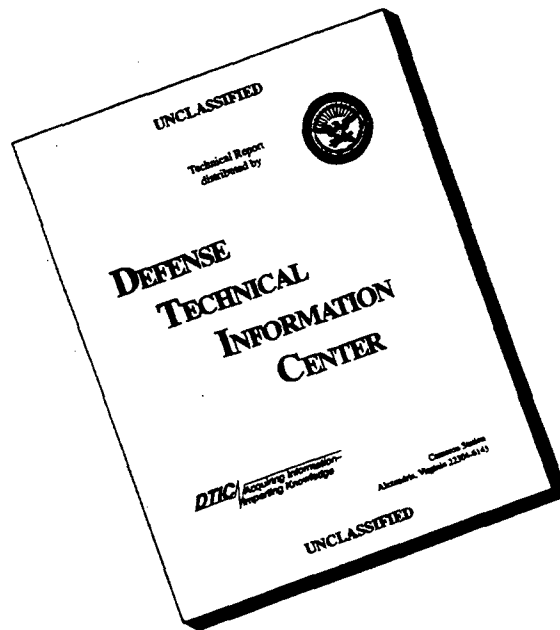
THIS DOCUMENT IS BEST
QUALITY AVAILABLE. THE
COPY FURNISHED TO DTIC
CONTAINED A SIGNIFICANT
NUMBER OF PAGES WHICH DO
NOT REPRODUCE LEGIBLY.

Interactions of a Quasi-Two-Dimensional Vortex
with a Stationary and Oscillating Leading-Edge

by
Rhett William Jefferies

Presented to the Graduate and Research Committee
of Lehigh University
in Candidacy for the Degree of
Doctor of Philosophy

in
Mechanical Engineering

Lehigh University

July, 1996
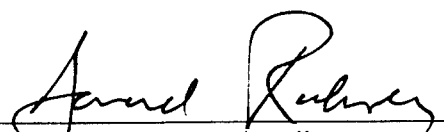
Approved and recommended for acceptance as a dissertation in partial fulfillment of the requirements for the degree of Doctor of Philosophy.
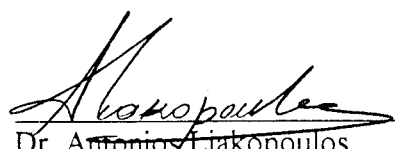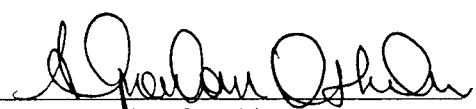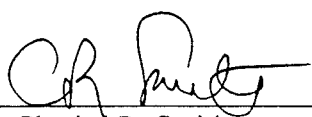
Dissertation Director
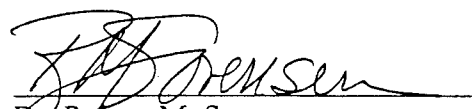
COMMITTEE MEMBERS

Dr. Donald O. Rockwell
Committee Chair

Dr. Antonios Liakopoulos

Dr. Alparslan Oztekin

Dr. Charles R. Smith

Dr. Robert M. Sorensen

ii

ACKNOWLEDGMENTS

TABLE OF CONTENTS

LIST OF FIGURES

xiv

ABSTRACT

Interactions of a quasi-two-dimensional vortex with a stationary and oscillating leading-edge were examined using a scanning laser version of high-image-density particle image velocimetry (PIV). The incident vortex street was generated by sinusoidal oscillation of an airfoil located upstream of the leading-edge. The reduced frequency of vortex convection and the oscillation of the leading-edge were equal, allowing the phase shift between them to be varied independently. At the lower of two Reynolds numbers, a well resolved time sequence of the interactions was obtained.

PIV images provide the first quantitative description of the edge interaction, employing instantaneous vorticity distributions and streamline patterns to reveal new topological features. These include the approach, deformation and splitting of an incident clockwise vortex, and the generation of tip and surface vortices on the lower surface of the stationary leading-edge.

Six stages of vortex development along the lower surface were also defined, including splitting of the tip vortex. The development of the tip vortex in the first three stages was found to depend more on the incident flow field and the resulting flux of vorticity from the upper surface. In the latter three stages, development depended more upon the mutual interaction of the tip and surface vortices with the lower surface.

Compared to interactions with a stationary leading-edge, oscillation of the leading-edge at $\phi=0°$ with respect to the incident vortex produced tip and surface vortices of much higher circulation. When the leading-edge oscillated at $\phi=180°$, no tip or surface vortices were formed. This suggests the induced force on the edge will be much greater when the leading-edge oscillates at $\phi=0°$, and substantially reduced when the edge oscillates at $\phi=180°$, relative to the incident vortex. Consequently, variation of the phase angle of the leading-edge oscillation may be used to control unsteady loading and noise generation resulting from vortex interactions.

1

1.0 INTRODUCTION

Interactions of coherent flow structures with airfoils and blades occur in a variety of flow configurations. Rotating blades pass through the wakes of upstream blading in turbomachinery while aircraft wings and helicopter blades collide with vortices generated by upstream lifting surfaces. In a wind park environment, wind turbine blades operate within turbulent wakes from upstream obstacles (Kelly, 1993).

When a vortex interacts with a surface, it induces pressure fluctuations on the surface, which serve as the origin of unsteady loading and noise generation. The unsteady loads may be of the same order as, or even surpass, steady loads and can lead to early failure of an airfoil or blade. The associated noise generation often exceeds design limits, and severely threatens system operation. Moreover, the overall system performance, based on steady-state criteria, is often degraded. An understanding of the flow physics of these vortex-surface interactions is therefore crucial before techniques can be devised to control the effects of these interactions.

1.1 Motivation for Research

Coherent flow structures exist in both two- and three-dimensional flows. In the case of helicopters, a vortex produced at the tip of an advancing blade will interact with oncoming blades in several ways, depending on flight conditions and the azimuth angle of the blade with respect to the vortex shed from the tip (figure 1.1). These interactions have been characterized as "parallel" or "oblique", representing quasi-two-dimensional and three-dimensional interactions, respectively. Parallel interactions are known to cause the most intense unsteady pressure fluctuations on rotating helicopter blades. Current

2

techniques intended to diminish these effects on helicopter blades include changing blade tip configurations and imposing high frequency pitch oscillations to the blade as it rotates (Hardin and Lamkin, 1987). Although it has been reported that these techniques have had limited success in reducing noise, the underlying reasons for the success have not been entirely understood.

This study focuses on quasi-two-dimensional or "parallel" interactions in order to more fully understand the detailed flow structure and mechanisms causing the most severe interactions and investigates the effectiveness of oscillating the airfoil to alter these interactions. Once the parameters which strongly affect these parallel interactions are known, the underlying physics can be better understood and used to design viable techniques of controlling the unsteady loading and noise in two- and three-dimensional vortex interactions occurring in many applications. This includes for example, attenuating aircraft tail buffeting or reducing wind turbine blade noise.

Previous analytical, numerical and experimental investigations have identified certain features affecting vortex interactions. The physics of the simplest case of a vortex interacting with an infinite wall will be presented first in section 1.2. Section 1.3 discusses vortex development and the resulting interactions on an airfoil undergoing dynamic stall. Investigations of vortex-stationary edge and vortex-oscillating edge interactions are summarized in sections 1.4 and 1.5, respectively. Several techniques of characterizing flow structures and extracting useful information from very complicated flows are addressed in section 1.6. A summary of the significant parameters affecting vortex interactions with a leading-edge is presented in section 1.7, followed by an overview of the research objectives in section 1.8, and finally, an outline of the dissertation in section 1.9.

1.2 Vortex-Wall Interactions

In external and internal aerodynamics, complex flows often arise from the viscous response of a vortex interacting with a boundary layer. As reviewed by Doligalski, Smith and Walker (1994) (DSW), the general features of this interaction can be more simply modeled by a two-dimensional, clockwise-rotating vortex, with Reynolds number ($Re_V=\Gamma/2\pi\nu$), convecting in a uniform flow (to the right) above an infinite wall. According to inviscid theory, in the absence of a uniform flow the vortex will convect to the left with self-induced speed $V_s=\kappa/2a$, where κ is the vortex strength ($\Gamma = 2\pi\kappa$) and a is the distance of the vortex center above the wall. Adding the uniform flow results in non-dimensional vortex convection speed $\alpha = V_c/U_0$, where U_0 is the uniform free stream and $V_c = U_0 - V_s$. The authors show $\alpha=0.75$ is the limiting value for a localized stagnation point to occur on the surface below the vortex due to the local adverse pressure gradient. For $\alpha<0.75$, reverse flow on the surface below the vortex (in the laboratory reference frame) will occur, leading to a viscous response of the boundary layer, or separation. In the boundary layer scale, this separation is due to a streamwise compression of fluid particles near the point of zero shear above the wall, requiring an elongation in the normal direction (for an incompressible fluid). This elongation focuses the local boundary layer vorticity into a very thin spike which erupts toward the external, inviscid flow field. On the scale of the external flow, this eruption appears as a sharply focused concentration of vorticity near the surface that will imminently shoot into the freestream. Although difficult to visualize, this eruption has been visualized in a few experiments of vortex-induced separation and numerically using Lagrangian coordinate formulations.

Using a moving reference frame, DSW show a primary two-dimensional vortex of sufficient strength and proximity to the wall (proportional to α) will induce an unsteady

4

viscous-inviscid interaction of the surface layer (separation) leading to the ejection of a secondary vortex at the wall (sometimes tertiary vortices) of opposite sense and comparable in strength to the primary vortex. This secondary vortex will also interact with the primary vortex in an inviscid manner, significantly altering its motion.

The mechanisms which have been described for 2-D vortex-induced, viscous-inviscid interactions also occur for 3-D interactions. Primary horseshoe vortices formed by the flow past a juncture of a wall and body induce the formation of secondary vortices which will be ejected from the surface by an eruption similar to that described for dynamic stall. These eruptions lead to vortex roll-up and the formation of hairpin vortices near the surface. The newly-formed hairpin vortices can then induce the formation of additional hairpin vortices, becoming a self-generating mechanism.

1.2.1 Unresolved Issues

The review by DSW (1994), and the works cited therein provide insight into vortex interactions with an infinite surface, as well as with the elliptical leading-edge of an airfoil undergoing oscillations and exhibiting dynamic stall (see section 1.3). Much of the physics associated with the flow development in the presence of an oscillating surface is not clearly understood. It is unknown how vortex development and interaction processes are affected when the airfoil surface is oscillated at varying frequencies and amplitudes.

1.3 Vortex-Surface Interactions on an Oscillating Surface Exhibiting Dynamic Stall

Much research has been conducted on dynamic stall of a pitching or oscillating airfoil. The vortex development near the leading-edge of an airfoil undergoing dynamic stall is similar to the flow development during some vortex-stationary edge interactions

5

in which a secondary vortex is shed. Therefore, the advances made in understanding dynamic stall and some useful analysis techniques may help to clarify issues pertaining to vortex interactions with stationary and oscillating leading-edges.

During the pitch-up of an airfoil, well after passing the static stall angle, DSW (1994) review vortex-induced separations, similar to those arising during vortex-wall interactions, that occur during a situation known as dynamic stall. In both experimental and numerical investigations, a dynamic stall vortex is formed initially near the leading-edge of an airfoil within the boundary layer which, when visualized using streamlines in a moving reference frame, appears as a detached, recirculating eddy. When the chord Reynolds number is low or moderate, the eddy grows smoothly, deforming the flow near the leading-edge until the eddy becomes the primary dynamic stall vortex, eventually reaching a threshold in strength, such that a secondary vortex is induced near the wall, similar to the vortex-induced separation on an infinite wall described earlier. Subsequent to the formation of the secondary vortex, in the region between the secondary and primary vortices, an eruption of surface flow occurs, ejecting the secondary vortex into the freestream and detaching the primary vortex from the airfoil surface and initiating dynamic stall.

DSW (1994) indicate that if the Reynolds number is high enough, two conditions will be established just upstream of the initial recirculating eddy: 1) a zero vorticity line and 2) a local zone of adverse pressure gradient. These will cause an eruption and subsequent roll-up of surface vorticity to form the dynamic stall vortex, rather than from the steady growth of the recirculating eddy as in lower Reynolds number situations. The remainder of the dynamic stall process continues with the formation of a secondary vortex, as described above. In high Reynolds number flows, numerical algorithms cannot yet be used to visualize the formation of the dynamic stall vortex.

6

Using particle image velocimetry (PIV), Shih, Lourenco & Krothapalli (1995) report the same flow development on the upper surface of a NACA 0012 airfoil that is pitched at a constant non-dimensional pitch rate $\alpha+ = \alpha C/U_\infty = 0.13$. they characterize the recirculating eddy near the leading-edge as arising from a shear layer driven by an adverse pressure gradient in the leading-edge region, and not from reverse flow originating at the trailing-edge. Vorticity contours of this shear layer show small-scale structures that typically occur in an unstable shear layer. These structures subsequently coalesce into a larger primary vortex (negative vorticity) which later forms a secondary vortex (positive vorticity) with 35% of the primary vortex circulation.

In a numerical study of dynamic stall of a sinusoidally oscillating airfoil, Tuncer, Wu & Wang (1990) found that by increasing the reduced frequency of oscillation, the leading-edge vortex formation is delayed until higher angle-of-attack and changes the hysteresis loop of the loading. For a pitching airfoil, Acharya and Metwally (1992) determined experimentally that the leading-edge vortex development depends significantly on airfoil pitch rate with the magnitude of the unsteady pressure and vorticity flux increasing with increasing pitch rate. In a numerical study, Visbal and Shang (1989) found the same flow structure dependence and corresponding pressure fluctuations and maximum lift on pitch rate as well as a dependence on pitch axis location. Visbal and Shang show, for a fixed pitch axis downstream of the leading-edge, that the formation of the leading-edge primary vortex is delayed to a higher geometric angle-of-attack and usually results in higher maximum lift when the non dimensional pitch rate is increased from 0.1 - 0.6. For a fixed pitch rate, the leading-edge vortex formation was also delayed as the location of the pitch axis was moved downstream. This trend was reported by Visbal and Shang to be related to an effective angle-of-attack α_{eff} which depends on the leading-edge velocity, induced by the pitching motion. Therefore, as the pitch axis moves downstream, α_{eff} is reduced for a given geometric

7

angle-of-attack and pitch rate. Visbal and Shang show very similar leading-edge vortex flow structure at the same α_{eff} for different geometric angles-of-attack and pitch axis locations. This is important since in general, Visbal and Shang found that when α_{eff} is increased, for a given pitch rate, higher pressure gradients near the leading-edge result, leading to higher vorticity flux and lift.

1.3.1 Unresolved Issues

The dynamic stall investigations discussed above were all performed on an elliptical leading-edge. Separation processes and the corresponding flow development for an airfoil with a sharp leading-edge, involving a fixed separation point, have not been investigated. From a more fundamental standpoint, the reason for the increase in lift and the dependence of the flow structure on pitch rate / oscillation frequency is not known. Furthermore, possible instabilities formed in the shear layer from the leading-edge and their role in the subsequent formation of primary vortices have not been characterized. Most important is the fact that flow complexities introduced by an oscillating or pitching wing in presence of an incident (impinging) vortex have not been addressed in a quantitative sense. The relevant issues for this type of interaction are addressed in the next two sections.

1.4 Vortex-Stationary Edge Interactions

In practice, there are many factors and unsteady effects that influence the type of vortex interaction. However, previous investigations first sought to understand the parameters affecting the simpler case of a vortex impinging upon a stationary body. Due to the varied flow configurations that produce these interactions, a wide range of

8

techniques have identified the same significant parameters that influence the magnitude of the resulting unsteady pressure fluctuations.

An array of non-decaying, discrete vortices approaching and convecting along on a semi-infinite flat plate was theoretically modeled by Rogler (1978) assuming 2-D, incompressible, inviscid, parallel flow to determine the two-dimensional unsteady, instantaneous flow field both upstream of the plate as well as in the vicinity of the plate. Rogler emphasizes that solutions are not valid for the very thin regions of the boundary layer or at the leading-edge. However, the singularity that exists at the leading-edge can be resolved by increasing the radius of curvature of the edge, or by introducing flow separation.

Rogler (1978) shows the magnitude of the pressure fluctuation ($|p'|$) varies with three parameters: proximity to the plate leading-edge; scale (λ) of the incident vortex; and transverse offset (δ) of the incident vortices relative to the plate. As the incident vortices interact with the leading-edge, $|p'|$ is greatest at the leading-edge and diminishes with distance from the edge. The pressure fluctuation magnitude also increases with increasing vortex scale and with decreasing transverse offset. Moreover, it is maximum when the plate bisects the oncoming vortex. In addition, Rogler identified three types of interaction streamline patterns that as a function of transverse offset.

Gursul and Rockwell (1990) used pressure measurements and qualitative flow visualization of a vortex street impinging upon an elliptical leading-edge to show how the magnitude of the pressure field is influenced by the type of vortex interaction. Several classes of vortex-airfoil interaction were identified as a function of scale (λ) and transverse displacement (δ). Dependence on δ was similarly noted in the experimental results obtained by Ziada and Rockwell (1982), Kaykayoglu and Rockwell (1985), Booth (1990), Wilder (1992) and Horner (1994). Horner's study included both two- and three-dimensional (streamwise) vortex interactions with a blade. Each reported

9

maximum pressure loading when the incident vortex impinged directly on the leading-edge; the magnitude of the loading further increased when the leading-edge was oriented at larger angle-of-attack.

The analysis of Rogler (1978) indicates that the largest pressure fluctuations occur at the leading-edge of the plate. In the experiments referenced above, the induced pressure at the edge varied with the type of leading-edge, i.e. rounded or sharp. Kaykayoglu and Rockwell (1985), referred to hereafter as KR, identified three features of the vortex-interaction process on a sharp leading-edge . First the incident vortex is distorted and severed, then a secondary vortex is shed from the tip of the leading-edge, followed by "sweeping" of the flow about the tip from the upper to lower surface of the airfoil. Ziada and Rockwell (1982) found the amplitude of the induced force on the sharp leading-edge is strongly dependent on the occurrence of secondary vortex shedding. KR similarly noted secondary vortex shedding and tip "sweeping" caused the pressure field to become wave-like with a maximum amplitude at the tip and different phase speeds along the upper and lower surfaces of the sharp leading-edge.

Gursul and Rockwell (1990) and Booth (1990) did not observe secondary vortex shedding on a rounded, elliptical leading-edge for an incident vortex with a scale much smaller than the chord of the airfoil. However, Nakagawa (1988) and Wilder (1992) both found secondary vortex shedding on an elliptical leading-edge. Using incident vortices of scale on order of the airfoil chord, Nakagawa determined that incident vortex circulation and scale diminish when the secondary vortex forms on the leading-edge; the circulation of the secondary vortex is reduced when the vortex begins to translate along the airfoil surface. Wilder shows a counter-clockwise rotating incident vortex, with a scale less than the airfoil chord, will generate a secondary vortex at the leading-edge of an airfoil at an angle-of-attack $\alpha = 10°$. It convects with the incident vortex.

Rockwell (1984) indicates that the character of the incident vortex, the mean flow distortion and leading-edge pressure gradients contribute to the formation of a secondary vortex. These features are characteristic of a broader class of vortex-wall interactions, which are reviewed in more detail in section 1.2. Doligalski, Smith & Walker (1994) and Smith, Walker, Haidari & Sobrun (1991) show that close proximity of a vortex to a wall will induce a local adverse pressure gradient in the boundary layer, causing an eruption of surface fluid which leads to secondary vortex formation. These studies suggest that secondary vortex shedding could occur on any airfoil leading-edge given the proper combination of incident vortex parameters (scale, transverse offset) and leading-edge pressure distribution.

1.4.1 *Unresolved Issues*

The determination of instantaneous velocity and vorticity over the entire flow field; direct correlation of instantaneous pressure, velocity and vorticity; assessment of the effects of leading-edge shape, and a determination of viable control concepts have not yet been addressed or resolved. In general, the dependence of the magnitude of pressure fluctuations induced at the leading-edge on the significant parameters summarized above needs to be assessed **quantitatively** for two- and three-dimensional vortex-blade interactions. In assessing this dependence, characteristic types of vortex interactions, which represent specific pressure fluctuation behaviors or "signatures", should be identified.

1.5 Vortex-Oscillating Edge Interactions

Inherent instabilities in shear layers that exist for example, within a planar jet or mixing layer, are amplified by the upstream influence of a stationary edge downstream

and cause flow fluctuations at a predominant frequency f_0^*, leading to the formation of vortices at a specific distance downstream. This upstream influence is determined by the unsteady pressure field acting on the edge. Staubli and Rockwell (1987) and Kaykayoglu (1989) employed this method of generating vortices and studied the effects of edge oscillation on the resulting vortex interactions with the edge. Staubli and Rockwell found that when the downstream edge is oscillated with a given excitation frequency f_e, two instability waves co-exist in a planar jet, one at a self-excited frequency f_0, usually different from f_0^*, and one at the excitation frequency f_e (see fig. 1.2), producing two corresponding components of fluctuating pressure on the edge with amplitudes: p_0 and p_e. Furthermore, when f_e is varied, from zero to over four times f_0^*, and the oscillation amplitude is small, a small frequency range exists near f_0^* where the two frequencies f_e and f_0 are phase-locked and $f_e = f_0$. In this "synchronized" frequency zone, Staubli and Rockwell note $0 < p_0 < p_e$. When the edge oscillation amplitude passes a certain threshold, synchronization occurs within a larger frequency range, but f_e $\neq f_0$ and $p_0 \rightarrow 0$, while is p_e amplified due to resonance.

Within the synchronization range, as described by Staubli and Rockwell (1987), the phase angle ϕ between the fluctuating pressure amplitude p_e and the edge displacement varies substantially with changes in f_e. Moreover, Staubli and Rockwell identify the frequencies of maximum energy transfer from the flow to the edge (damping) as well as from the edge to the flow (excitation) within the synchronization range for the larger oscillation amplitude. The corresponding flow structure, as shown by qualitative dye flow visualization, at the "damping" frequency shows a delay in the roll-up of the primary vortex near the oscillating edge when compared to the corresponding flow structure of the stationary edge. Opposite to this effect, the growth of the flow instability is accelerated at the "exciting" frequency as evidenced by the early primary vortex roll-up.

12

When the excitation frequency increases beyond the synchronization range, dye flow visualization results show the wavelength and vortex scale of the instability wave become smaller while the roll-up of the vortices occurs sooner, much closer to the jet nozzle, indicating energy transfer from the edge to the flow. As f_e continues to increase, vortices exhibit different pairing and levels of coalescing. In many of the flow visualization images, secondary vortex formation is evident, particularly at higher excitation frequencies.

Kaykayoglu (1989) studied the effect of edge oscillation in the wake of an unstable mixing layer by varying both the frequency and amplitude of the edge oscillation and identified several classes of upstream vortex development and corresponding edge interactions. In each of the identified classes, vortex development was repeatable and "phase-locked" to the motion of the edge. For an excitation frequency range $1/2f_0^* < f_e < f_0^*$, where f_0^* is the instability frequency associated with a stationary edge, the scale and wavelength of the vortices are greatest, becoming smaller as f_0^* is approached. In all the vortex interactions, secondary vortices were produced on the lower surface but with distinct flow structure, which Kaykayoglu (1989) showed to depend on the relative phase of the arrival of the incident vortex to the position of the oscillating edge. This phase angle depends on excitation frequency. The scale of the secondary vortices was also shown to increase with increasing oscillation amplitude.

1.5.1   Unresolved Issues

It is important to realize that the vortex-oscillating edge investigations were conducted employing an inherently unstable flow and upstream feedback to generate the vortices and that the above mentioned parameters are specific to that case. However, it is probable that given a different flow field that does not depend on upstream feedback for vortex generation, that the last four parameters will still be significant. Consequently,

13

it is unknown how the edge oscillation parameters of amplitude, frequency and phase will affect vortex interactions for vortices that are generated sufficiently far upstream so as to not depend on feedback from the edge. This type of flow would also allow the separation of frequency and phase into two independent parameters, which was not feasible in the above mentioned investigations.

1.6 Classification of Flow Structure

In the preceding sections important results of previous investigations were reviewed which helped to provide insight into the nature of complex flows. Many of these researchers, and others in parallel, have developed techniques of describing and classifying the flow field in an attempt to identify key flow features and processes and analyze them in a simplified manner. Three particular methods are reviewed here: vorticity flux, local circulation and two-dimensional streamline topology.

1.6.1 Vorticity Flux

Reynolds and Carr (1985) view vorticity as the key to understanding the main features of unsteady, separated flows that are driven by some method of forced oscillation. Development of the vorticity field can be described as a balance between vorticity generation and transport. Vorticity can only be produced in the presence of a solid surface by three means: 1) by tangential surface acceleration; 2) by a pressure gradient; and 3) by transpiration of fluid through a surface by sucking or blowing. Consequently, a net vorticity flux through the surface is simply the sum of these three contributions:

$$-v\frac{\partial \Omega}{\partial y} \quad = \quad -\frac{\partial U_s}{\partial t} \quad -V\Omega \quad -\frac{1}{\rho}\frac{\partial P}{\partial x}$$

| Vorticity Flux | Surface Acceleration | Transpiration | Pressure Gradient |

Here x is tangential and y is normal to the surface; U_s is the surface tangential speed, V is the transpiration velocity and Ω is the spanwise mean vorticity.

There are several examples of researchers using vorticity flux to determine the flow physics. Emphasis has been on evaluating the flux in regions away from the surface, which is, of course, a consequence of the foregoing sources of vorticity flux. Sheridan, Lin & Rockwell (1995) used vorticity flux measurements obtained from PIV data to establish the flow past a cylinder near a free-surface is characteristic of a free-jet. From this result, it may be deduced that the free-surface will distort to produce sufficient vorticity to match that generated by the cylinder. Shih and Ho (1994) employed vorticity flux concepts to determine the instants of leading-edge vortex attachment and break-away in the cycle of an oscillating free stream past a stationary airfoil at an elevated angle-of-attack. Experimental results by Acharya and Metwally (1992) indirectly evaluated peaks of surface vorticity flux near the leading-edge by differentiating the unsteady surface pressure. These peaks identify sources of vorticity generation on the airfoil surface located within the first 10% of the airfoil chord, some of which apparently feed the primary and secondary dynamic stall vortices.

1.6.2 Local Circulation

The vorticity balance equation described by Reynolds and Carr (1985) is

$$\frac{d}{dt}\iint \Omega \, dx\, dy \quad = \quad \int_a^b F_x \, dy \quad - \int_c^d F_x \, dy \quad + \int_a^c\left(-v\frac{\partial \Omega}{\partial y}\right)dx$$

| Accumulation | Flux In | Flux Out | Flux Generated on Surface |

for a control volume shown in figure 1.3. The segment ac of the control volume is on the body surface. The accumulation term on the left could also be considered as the time

15

rate of change of the circulation of the control volume. Therefore, the circulation of the control volume is a local value within a specific spatial region of the flow. If a large number of control volumes of infinitesimal size are defined within a flow field, the distributions of their local circulation will yield a spatial variation of vorticity distribution. In an unsteady flow, the time rate of change of this local circulation distribution will yield the accumulation term on the left side of the vorticity balance equation for each local circulation cell or control volume. From this, one may determine the location of vorticity generation on a surface to within the width of a circulation cell.

Shih and Ho (1994) applied this technique by defining seven local circulation cells on the upper surface of an airfoil in an sinusoidally varying freestream and calculated the local circulation of each cell for the entire cycle. Shih and Ho were consequently able to show the local circulation to be maximum near the leading-edge and that the circulation increases with time over the entire upper surface of the airfoil. By making use of the vorticity balance equation, Shih and Ho determined the circulation increase in attached flow is due solely from the imposed transient pressure gradient and that the variation of the vorticity distribution should be linearly proportional to the external velocity of the boundary layer. In the separated case, Shih and Ho find that the convected vorticity generated at the leading-edge dominates the flow.

1.6.3 Topology of Two-Dimensional Streamline Patterns

Chong, Perry & Cantwell (1990) describe how complex three-dimensional flows can be more easily interpreted by indentifying elemental flow patterns of streamlines projected on a two-dimensional plane. These elemental flow patterns consist of critical points in the flow where all three velocity components are zero and the streamline slope is indeterminate. For flows that can be locally linearized in space, a three-dimensional set of first-order differential equations can be written in as

16

$$\begin{pmatrix} \dot{x}_1 \\ \dot{x}_2 \\ \dot{x}_3 \end{pmatrix} = \begin{bmatrix} a_{11} & a_{12} & a_{13} \\ a_{21} & a_{22} & a_{23} \\ a_{31} & a_{32} & a_{33} \end{bmatrix} \begin{pmatrix} x_1 \\ x_2 \\ x_3 \end{pmatrix} \quad \text{or } \dot{x} = A \cdot x$$

where a_{ij} are real constants. For fluid flow away from no-slip boundaries, a_{ij} are the elements of the rate-of-deformation tensor $\dfrac{\partial \dot{x}_i}{\partial x_j}$ evaluated at $(x_1, x_2, x_3) = (0,0,0)$; near boundaries a_{ij} become higher order quantities related to gradients of vorticity and pressure. The local behavior of the solution of these linearized equations depends on the eigenvalues of A. The characteristic equation can be written in the form $\lambda^3 + P\lambda^2 + Q\lambda + R = 0$, where P, Q and R are the invariants of the matrix A. The critical point flow topology can be classified by the values of these invariants.

Examples of possible critical point topologies as described by Perry and Steiner (1987, Part I) are shown in figure 1.4. Figure 1.5 is reproduced from Vorobieff (1996) and shows possible critical point topologies for incompressible flow, which requires the invariant P = 0. In this case, Chong, Perry and Cantwell (1990) emphasize in particular, that a center topology can only be obtained if the flow is two-dimensional. Furthermore, on the Q-R plane, all possible no-slip critical points must lie on the line R=0. Other critical points in this plane also indicate physical three-dimensional flow phenomena. Perry and Steiner (1987, Part I) relate for example, a stable focus indicates axial stretching of a vortex tube, while an unstable focus represents axial compression. Closed bifurcation lines or limit cycles may be classified as unstable or stable and denote a transition between stable and unstable foci. Flow stagnation points will appear as either saddle points or nodes in the streamline patterns.

These topology concepts have been used by several researchers to identify the critical points in three-dimensional flow and relate them to physical processes. In a computational study, Visbal and Gordnier (1993) noted the streamline topology in a cross plane for a streamwise vortex of a delta wing changed as the wing pitched. When

17

the core of the vortex experienced stretching and vortex breakdown occurred downstream of the cross plane, the topology showed a stable focus within a limit cycle. As the position of vortex breakdown moved upstream past the cross plane, the core of the vortex underwent axial compression and the topology showed an unstable focus and limit cycle. Topological classification has been useful in this investigation and will be discussed further in subsequent sections.

1.7 Summary of Significant Parameters

Some of those parameters listed above, for example, vortex circulation and flow Reynolds number, are shown to be significant in more than one type of flow interaction but are listed only once here. Furthermore, in the current investigation the incident vortex sheet is generated by sinusoidal oscillation of an airfoil located far enough upstream of the leading-edge to minimize the influence of upstream feedback. Consequently, the parameters of shear layer type and separation distance between the shear layer and edge are not considered significant. The relevant, significant parameters for the current study are summarized below (see fig. 1-6).

- Flow Reynolds number ($Re_c = \frac{U_\infty c}{v}$), where c is the airfoil chord length and U_∞ is the freestream velocity

- Leading-edge pressure distribution as affected by
    1) leading-edge shape
    2) effective airfoil angle-of-attack (α_{eff})

- Transverse offset between the incident vortex and the airfoil leading-edge (δ)

- Scale of the incident vortex (λ)

- Circulation of the incident vortex (Γ)

- Airfoil reduced frequency ($k = \dfrac{\omega c}{2U_\infty}$), where ω is the angular frequency in rad/sec

- Leading-edge oscillation amplitude

- Phase angle between the arrival of the incident vortex and the oscillation of the edge

1.8 Current Investigation

1.8.1 Scope

The focus of this experimental investigation is to assess the effects of leading-edge motion on the interaction with an incident vortex. However, a parametric study of the oscillation amplitude, frequency and phase is beyond the scope of this current initiative. Rather, the approach is taken of identifying the influence of phase angle on the interactions with a sharp leading-edge. Consequently, of those significant parameters listed above, only the phase angle, flow Reynolds number and effective angle-of-attack vary.

Furthermore, although the simultaneous acquisition of unsteady pressures in the leading-edge region with the instantaneous velocity field is highly desirable, it too proved to be beyond the scope of this study. Instead, a more detailed, quantitative analysis of the unsteady, instantaneous velocity and vorticity fields is accomplished using high density particle image velocimetry (PIV). These results are then compared, and a relative assessment of unsteady loading is made in accordance with the relationships defined from other investigations between unsteady pressure and the corresponding flow structure.

1.8.2 Summary of Research Objectives

The objectives for this investigation are summarized in the following:

1) Quantitatively characterize vortex interactions with a stationary and oscillating leading-edge. The time dependent flow structure for both stationary and oscillating leading-edge cases will be identified using PIV techniques. Flow development will be classified using streamline topology, contours of constant vorticity and the concepts of vorticity flux and local circulation.

2) Define relationships between identified flow structures and leading-edge oscillation and phase angle. Physical mechanisms causing the interactions for each case will be proposed.

3) Evaluate effectiveness of leading-edge oscillation and phase angle as a control technique . The physical significance of varying the phase angle will be explored and other possible methods of producing similar effects will be proposed.

1.9 Outline of Dissertation

This chapter addresses the current state of understanding of vortex-interactions with both stationary and oscillating leading-edges as assessed by previous studies. Techniques of classifying unsteady flow as a means of identifying physical processes are reviewed. Significant parameters and research objectives pertinent to this study are also summarized.

Chapter 2 describes the details of the experimental system and techniques used in this study. Chapter 3 evaluates the quasi-two-dimensional nature of the incident vortex generated upstream of the leading-edge. Chapters 4 and 5 characterize the interaction flow structure for a stationary and oscillating leading-edge, respectively. Chapter 6 compares the flow structure and development for the several cases and examines

possible physical mechanisms for the observed flow behavior. Chapter 7 summarizes the conclusions of this investigation, assesses the significance of leading-edge motion and phase for controlling vortex interactions, and finally recommends areas for further research.

Practical considerations of experimental image acquisition and data processing are discussed in the appendices.
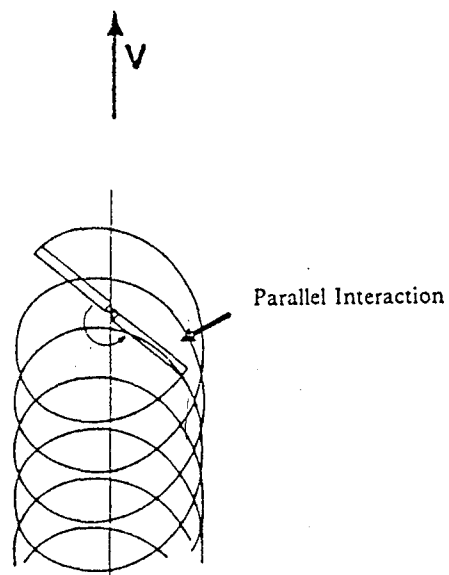
Figure 1.1: Schematic of a parallel blade-vortex interaction in a helicopter rotor (Wilder, 1992)
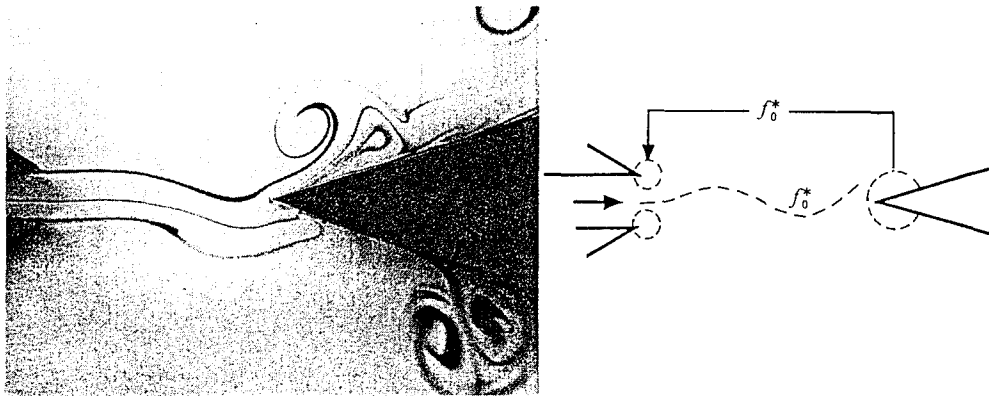
a) Self-sustained oscillations of a jet impinging upon a stationary edge.
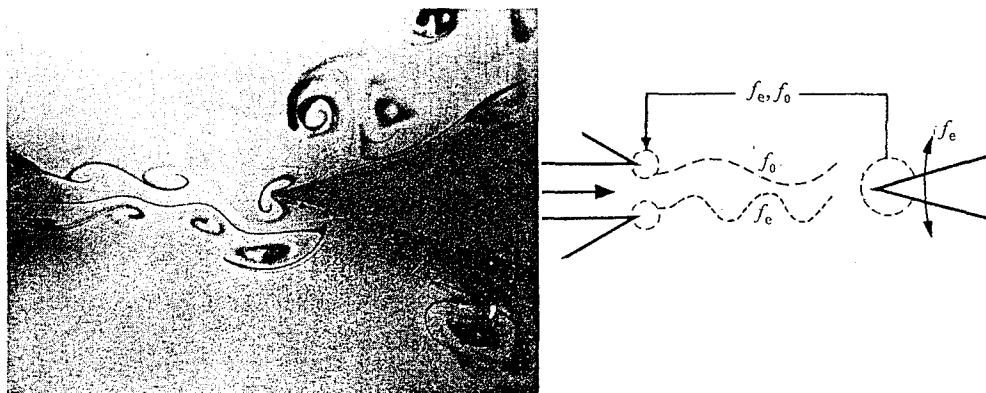
b) Jet impinging upon the oscillating edge ($f_e = 4f_0$).

Figure 1.2: Instability wave-forms for a jet impinging on a) a stationary edge and b) an oscillating edge. (Staubli & Rockwell, 1987)
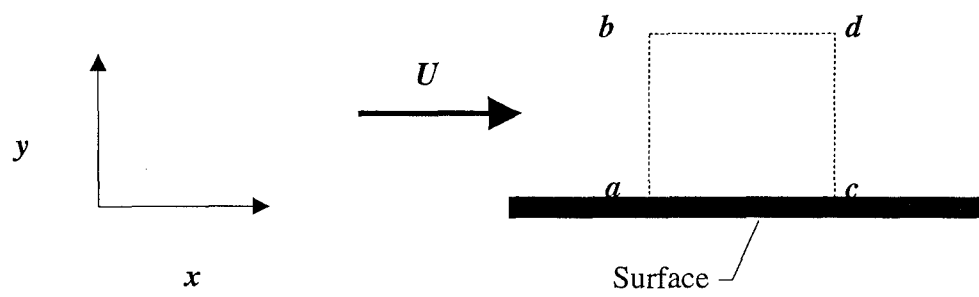
Figure 1.3: Control volume above a solid surface (Reynolds and Carr, 1985)
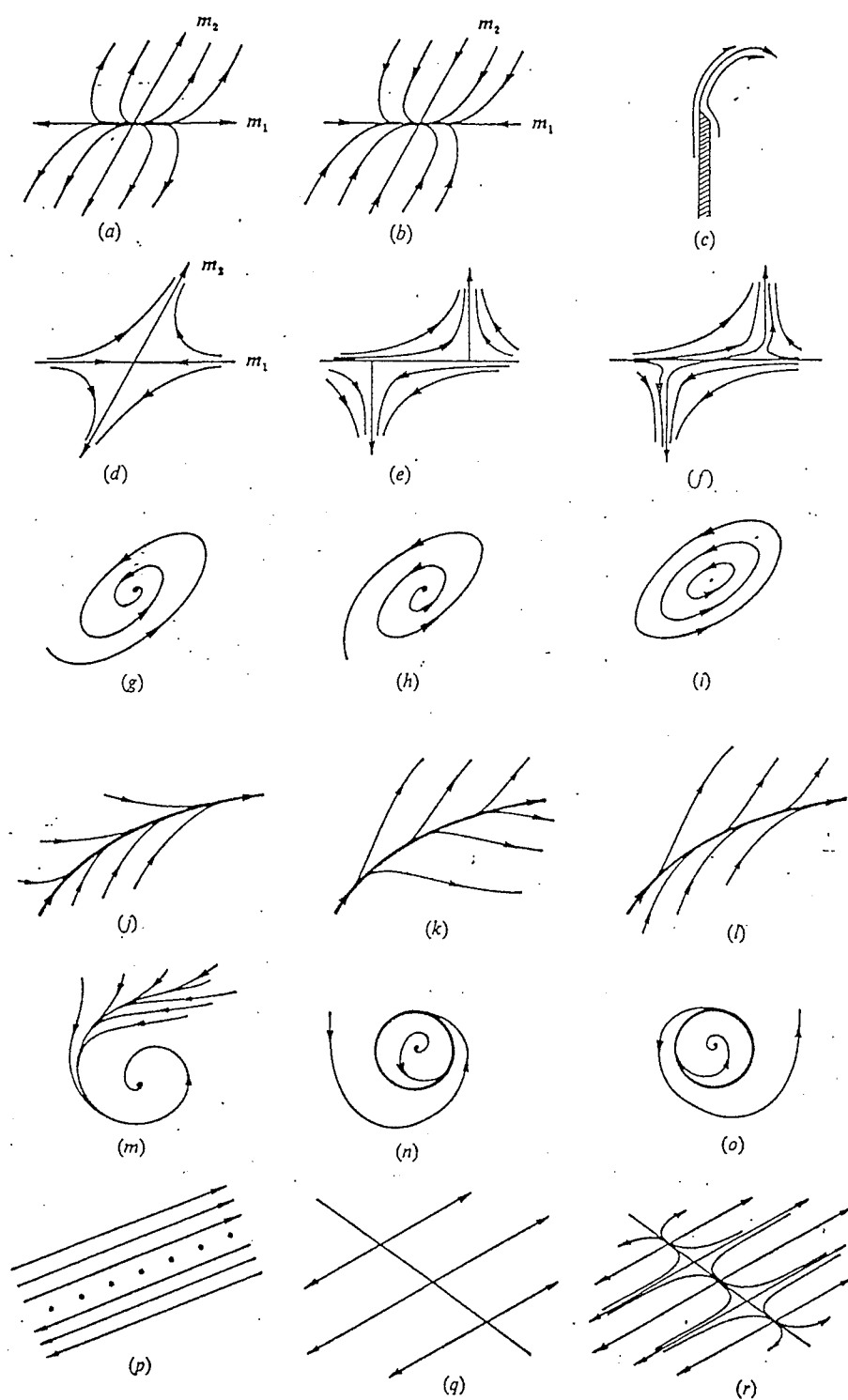
Figure 1.4: Examples of possible critical point topologies (Perry & Steiner, 1987, Part I)

25
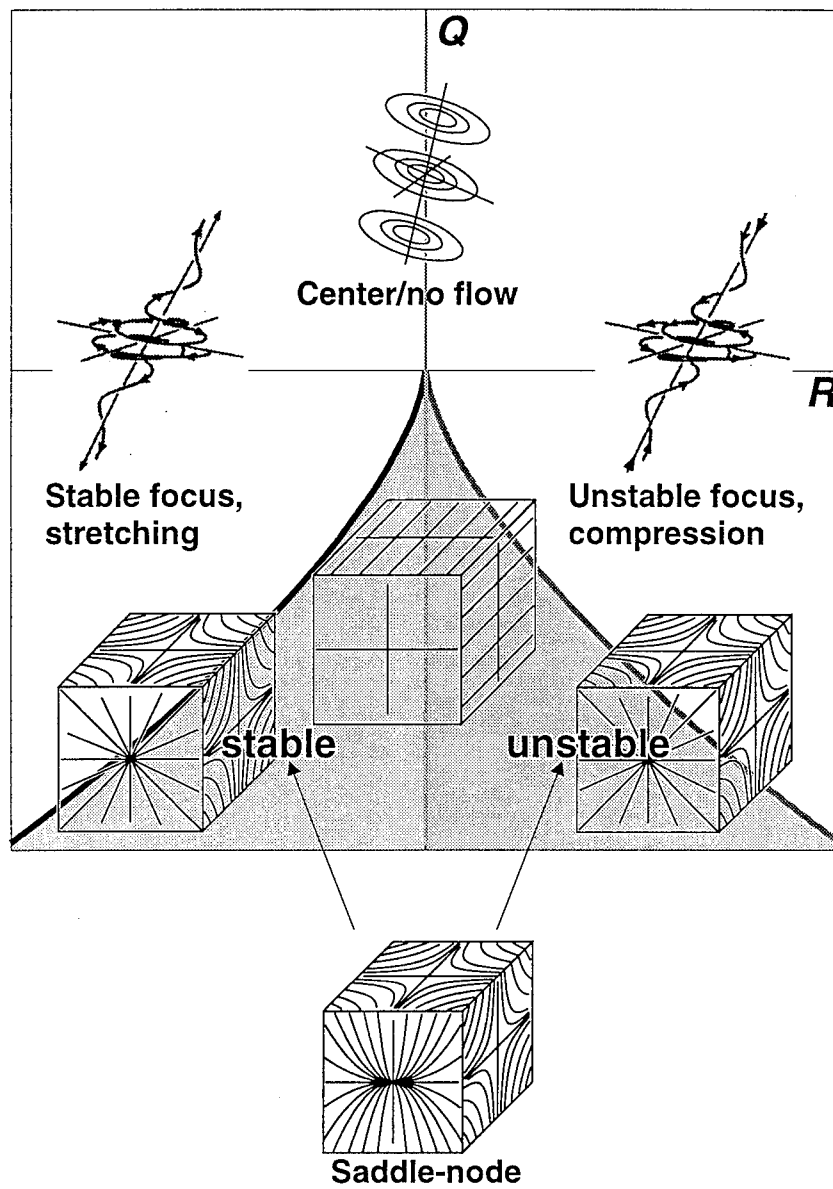
Figure 1-5: Possible critical point topologies for incompressible flow (Vorobieff, 1996)

U∞

Uc

λ

Γ

φ

δ

ω

+

Rounded vs. Sharp
Leading-Edge

α_eff

φ = Phase shift of arrival of incident vortex
relative to displacement of leading-edge
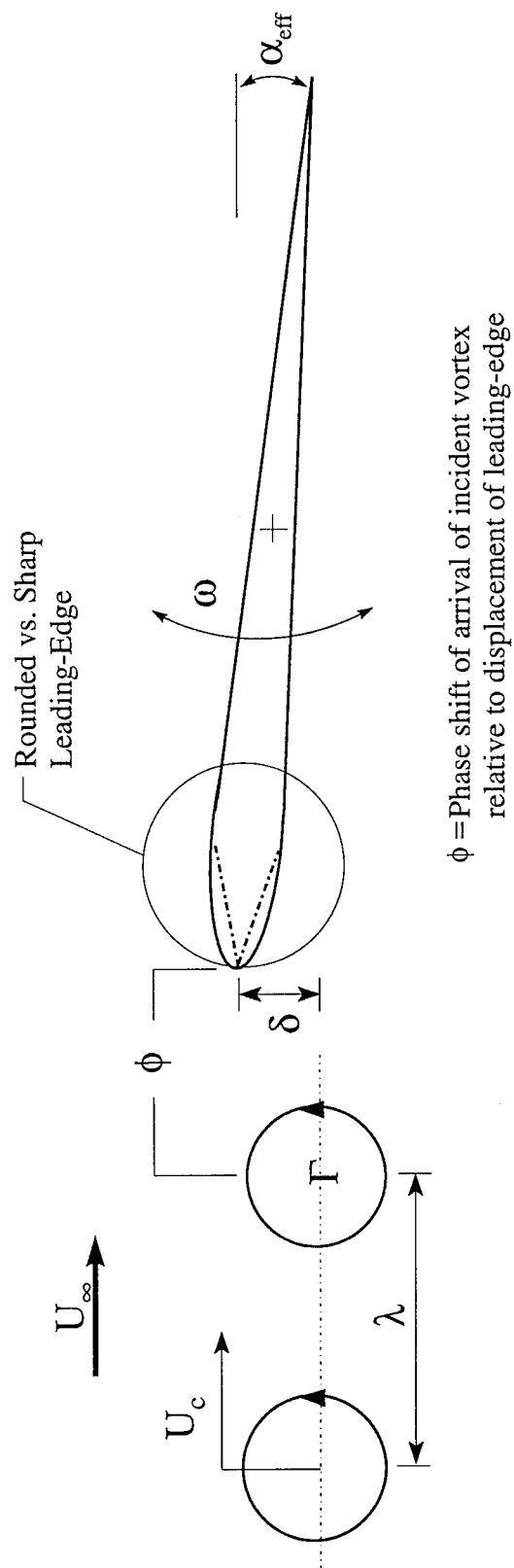
Figure 1.6: Significant parameters for vortex interactions with a stationary or oscillating leading-edge

2.0 EXPERIMENTAL SYSTEMS AND TECHNIQUES

2.1 Flow System

Experiments were conducted in a recirculating, free-surface water channel located in the Lehigh University Fluid Mechanics Laboratory. The water channel consists of a transparent Plexiglas test section, 597 mm × 933 mm, upstream and downstream reservoirs, and an Ingersoll-Rand pump, providing reliable test section flow speeds of 2.0 cm/sec to 38 cm/sec. Flow speeds vary linearly according to U (cm/sec) = 0.0245 × RPM and are calibrated for a test section water depth of 540 mm. A flow conditioning section involving honeycomb and screens is located immediately upstream of the contraction, which has an area ratio of 2:1. This flow conditioning provides very low levels of turbulence intensity in the test section. Experiments were conducted at two different flow speeds in the test section: 3.8 cm/sec and 15 cm/sec, corresponding to Reynolds numbers Re=6,250 and 25,000, based on the chord of the oscillating plate.

2.2 Experimental Apparatus

Figure 2.1 shows a schematic of the experimental system used. A 7.5 cm chord, NACA 0012 airfoil is located 17.8 cm upstream of a 15 cm chord, 6 mm thick flat plate which is tapered at the leading and trailing edges with a 30° included angle. Both the airfoil and the plate are mounted in separate sections, placed between two 1.2 cm thick false walls, spaced 30.5 cm apart to facilitate installation in the water channel test section. The front and aft section false walls are aligned and butted together to provide a smooth inner surface to minimize spanwise disturbances. The NACA 0012 airfoil is sinusoidally oscillated about its leading-edge to provide a quasi-two-dimensional vortex

28

street that convects downstream and impinges upon the leading-edge of the flat plate. The transverse displacement of the incident vortex street was varied by vertically translating the pivot supports of the upstream airfoil and was located such that the center of the clockwise rotating vortex was aligned with the tip of the leading-edge of the stationary flat plate at zero degrees angle-of-attack. The airfoil is oscillated with an amplitude of $\pm$ 7.5° and a reduced frequency $k = \dfrac{\omega c}{2U_\infty} = 5$, where c is the chord length of the downstream flat plate and U_∞ is the freestream velocity. In certain experiments, the flat plate was oscillated about its mid chord position with $k = 5$ and an amplitude of $\pm$ 5°. An orthogonal coordinate system fixed to the laboratory frame is used, where the x-axis is oriented in the free-stream direction at the location of the laser sheet, the y-direction is vertical, perpendicular to the free-stream, and the z-direction is along the wing span, perpendicular to the x-y plane.

In this investigation, only one reduced frequency was used. Consequently, specific instants during one oscillation cycle at the reduced frequency were denoted as a specific cycle angle (β). The actual period of oscillation in seconds, for a given oscillation cycle at the reduced frequency, will depend on the Reynolds number of the flow. For example, when Re=25,000, the period of oscillation is 0.624 seconds. At Re=6,250, the period is 2.52 seconds.

In the case when a vortex street is produced by the oscillating NACA 0012 airfoil, a cycle angle of β=0° is defined as the point in the oscillation cycle when the center of the incident clockwise vortex is approximately 10 mm from the stationary leading-edge. (Refer to section 3.2 for a description of how the center of the incident vortex was determined.) In the case where there is no incident vortex street and the leading-edge of the flat plate is oscillating sinusoidally, then a cycle angle of β=0° is defined as the instant in the oscillation cycle when the leading-edge is pitching upwards (+ y direction) and is at an angle-of-attack α=0°. In cases where the leading-edge oscillates with an incident

29

vortex street, a phase angle ϕ is defined as the difference between the cycle angle of the incident vortex and that of the oscillating leading-edge, or $\phi=0°$ when $\beta=0°$ for the incident vortex and $\beta=0°$ for the oscillating leading-edge. Therefore, as shown in figure 2.2, the phase angle $\phi=0°$ when the oscillating leading-edge is at $\alpha=0°$ while in its upstroke at the arrival of the incident vortex. Although in this investigation phase angles were varied in increments of 45° from 0° to 315°, inclusive, only results of $\phi=0°$ and $\phi=180°$ are presented.

Oscillation amplitude, frequency and phase of both the airfoil and flat plate are controlled by two stepping motors (Parker AX57-102 Compumotor), one for each wing, via a Parker PC-23 indexer and a microstep driver. Motor to wing gear ratios are 1:4 for the airfoil and 1:8 for the flat plate. Compumotor motion profiles are first generated by the in-house program SFG (Magness 1990) and consist of motor displacements for a given time interval. These motion profiles are executed by the in-house program ALT (Magness and Troiano 1991) which allows control of up to three Compumotors simultaneously. Motion commands are sent from ALT to the indexer which converts the displacement commands from the computer into signals, which are then sent to the microstepping driver. This driver converts the indexer signals into proper current levels for precise motion of the motors (25,000 steps/rev).

In addition to displacement commands, the motion wave form profile may also contain embedded auxiliary commands to synchronize other experimental apparatus with the motion of the wings. This approach was used to trigger a 35 mm camera to obtain PIV images of the mid-span position of the flat plate, in the region of the leading-edge at selected oscillation cycle angles. When Re=6,250, a time sequence of PIV images was obtained for two complete oscillation cycles in cycle angle increments of 20°, corresponding to time increments of 0.140 seconds. For the case of $\phi=180°$, images were acquired in a time sequence beginning with $\beta=20°$ and ending with $\beta=0°$. In all the

other cases the time sequence of data began at $\beta=200°$, ending at $\beta=180°$. Consequently, $\beta=340°$ is not the end of the sequential data, only the end of a <u>defined</u> oscillation cycle. When Re=25,000 the framing rate of the camera would allow only four images per oscillation cycle to be obtained in cycle angle increments of 90°, corresponding to 0.156 second time steps.

2.3 Laser Scanning and Image Acquisition Techniques

A scanning laser version of high-image-density particle image velocimetry (PIV) was used to obtain an instantaneous, quantitative representation of the velocity flow field. PIV has several advantages over standard laser anemometry in that velocities are measured with high spatial resolution and accuracy over an entire plane at an instant of time. From this "snapshot" of the velocity field, instantaneous vorticity distributions, along with other flow properties can be easily calculated. Comprehensive reviews of PIV techniques are given by Adrian (1986,1991), Lourenco et al. (1989), Rockwell et.al. (1992, 1993), Rockwell and Lin (1993) and Reuss et al. (1989). A full description of the experimental approaches is also given by Rockwell et al. (1992, 1993), Rockwell and Lin (1993), Towfighi and Rockwell (1994), and Chow (1992). A brief description of PIV techniques follows.

A continuous wavelength Argon-ion laser beam (Coherent Innova series laser) with the capability of variable power output from 1 to 30 watts initially passes through a focusing lens combination (Corcoran 1992) to a rotating, 72 facet mirror (Lincoln Laser Co), producing a vertical scanning laser sheet, 1-2 mm thick, which illuminates seeding particles in the flow (refer to figure 2.1). In this study a laser power output of 20 or 30 watts was employed, depending on flow conditions. The seeding particles are silver-coated, hollow glass spheres with an average diameter of 14 microns and density of 1.65

31

gm/cc (Conduct-O-Fil made by Potters Industries, Inc.). Although these particles are not quite neutrally buoyant, flow speeds are such that the mixing occurring in the channel return pipe is sufficient to keep the particles uniformly suspended in the test section.

As the particles move in the flow, the laser beam will illuminate particles at a scanning frequency $f_{sc} = 72\ f_m$, the product of the rotation frequency f_m of the rotating mirror and the number of mirror facets (72). For more accurate control of f_m at lower rotation rates, variable-frequency motor control for the rotating mirror (Lincoln Laser Co. VFC-2) employs a sweep function generator (Heath Co. SG-1274) to send a square wave, with an amplitude of +5 volts, as the frequency input. Typical values of f_m ranged from 14.0-36.6 Hz, yielding scanning frequencies of 1008-2635 Hz.

When the scanning laser sheet is oriented parallel to the free-stream, a quasi-two-dimensional view of the impinging vortex and leading-edge flow field is obtained (see figure 2.3). The flow field illuminated by the laser sheet is captured on 35 mm Kodak TMAX 400 film by a Canon EOS-1 N RS camera with a 2X teleconverter and Macro 100 mm telephoto lens combination. A camera shutter speed of 1/250 and f-stop=5 is used for the low Reynolds number case while shutter speeds of 1/500, f-stop=4.5 and 1/640, f-stop=4 were used in the higher Reynolds number flow. The Canon camera can achieve synchronized framing rates of nearly 9 frames/sec when TTL signals from a microcomputer are sent to the camera's remote control socket to trigger the shutter. This higher framing rate permitted the acquisition of a sufficiently resolved time sequence of PIV images for the lower Reynolds number case.

Images acquired in this manner require the addition of an artificial bias velocity to resolve the directional ambiguity caused by reverse flow (Adrian 1986). This is done by rotating a mirror placed between the flow field and the camera. The counterclockwise rotation of the bias mirror is initiated just before an image is to be photographed such that the mirror will be oriented at 45° to the laser sheet when the camera shutter is open.

Bias velocities are obtained by using a Scanner Control (General Scanning Inc. CX-660) to specify the amplitude and frequency of the ramp function generating the rotation of the mirror. In this investigation, bias frequencies of 11.63-39.0 Hz and amplitudes of 0.5-0.7 V were employed to obtain bias velocities ranging from 4-5.6 times the freestream velocity and directed in the negative y direction, 90° to the freestream velocity. These bias velocities also decreased the dynamic range of velocities in a PIV image which improved interrogation results by reducing the number of "bad" vectors (see subsection 2.4).

Oschwald et al (1995) report possible sources of significant error from the use of a rotating bias mirror in acquiring PIV images, depending on the relative locations of the camera, bias mirror and laser imaging plane. When the bias mirror is located very close to the image plane and the mirror is rotated with a large amplitude, errors from aberrations of the particle displacements around the mirror perimeter will occur. As the distance of the bias mirror from the image plane increases, these errors will decrease. Furthermore, the total angle of rotation of the bias mirror in this investigation was from approximately 44.5°-45.5°, an amplitude of 1°, which occurred over a period ranging from 26-86 milliseconds. The camera's shutter was open for a maximum of 8% of the total bias mirror rotation period when the mirror angle was very close to 45°. Consequently, based on results by Oschwald et al, the distortion-induced error from the bias mirror in this study is negligible.

For a given local flow velocity, a proper combination of laser scanning frequency f_{sc}, bias mirror velocity and shutter speed will produce, on the film negative, multiple images of individual particles in the direction of the vector sum of the local and bias velocities, with the spacing between the particle images proportional to the magnitude of the vector sum. The following section describes the technique of extracting velocity data from the developed negatives.

2.4 Image Processing and Evaluation

When the photographic images have been developed using standard black and white film processing procedures, they are first digitized using a Nikon LS-3510AF 35 mm film scanner at a resolution of 125 pixels/mm and are stored as TIFF files on the computer hard drive. The TIFF files are then interrogated using an in-house developed computer program known as PIV3 (Seke 1993). A window size of 128 pixels × 128 pixels (1.02 mm×1.02 mm) is specified in which a single-frame, cross-correlation within each window is performed by applying two successive two-dimensional Fourier transforms to the pattern of particle images within the window (Keane and Adrian 1992). An average displacement vector results and is placed in the center of the window. The interrogation continues for the entire image by overlapping the windows 50% and produces a vector field with a grid size of 0.51 mm × 0.51 mm. The program TRACE-S (Vorobieff, 1994) is employed to trace and define the boundaries of objects within the image field. Further discussion of this program and its capabilities is written in Appendix A.

The resulting vector field and corresponding boundaries are viewed using the program V3 (Robinson 1992), developed in-house, to determine incorrect or "bad" vectors from the interrogation. These types of vectors can result when an incorrect particle correlation is made near boundaries or within shadow regions, or when the particle images are too widely spaced for the interrogation window size specified. Generally, fewer than 2% of the vectors are incorrect. Using V3, the incorrect vectors are removed from the vector field. V3 is also capable of calculating streamlines from the vector field.

Following the removal of incorrect vectors, the in-house program NFILVB (Lin 1994) interpolates between the vectors surrounding the "holes" using a bilinear least-

34

squares fit technique. In addition, NFILVB utilizes the image magnification factor M, the bias velocity V_{bias}, and the scanning frequency f_{sc} to convert interrogated displacements to velocity magnitudes on the scale of the actual flow field. The magnification factor $M = \dfrac{l_i}{l_p}$, where l_i is the length scale of the image on the negative, and l_p is the real physical length scale. Magnification factors of 0.68 for the lower Reynolds number case and 0.65 for the higher Reynolds number case were obtained in this study, yielding a vector grid size in the physical plane of 0.75 mm $\times$ 0.75 mm and 0.79 mm $\times$ 0.79 mm, respectively. The bias velocity is determined by calculating the displacement of a stationary object on the image due to the motion of the bias mirror. The interpolated and scaled velocity field is also smoothed by a Gaussian weighted averaging technique based on Landreth and Adrian (1989), in which a smoothing parameter of 1.3 was used. Finally, vorticity is calculated from the velocity data. The uncertainty in the velocity and vorticity field is less than 1% and 5%, respectively.

Based on interpolated velocity data, circulation and streamlines are calculated and displayed by program V3. The technique for calculating values of vorticity and non-dimensional circulation is discussed in Appendix B. The ensemble average of velocity fields is calculated by program ENSAV (Robinson 1991). Correlation of vorticity field is obtained by the program VCOR2 (Seke 1993). Iso-vorticity contours are generated and displayed by the program SURFER (Golden Software Inc. 1989) in which spline curve fitting was utilized to construct the contour map. In order to reduce background noise on selected images so that major features of the flow can be shown, the program FILTER is used to spatially filter velocity or vorticity fields. To extract velocity information along a specified curve within the PIV images, the program BLINTP (Lin, 1995) is used. This allows determination of velocity profiles at selected spatial locations in the image. Additional programs were written specifically for this investigation

35

including CIRFLUX, which determines the local circulation and vorticity flux of specified control volumes within PIV images; TFLUX, determining the vorticity flux along multiple line segments in an image; and TIPVEL/TIPFLUX, determining the velocity and vorticity flux at the leading-edge, orthogonal to an extension of the line of symmetry of the flat plate.
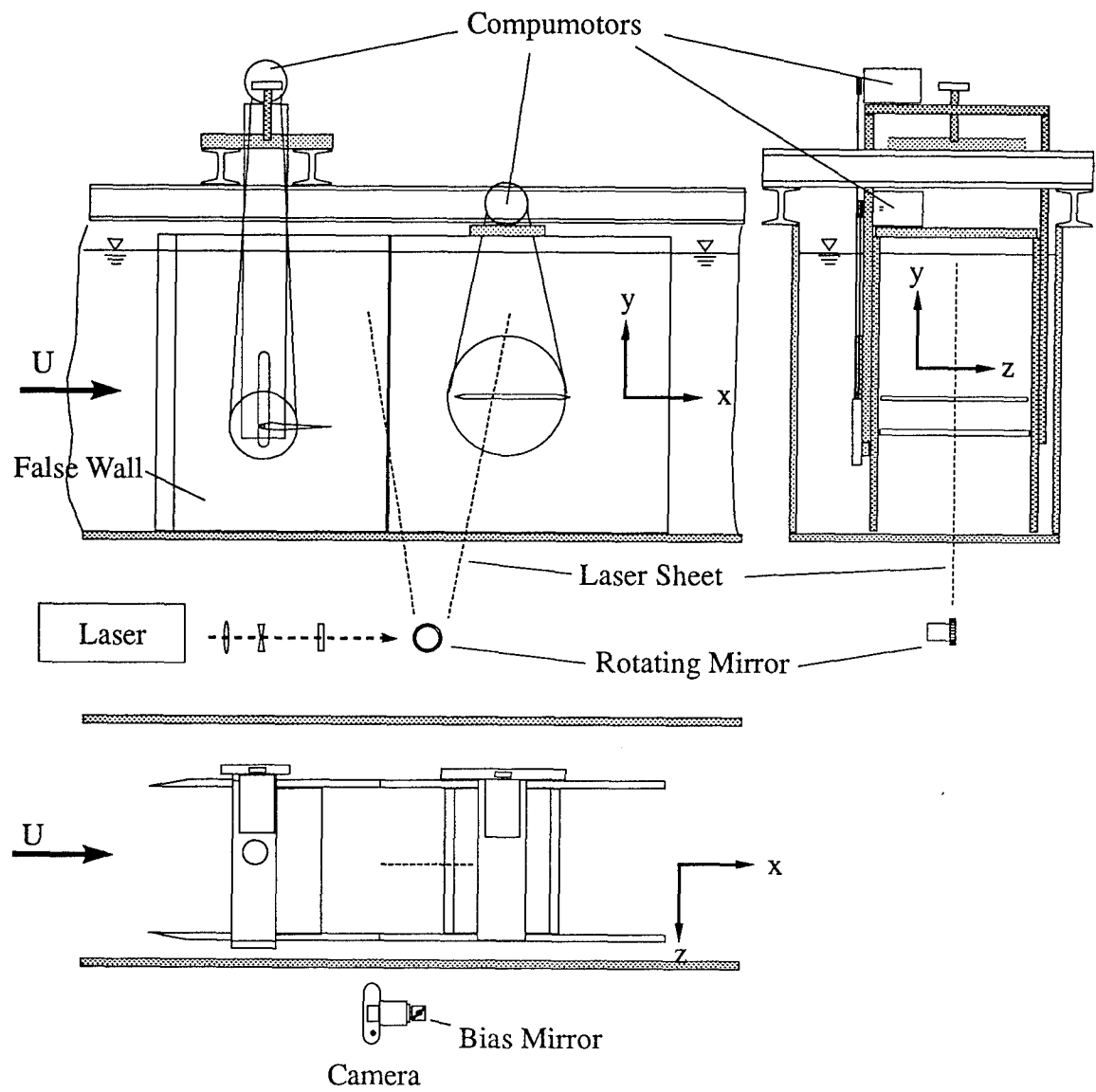
Figure 2.1: Experimental System
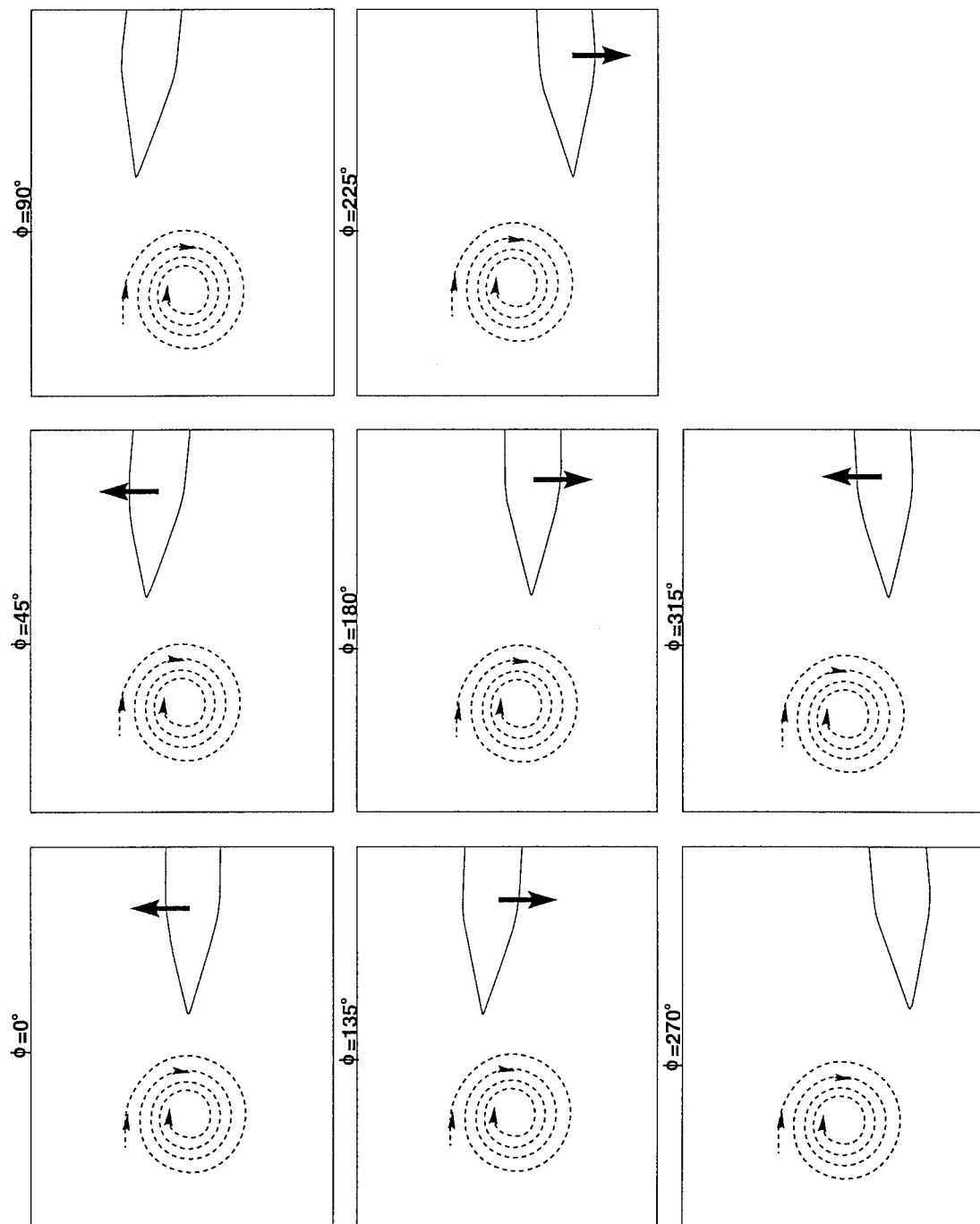
Figure 2.2: Schematic of Representative Phase Angles for an Oscillating Leading-Edge
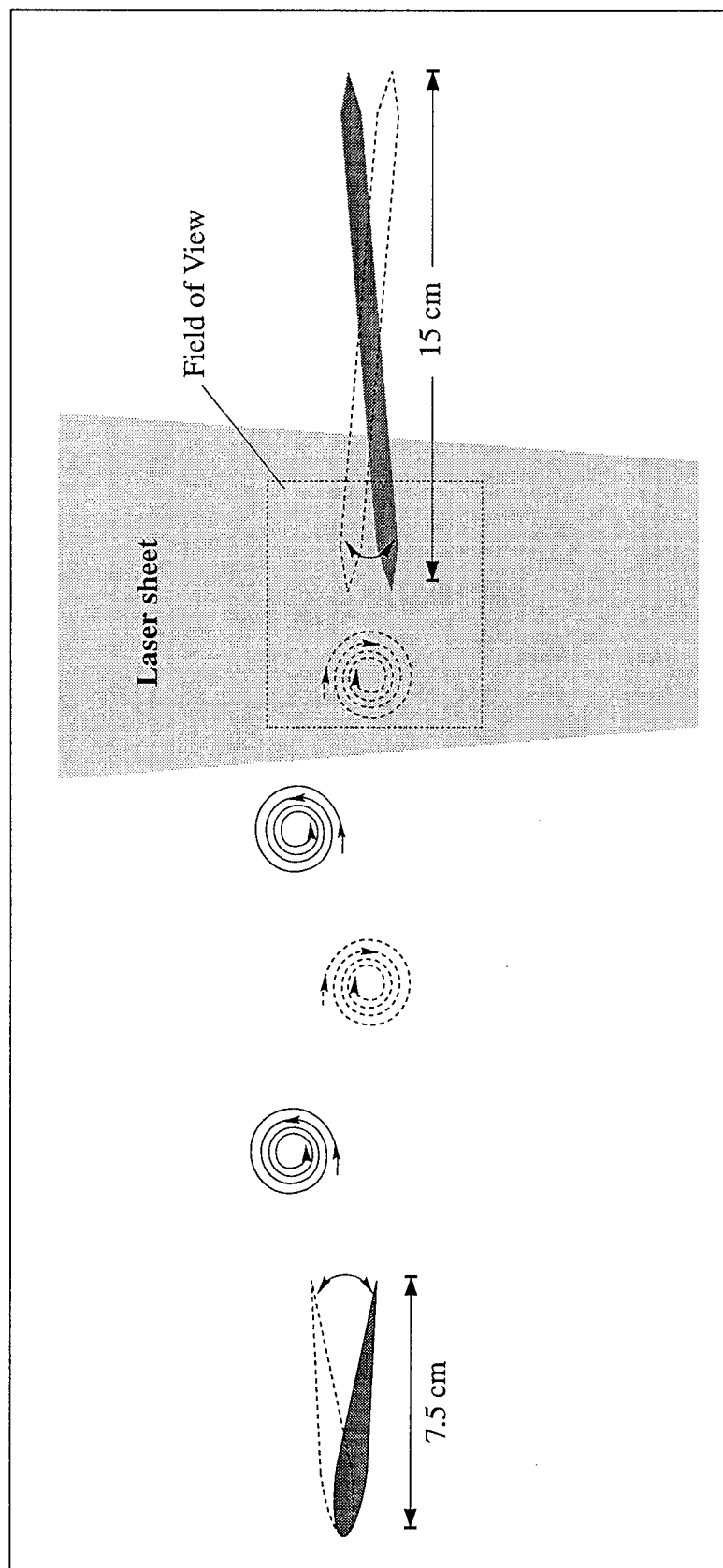
Figure 2.3: Quasi-Two-Dimensional View

3.0 NATURE OF THE INCIDENT VORTEX

Booth (1990) and Wilder (1992) employed an oscillating airfoil to generate a vortex street that subsequently impinges upon the leading-edge of another body. Wilder (1992) found that the reduced frequency of the oscillation affected the spacing or wavelength of the vortex street while the amplitude of oscillation influenced vortex size and circulation. In this study, a NACA 0012 airfoil was oscillated about the leading-edge with a reduced frequency k=5 (based on the chord of the flat plate) and an amplitude A = 7.5°. At a freestream velocity U=38 mm/s, the airfoil oscillation produced a vortex street of wavelength 93 mm with counter-clockwise rotating vortices in the upper row and clockwise vortices in the lower row of the street.

In this investigation, a two-dimensional incident vortex street was desired. However, it is very difficult indeed to experimentally produce a purely two-dimensional vortex along the entire span of the test section due to effects induced by the section walls. Nevertheless, a vortex can be considered quasi-two-dimensional if the end effects are minimal and the central portion of the vortex remains two-dimensional. This chapter characterizes the nature of the incident vortex using the results of qualitative flow visualization and PIV.

3.1 Qualitative Investigation

The same laser scanning technique used for PIV was slightly modified to produce two orthogonal laser sheets oriented in the vertical x-y and horizontal x-z planes. These laser sheets were intended only to provide qualitative results, not for obtaining PIV data. These qualitative investigations showed the wall induces a thickening of the vortex core which propagates toward the center-span as the vortex convects downstream. At the

40

point of impingement upon the leading-edge of the flat plate, the central third of the vortex still retains its initial core diameter, indicating approximate two-dimensionality.

This wall effect was also noted by Laursen, Rasmussen and Stenum (1996). Analogous to this wall effect, Schlichting (1968) describes flow for a quiescent fluid over a rotating disk. When the disk rotates, the viscous effects near the surface of the disk cause the centrifugal force to move the fluid radially outward from the center. This causes a velocity along the z-axis (orthogonal to the plane of the disk, passing through its center) toward the disk. Applying Schlichting's result to the case when the wall is stationary and the fluid is rotating in a line vortex whose axis is perpendicular to the wall, the pressure gradient is lower along the axis of the vortex. Consequently, fluid will move along the axis of the vortex away from the wall. Due to viscous effects on the wall, the rotation of the vortex at the wall will be slowed, causing an increase in the vortex diameter. These results indicate a finite axial velocity must exist along the core of an initially two-dimensional vortex.

3.2 Quantitative Assessment

PIV images captured the instantaneous velocity field of the incident vortex convecting toward the leading-edge for the various cases considered. From the plots of contours of constant vorticity, the approximate center of the incident vortex was located and velocity profiles were obtained along horizontal and vertical line segments passing through the center of the vortex. Figure 3.1 shows a representative plot of these velocity profiles. If the incident vortex is considered to be axisymmetric, with a maximum tangential velocity V_θ, then the vortex center, convection speed U_c, V_θ, and diameter D can be obtained from these V_θ profiles. In reference to figure 3.1, the x-coordinate of the vortex center may be determined by noting the x-position where the vertical velocity

41

component is equal to 0. Similarly, the y-coordinate of the center is the location where the u velocity component is equal to U_c. The convection speed $U_c = \dfrac{U_{max} + U_{min}}{2}$ and the tangential velocity $V_\theta = \dfrac{U_{max} - U_{min}}{2}$, where U_{max} and U_{min} are the maximum and minimum values of the u component of velocity along the vertical line segment and can be seen in figure 3.1. The vortex diameter D_v is simply the y-distance between the maximum and minimum u component velocities.

These incident vortex parameters were calculated at various points in the cycle for the stationary and oscillating leading-edge cases. Averages of V_θ=25 mm/s and vortex diameter D_v=15 mm were obtained. Figure 3.2 shows values of U_c for the various cases where the incident vortex is visible and intact as a vortex. From figure 3.2 it can be seen that U_c is dependent on the proximity of the vortex to the leading-edge and on the motion of the edge. The average values of V_θ and D_v were employed to determine a model for estimating the induced velocity V_i at the tip of the leading-edge. The model assumes a tangential velocity according to solid body rotation within the central region:

$$\text{for a radius } r < 7.5 \text{ mm}, \quad V_i = 25\frac{mm}{s}\left(\frac{r}{7.5 \text{ mm}}\right) \qquad (1a);$$

and a velocity distribution corresponding to an irrotational vortex in the outer region:

$$\text{for } r \geq 7.5 \text{ mm}, \quad V_i = 25\frac{mm}{s}\left(\frac{7.5 \text{ mm}}{r}\right) \qquad (1b).$$

Based on this model, the velocities induced on a stationary leading-edge were calculated from the horizontal distance between the tip of the leading-edge and the center of the incident vortex. At the point in the vortex shedding cycle where the clockwise vortex is about to collide with the leading-edge (β=0°), V_i = -17.5 mm/s.

It was desired to induce a velocity of the same magnitude at the edge from the oscillation of the leading-edge only. From the flat plate geometry,

$$V_{iosc} = -\frac{c}{2}\omega A \cos(\omega t) \qquad (2),$$

42

being maximum when $\cos(\omega t) = 1.0$. This occurs when the instantaneous angle-of-attack of the flat plate is $\alpha = 0°$. Since the reduced frequency of the flat plate must match that of the upstream oscillating airfoil, equation (2) could be solved for A. The result is $A = 5.2°$, which was approximated as $A = 5°$. The resulting induced velocities defined by equations (1) and (2) are plotted in figure 3.3 over the course of an oscillation cycle.

Once the convection speed of the incident vortex is determined, a reference frame which moves with the speed of the vortex can be used to examine the topology. As reviewed in Chapter 1, only certain types of topologies may exist in two-dimensional flow. Therefore, these patterns may substantiate the qualitative results. Figure 3.4 shows a sequence of the streamline topologies for a vortex about to impinge upon a stationary leading-edge in a frame of reference moving at $U = 34.3$ mm/s ($U/U_\infty = 0.9$). At $\beta = 340°$, the topology of the incident vortex shows that the outer streamlines are slightly distorted from their initial shape. At the core of the vortex are a series of concentric circles which are nested within a stable limit cycle. This topology can only occur in two-dimensional flow. Hence, the central region of the incident vortex retains its two-dimensional nature as it impinges upon the leading-edge. At $\beta = 0°$, the incident vortex shows more pronounced distortion with an unstable focus at its center, indicating compression along the spanwise axis (z-axis, into the page) of the vortex. It is not definitively clear from this result alone whether the upstream influence of the leading-edge caused this axial compression or whether it came from the wall effect, but considering the qualitative results, it most likely came from the leading-edge.

3.3 Conclusions

The nature of the incident vortex has been examined qualitatively and quantitatively and appears to remain essentially two-dimensional at mid-span, within the core of the

43

vortex, until it impinges upon the leading-edge. The convection speed of the incident vortex depends on whether the leading-edge is stationary or oscillating and varies as it approaches the edge. Average values of the incident vortex diameter and tangential velocity along the circumference were determined from velocity profiles extracted from PIV data. This information provided the means to estimate the velocity induced by the approaching vortex at the tip of the stationary leading-edge. This induced velocity at $\beta = 0°$ closely matches the maximum induced velocity of a leading-edge oscillating with an amplitude of 5 degrees, without an incident vortex.
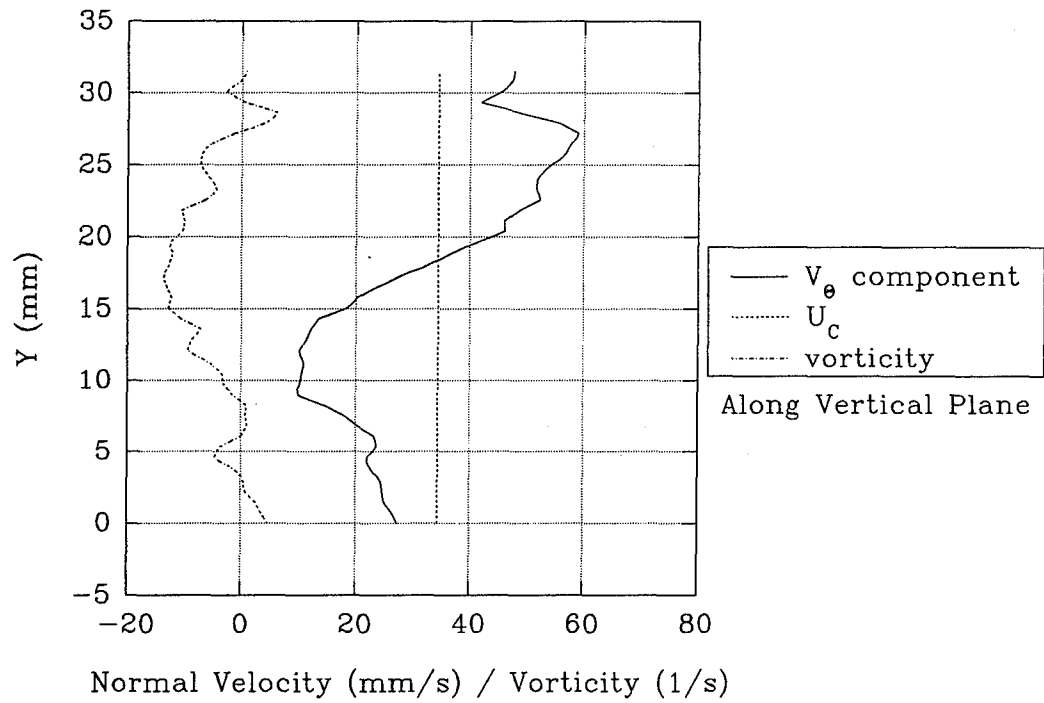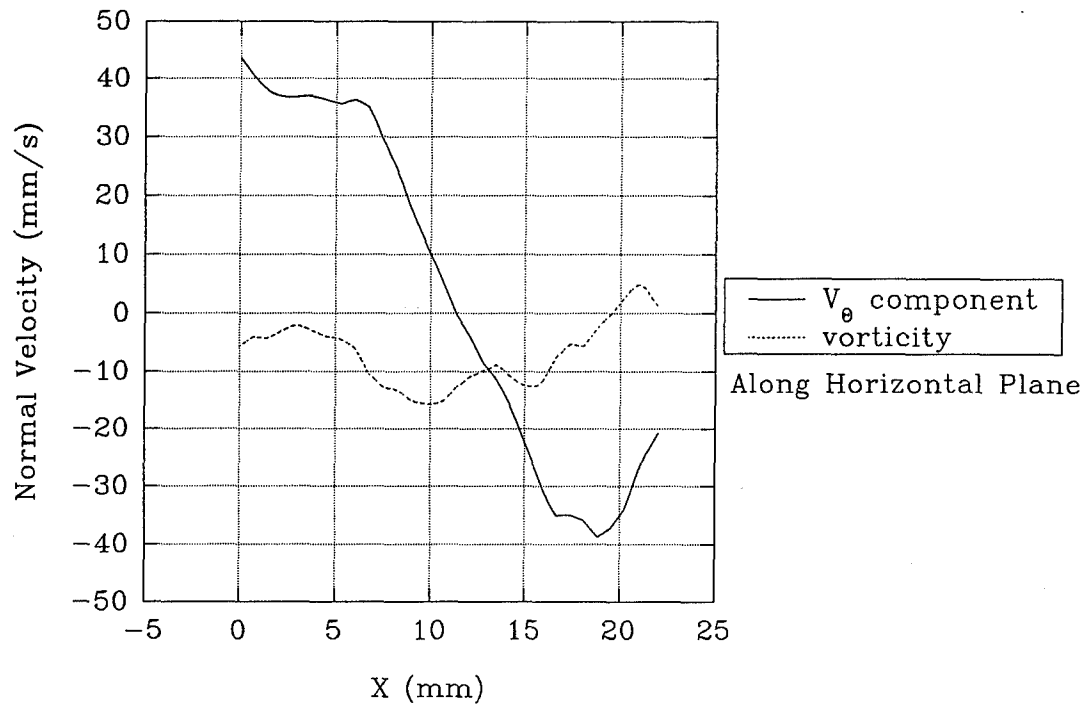
Figure 3.1: Instantaneous velocity and vorticity profiles for a stationary leading-edge at $\dot{\beta}=0°$
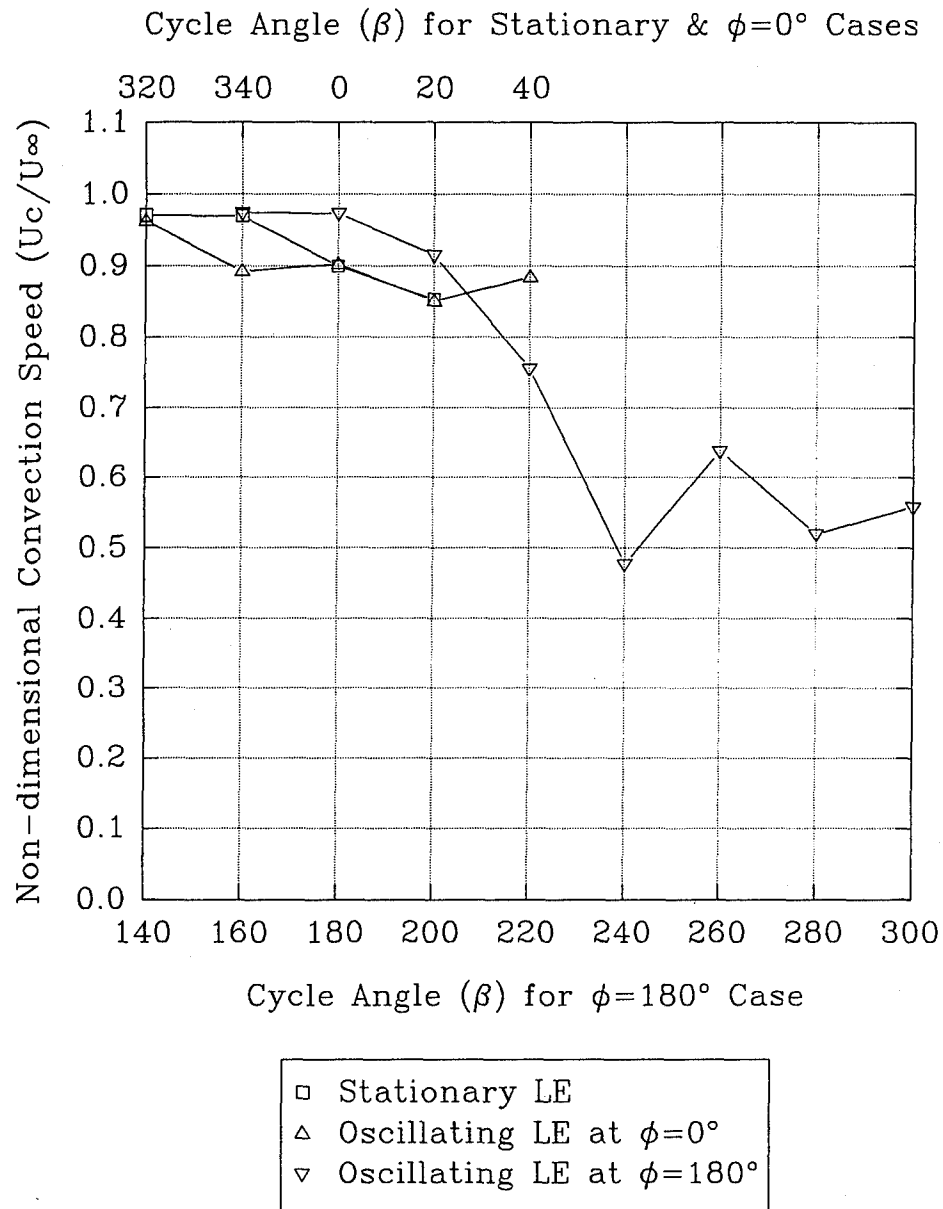
Figure 3.2: Non-dimensional convection speed of an incident vortex

46
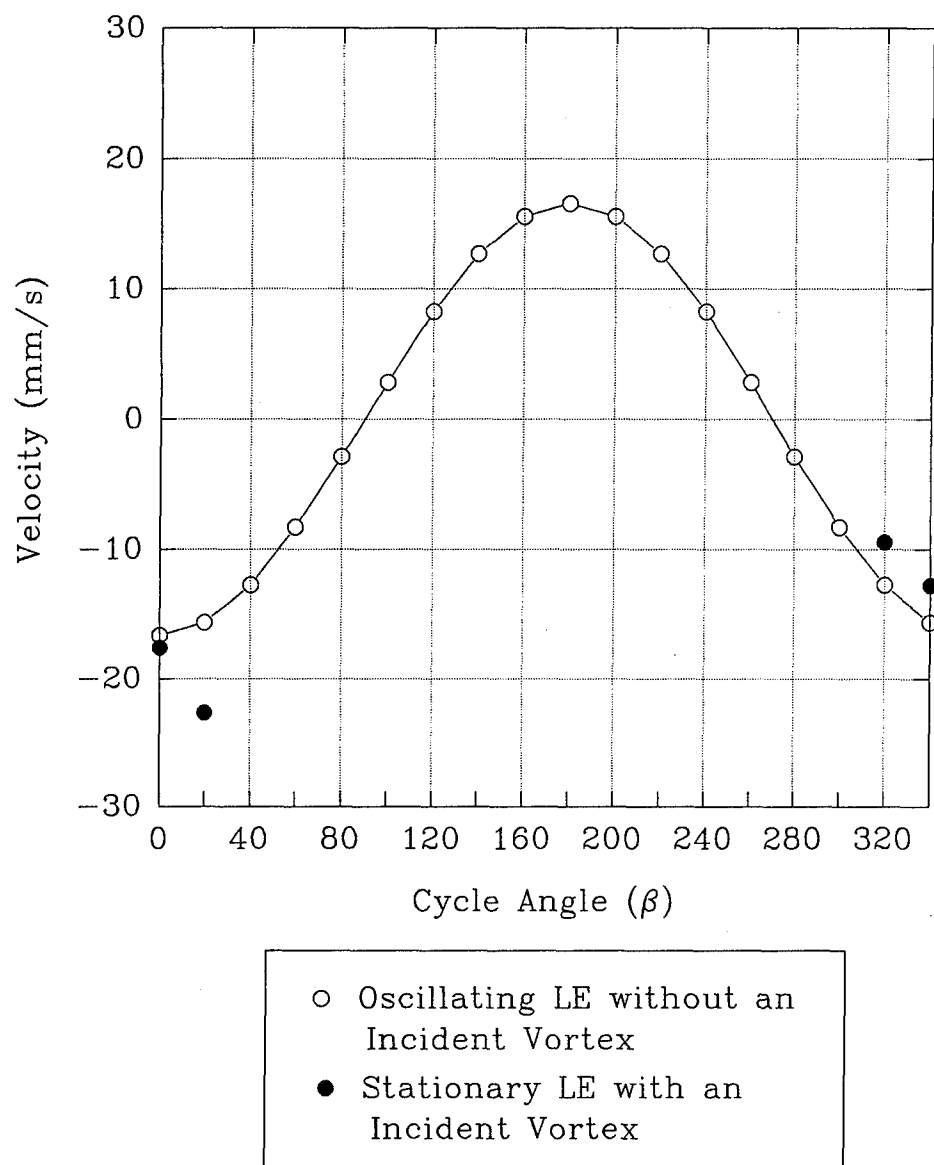
Figure 3.3: Velocity induced at the leading-edge
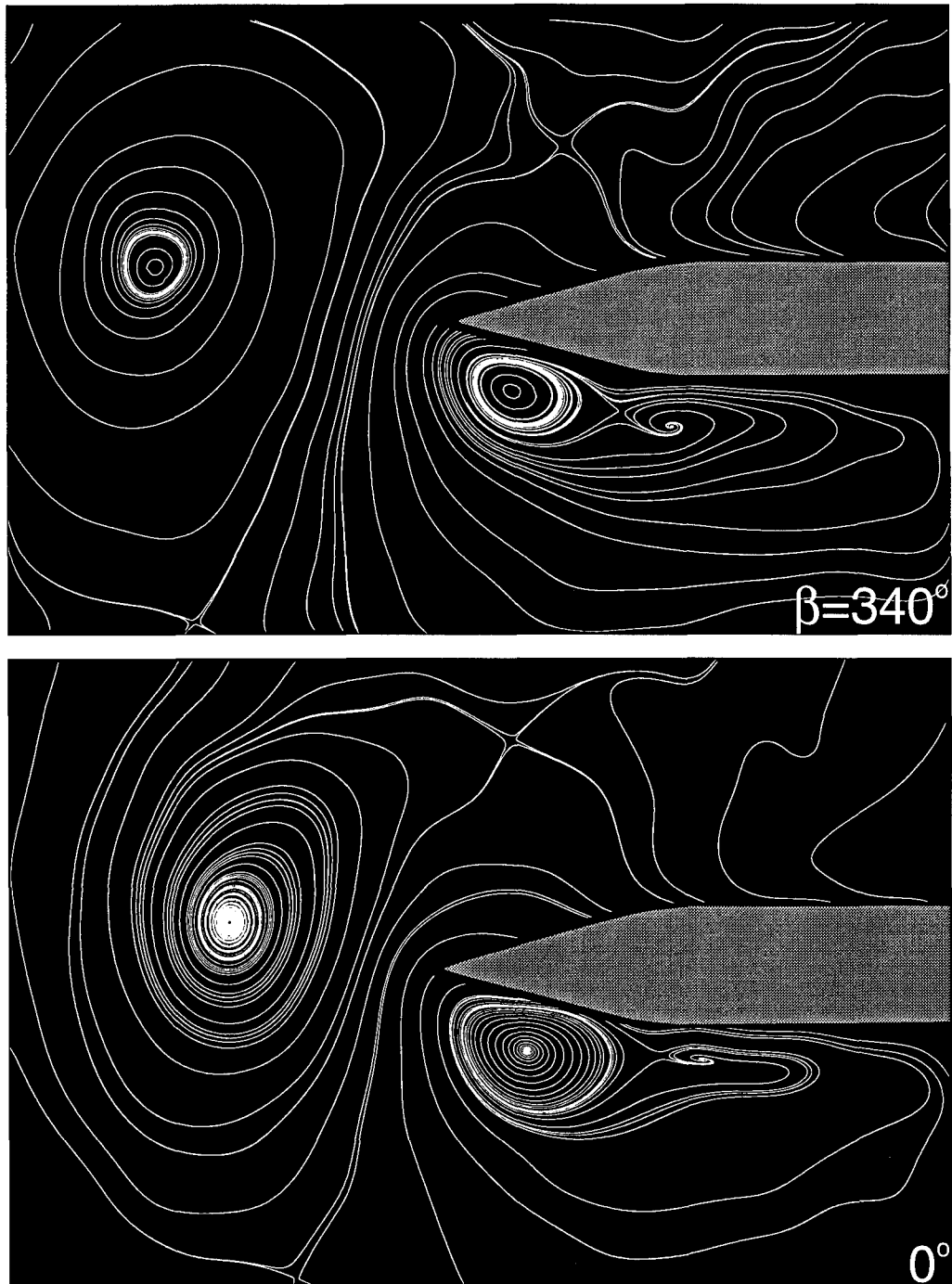
Figure 3.4: Streamline Patterns in a Reference Frame Moving at $U/U_\infty = 0.9$ for a Stationary Leading-Edge with an Incident Clockwise Vortex.

4.0 VORTEX INTERACTION WITH A STATIONARY LEADING-EDGE

4.1 Flow Structure for an Incident Vortex Directly Impinging the Leading-Edge

In order to provide a reference case for the interaction of a vortex with an oscillating leading-edge, attention is first focused on a vortex that impinges directly upon a stationary leading-edge. Contours of constant vorticity and streamline patterns of the instantaneous velocity field obtained via PIV are used to show the development of the interaction with time.

4.1.1 *Vorticity Field Development*

Figure 4.1 shows the flow development using contours of constant vorticity, where $|\omega_{min}|=5$ sec^{-1} and $\Delta\omega=5$ sec^{-1}. In this and all the following vorticity contour plots, dashed lines denote contours of negative vorticity while solid lines indicate contours of positive vorticity. A thin, black region surrounding the leading-edge indicates a region very close to the surface of the body in which accurate PIV data cannot be obtained. (See appendix A for a more detailed explanation of the treatment of PIV data near boundaries.)

In figure 4.1 at $\beta=340°$ to $20°$, the clockwise-rotating incident vortex of negative vorticity is clearly evident on the left side of the image as it approaches the stationary leading-edge. At $\beta=20°$, the incident vortex begins to deform noticeably, being compressed in the x-direction and elongated in the y-direction as it collides with the tip. This incident vortex deformation continues until it is split into two sections ($\beta=60°$). For $\beta=80°$ to $120°$, the upper section appears to roll along the upper surface of the leading-edge, adding to the negative vorticity of the boundary layer, while remaining a coherent structure. In contrast to the upper section, in $\beta=60°$ to $100°$, the lower section is

distended around a seemingly strong tip vortex of positive vorticity. The remaining fragments of the lower incident vortex section appear to rapidly convect downstream along the outer edge of the tip vortex at a rate faster than the upper section.

As the incident vortex approaches the leading-edge, there is significant flow development on the lower surface of the leading-edge. Beginning at $\beta=340°$, levels of positive vorticity near the tip are seen on the upper surface of the wedge, suggesting that the stagnation line is downstream of the tip. Along the lower surface, concentrations of positive vorticity develop, forming two distinct peaks on the forward part of the wedge. At $\beta=0°$, flow separates from the tip, forming a tip vortex of positive vorticity which begins to enlarge and extend along the surface, generating negative vorticity from the surface of the edge. At $\beta=20°$ to $60°$, this negative vorticity rolls up into a surface vortex and appears to pinch the tip vortex. From $\beta=0°$ to $40°$, the tip vortex continues to grow. At $\beta=60°$, the tip vortex begins to convect downstream. At $\beta=80°$, the surface vortex centered over the shoulder apparently separates the tip vortex into two components: a larger section further downstream (denoted as "A") and a smaller upstream section ("B"). From $\beta=80°$ to $120°$ the A vortex is detached from the surface and is of sufficient strength to eject the surface vortex and distort the remnants of the incident vortex. Both the A and B vortices convect downstream at the same rate, but B remains along the surface, while A moves away from it.

At $\beta=100°$, higher concentrations of negative vorticity begin forming near the tip on the upper surface of the wedge and at $\beta=120°$, the negative vorticity moves towards the lower surface. At the far left of the image, the positive vorticity contours of the incident counterclockwise vortex can just be seen approaching the leading edge.

4.1.2   Evolution of Circulation during the Interaction

The circulation of the vortical structures discussed above and described in figure

4.1, namely the incident vortex, the tip vortices (A and B) and the surface vortex, was computed, non-dimensionalized by $\pi U_\infty D_v$ and plotted in figure 4.2. It can be seen in figure 4.2 that the non-dimensional circulation of tip vortex A (note that the tip vortex prior to splitting is considered as tip vortex A) increases as the incident vortex approaches the leading-edge, reaching a magnitude slightly larger and of opposite sign, relative to the incident vortex at $\beta=40°$. The circulation of A decreases slightly as it begins to convect downstream at $\beta=60°$. When the tip vortex splits, the circulation of A is decreased by approximately the circulation of B such that the sum of A and B approximately equals A at $\beta=60°$. The values of circulation of A and B maintain relatively constant values as the two vortices convect downstream.

The surface vortex has a relatively small value compared to the incident vortex or the tip vortex A. However, the circulation of the surface vortex increases as the circulation of the tip vortex A increases, supporting the foregoing observation that the surface vortex is induced by the tip vortex. Nevertheless, once the surface vortex is formed at a given level of circulation of vortex A, it does not increase at the same rate as the tip vortex but at approximately one-third that rate. This suggests that only a portion of the circulation increase of vortex A is translated into an increase in the circulation of the surface vortex. At $\beta=80°$, the apparent increase in circulation of the surface vortex may be due to the merging of the surface vortex with a remnant of the incident vortex. Otherwise, it is due to splitting of the tip vortex.

The instantaneous vorticity field was divided into 24 regions along the x-axis (see figure 4.3), with an upper and lower section of each region in the vicinity of the leading-edge. A local circulation was calculated for each region and plotted in figure 4.4, showing the time sequence of the local circulation upstream of the leading-edge and on the lower surface of the leading-edge. For $\beta=340°$ to $40°$ the negative peak on the left side of the graph corresponds to the incident vortex. The positive peaks depict the

51

developing tip vortex on the lower surface. At $\beta=40°$, the peak of the incident vortex is smaller, indicating that only the lower half of the incident vortex is considered. From β $=60°$ to $80°$, the magnitude of negative circulation offsets some of the positive circulation produced by the tip vortex so that the total circulation for cells 13-24 is reduced. At $\beta=100°$ the negative peak shown for cell 18 probably results from the combination of the remnants of the incident vortex and the eruption of the surface vortex. The convection of tip vortex A can be readily observed by the movement of the positive peak in $\beta=60°$ to $120°$.

4.1.3 Streamline Patterns in the Moving Reference Frame

Unlike vorticity contours, streamline patterns depend on the frame of reference. Figure 4.5 shows a series of streamline patterns for a reference frame moving at the convection speed of the incident vortex, as calculated for $\beta=0°$ in the manner described in Chapter 3. Furthermore, these patterns have been smoothed by removing any structures of length scales smaller than 6 mm using a spatial filtering routine developed in-house (refer to section 2.4).

For $\beta=340°$ to $20°$ the incident vortex is clearly evident on the left side of the image as it approaches the tip of the stationary leading-edge and then experiences compression in the x-direction and stretching in the y-direction as the initial shape of the vortex distorts. As reviewed in Chapter 3, the center region of the vortex core initially shows a topology indicating two-dimensional flow but changes to an unstable focus at $\beta=0°$, indicating compression and three-dimensional flow along the z-axis of the incident vortex. at $\beta=20°$ it appears that the incident vortex begins to diminish in size and strength until finally at $\beta=40°$, the focus of the incident vortex disappears and only streamlines with more curvature are visible.

Also evident for $\beta=340°$ to $20°$ is a pair of saddle points: one located above the

52

upper surface of the wedge and another below the center of the incident vortex on the bottom edge of the image. At $\beta=340°$, streamlines appear to be nearly vertical between them, forming an alleyway. For $\beta=0°$ to $20°$, this alleyway is cutoff by the approaching incident vortex where some streamlines originating on the upper wedge surface are bent around the incident vortex, but none are entrained within it. At $\beta=40°$ the saddle point above the upper surface disappears.

Along the lower surface of the wedge, at $\beta=340°$, the tip vortex initially exhibits two-dimensional flow within its core. The streamline at the tip that emanates from the upper surface of the wedge appears to be drawn within the tip vortex. Just to the right of the tip vortex is a saddle point-stable focus combination which disappears at $\beta=20°$. At $\beta=0°$ to $40°$, the tip vortex remains a stable focus, indicating there is three-dimensional flow along the z-axis due to axial stretching. The streamline at the tip, extending to the upper surface of the edge, continues to be entrained within the tip vortex until $\beta=40°$, when it deflected away by the incident vortex. At $\beta=40°$, the tip vortex is the dominant flow feature near the leading-edge.

4.1.4   Streamline Patterns in the Laboratory Reference Frame

Figure 4.6 depicts the streamline patterns in the laboratory reference frame, corresponding to the velocity field of figure 4.7. In figure 4.6, the incident clockwise vortex can be identified by the wave-like curvature of the streamlines upstream of the leading-edge, visible until $\beta=40°$. The stagnation point can be seen on the upper surface of the wedge at a location near the tip for $\beta=340°$ to $0°$, and may be considered as a half-saddle point. At $\beta=20°$ the saddle point moves above the upper surface and further aft as the incident vortex collides with the tip of the leading-edge. The streamlines along the upper surface near the tip are no longer parallel to the surface, but almost perpendicular, indicating that flow is away from the surface before sweeping around the tip toward the

lower surface. At $\beta=40°$ the saddle point moves toward the tip of the leading-edge until at $\beta=60°$, the saddle point appears nearly coincident with the tip. From $\beta=80°$ to $120°$ a clear saddle point is not apparent but a stagnation streamline is visible near the tip on the lower surface of the wedge, moving further aft at $\beta=120°$.

On the lower surface, the tip vortex begins to grow in size from $\beta=340°$ to $20°$, appearing as an unstable focus nested within a stable limit cycle. The tip vortex splits into two sections at $\beta=40°$, rather than at $\beta=80°$ as indicated in the vorticity contours described in the foregoing section. A saddle point occurs between a stable node near the tip and an unstable focus nested within a stable limit cycle further downstream. The tip vortex does not appear to convect downstream until $\beta=60°$, when the nested, unstable focus also changes to a stable focus within an unstable limit cycle. The stable node disappears. At $\beta=80°$ to $120°$ the stable focus corresponds to the portion of the tip vortex previously denoted as vortex "A" and continues to convect downstream along the lower surface, being first an unstable focus, changing its topology to concentric circles nested within a stable limit cycle, then reverting back to an unstable focus. The saddle point previously seen between the stable node and the nested unstable focus becomes a half-saddle point on the lower surface and also convects along the surface with vortex A.

4.2 Concluding Remarks

Interactions of a clockwise rotating vortex with a stationary leading-edge has been examined using instantaneous velocity fields obtained in a time sequence with 0.140 second intervals. Both the streamline topology and the vorticity distributions show the approach, deformation and splitting of the incident vortex and the generation of a tip vortex on the lower surface of the leading-edge. In addition, streamline topology shows that the stagnation line moves from the upper to the lower surface of the leading-edge.

54

Similar flow features have been suggested qualitatively in the earlier investigations by Ziada and Rockwell (1982), Kaykayoglu and Rockwell (1985), Gursul and Rockwell (1990), Booth (1990) and Wilder (1992), as reviewed in Chapter 1, and more recently modelled numerically by Kaya and Kaykayoglu (1996) using a discrete vortex technique. The present study provides the first quantitative description of the distinctive features of the vortex-edge interaction.

The streamline topology of the incident vortex reveals that the core changes from a two-dimensional to a three-dimensional state as it approaches and begins to collide with the leading-edge. As the vortex distorts around the tip, the unstable focus disappears in the moving reference frame, suggesting that the incident vortex ceases to be a coherent structure and its effect on the flow development near the leading-edge is minimized. Subsequent vorticity distributions of the incident vortex show that the portion of the incident vortex passing below the surface of the edge is distended by the development of the tip vortex, leading to its fragmentation as it convects downstream. The portion of the incident vortex on the upper surface appears to retain a higher concentration of vorticity than the surrounding boundary layer, but tends to dissipate as it convects downstream.

Streamline patterns in the laboratory frame show the interesting behavior of the flow near the tip of the leading-edge. As the incident vortex approaches, the stagnation line on the upper surface becomes a half-saddle point on the surface, then becomes a saddle point as it rises above the tip. As this occurs, streamlines very near the tip appear almost orthogonal to the surface in the region immediately above the surface, then sweep around the tip toward the lower surface. This pattern may indicate a large suction force on the lower surface of the tip. After the incident vortex collides with the leading-edge, the saddle point coincides with the tip at $\beta=60°$. Subsequently, the stagnation point moves to the lower wedge surface.

Plots of the local circulation on the lower surface as well as the vorticity distribution show that the tip vortex forms with two peaks of vorticity on the lower wedge surface. As the tip vortex grows, these peaks become more pronounced, inducing a region of opposite sign vorticity (negative) which later forms a surface vortex. The tip vortex begins to convect downstream at the moment the stagnation line is coincident with the tip of the leading-edge. After the splitting of the tip vortex into two vortices A and B, both A and B convect at the same rate but the larger vortex A begins to move away from the lower surface while B convects along the surface.

Taken together, the streamline topology and vorticity distributions provide a complete picture of the process of splitting the tip vortex. From the streamline patterns in the fixed laboratory frame, the tip vortex splits at $\beta=40°$, at which a saddle point divides the two vortices. This saddle point moves to the lower surface of the edge at $\beta =80°$, the instant when the vorticity contours show the tip vortex splits.

Determination of the circulation of the incident, tip and surface vortices reveals a significant relationship. The circulation of the tip vortex grows as the incident vortex approaches the leading-edge, reaching a magnitude greater than that of the incident vortex. The circulation of the surface vortex increases as the circulation of the tip vortex grows, but its magnitude is always much less than that of the tip vortex. After the tip vortex splits into two vortices A and B, the circulation of A is much larger than B, but their sum nearly equals that of the tip vortex prior to splitting. This implies that vorticity ceases to be fed into the tip vortex before splitting. The transient process associated with this cessation of vorticity flux may result in the two distinct vortices A and B. This hypothesis contrasts with the view that the surface vortex actually cuts off the supply of vorticity into vortex A.
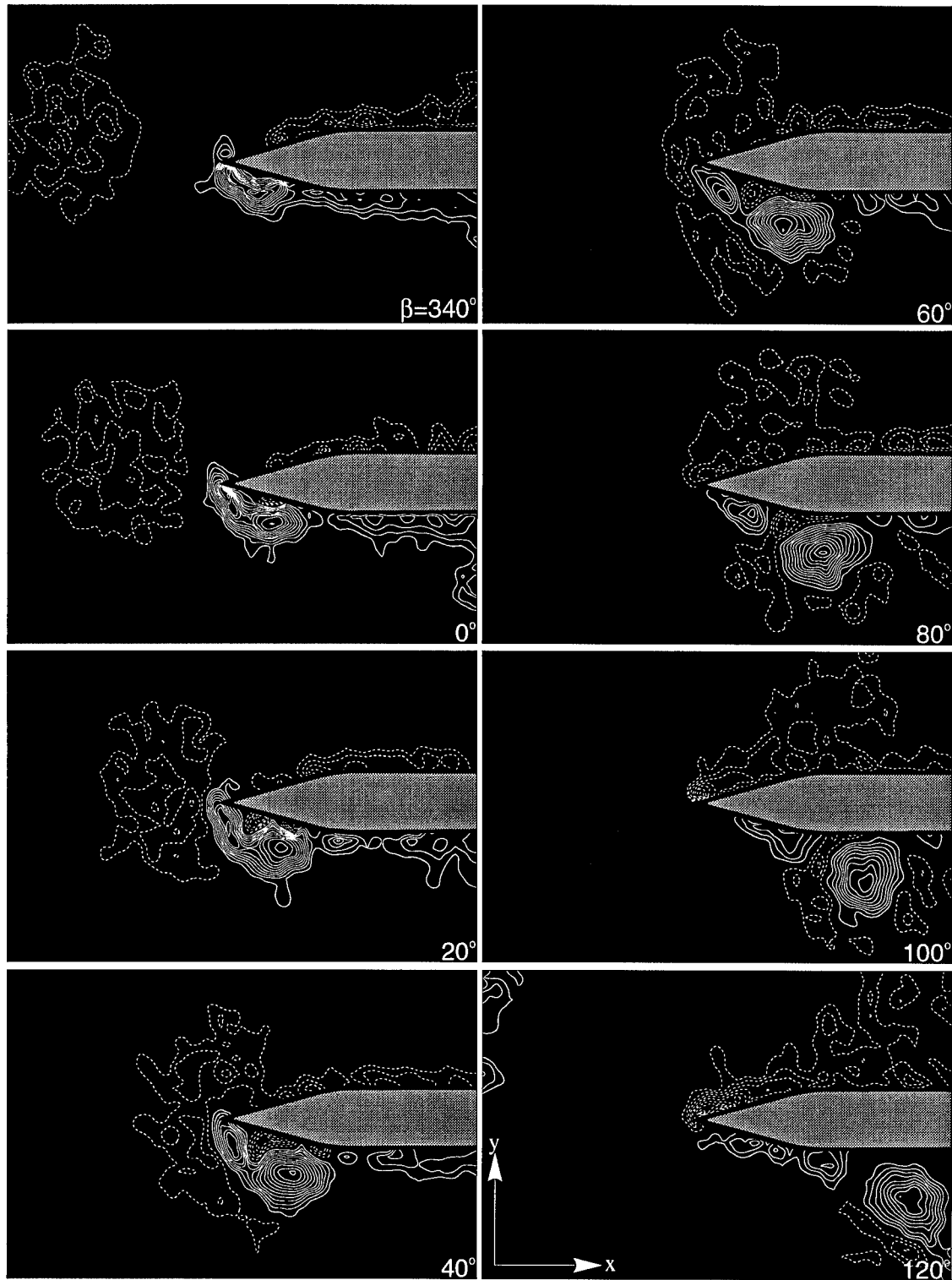
Figure 4.1: Instantaneous vorticity distributions for a stationary leading-edge at a=0° with an incident clockwise vortex. Re= 6,250. Contours of negative vorticity, corresponding to clockwise rotation, are denoted as dashed lines, while positive vorticity is represented by solid lines. Minimum and incremental contour levels are $|\omega_{min}| = 5 \text{ sec}^{-1}$ and $\Delta\omega = 5 \text{ sec}^{-1}$.
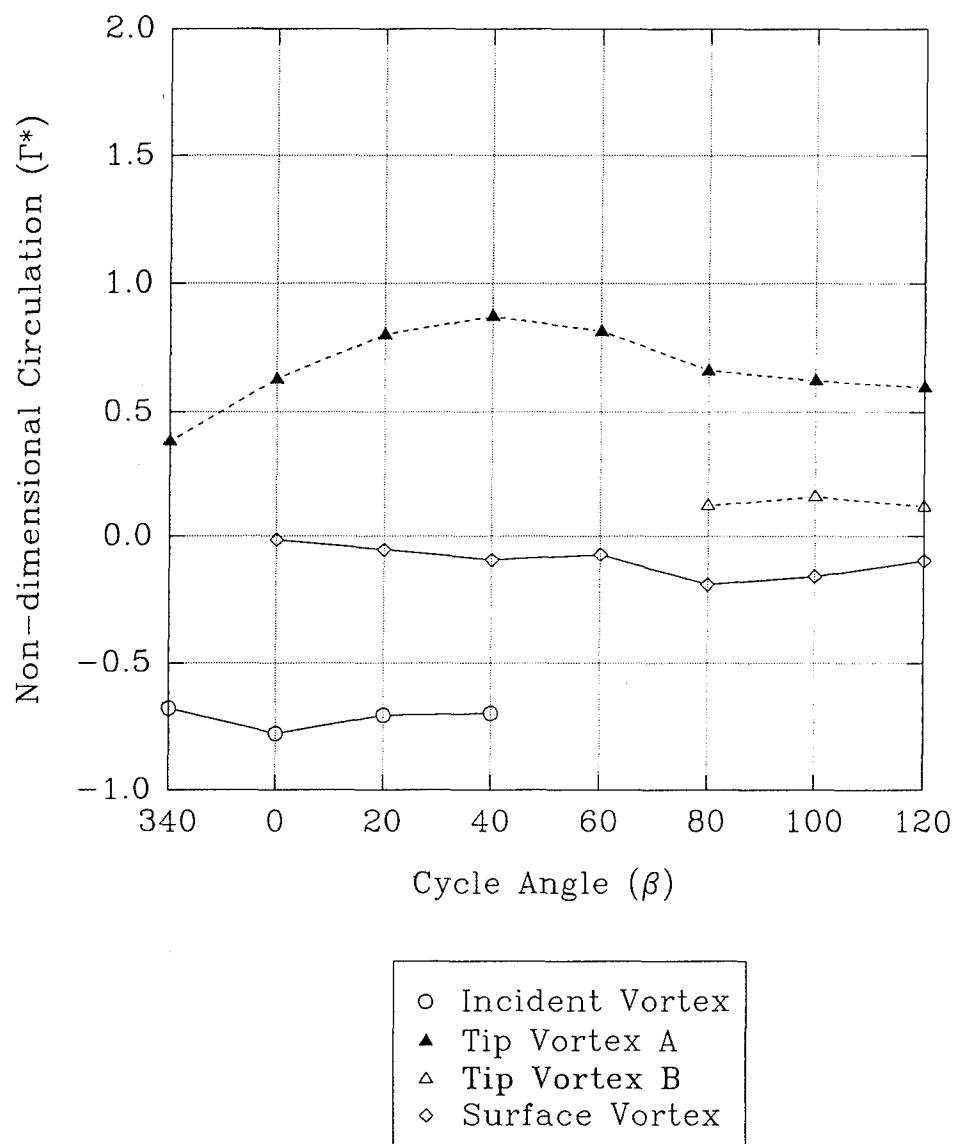
Figure 4.2: Non-dimensional circulation of the incident, tip and surface vortices for a stationary leading-edge at $\alpha=0°$
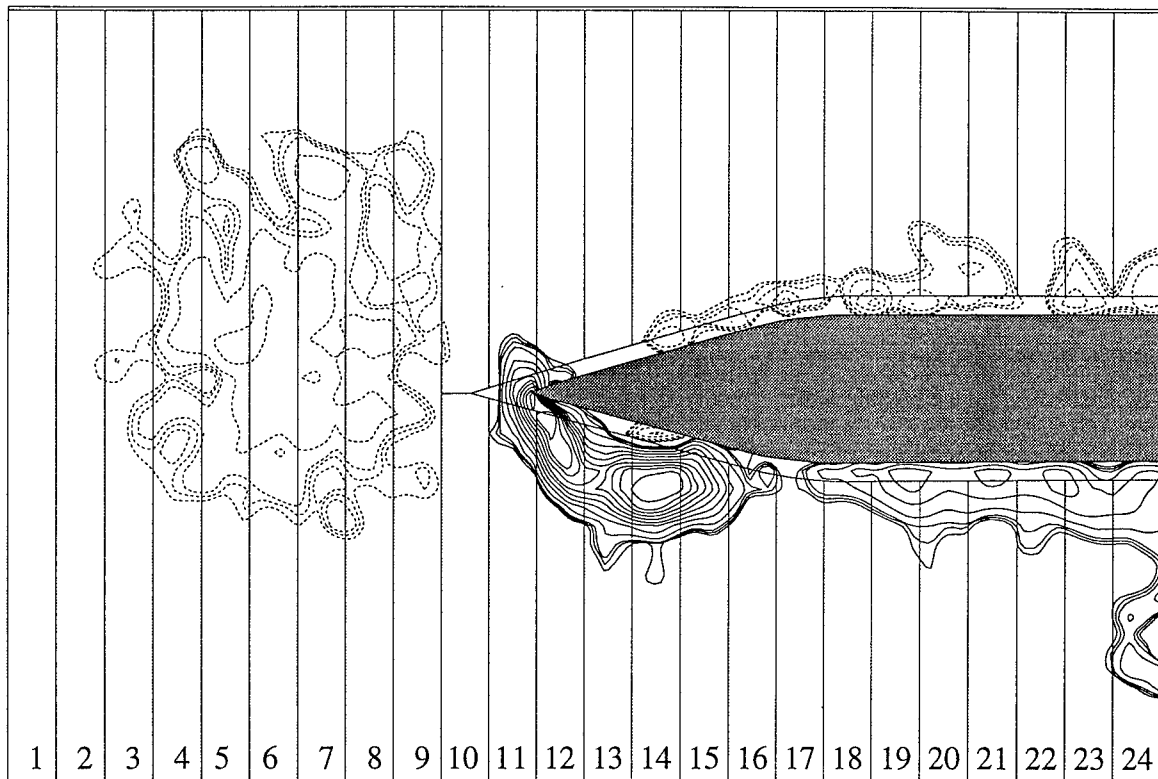
Figure 4.3: A representative plot of the locations of the local circulation cells overlaid on the instantaneous vorticity distribution for the case of a stationary leading-edge at ß=0°. Cells above and below the surface are used for locations 10-24.
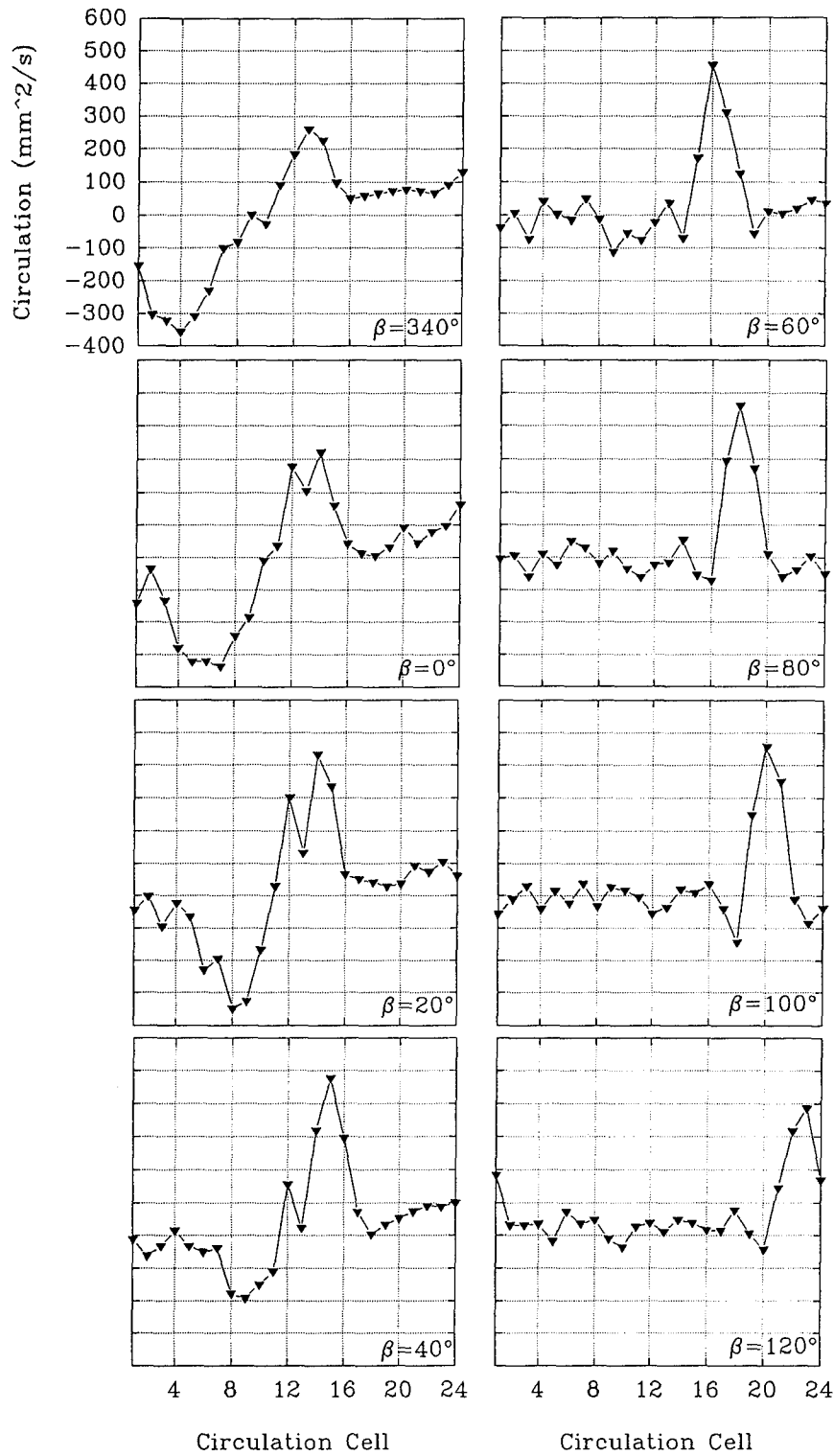
Figure 4.4: Local circulation upstream of and along the lower surface of a stationary leading-edge at α=0°
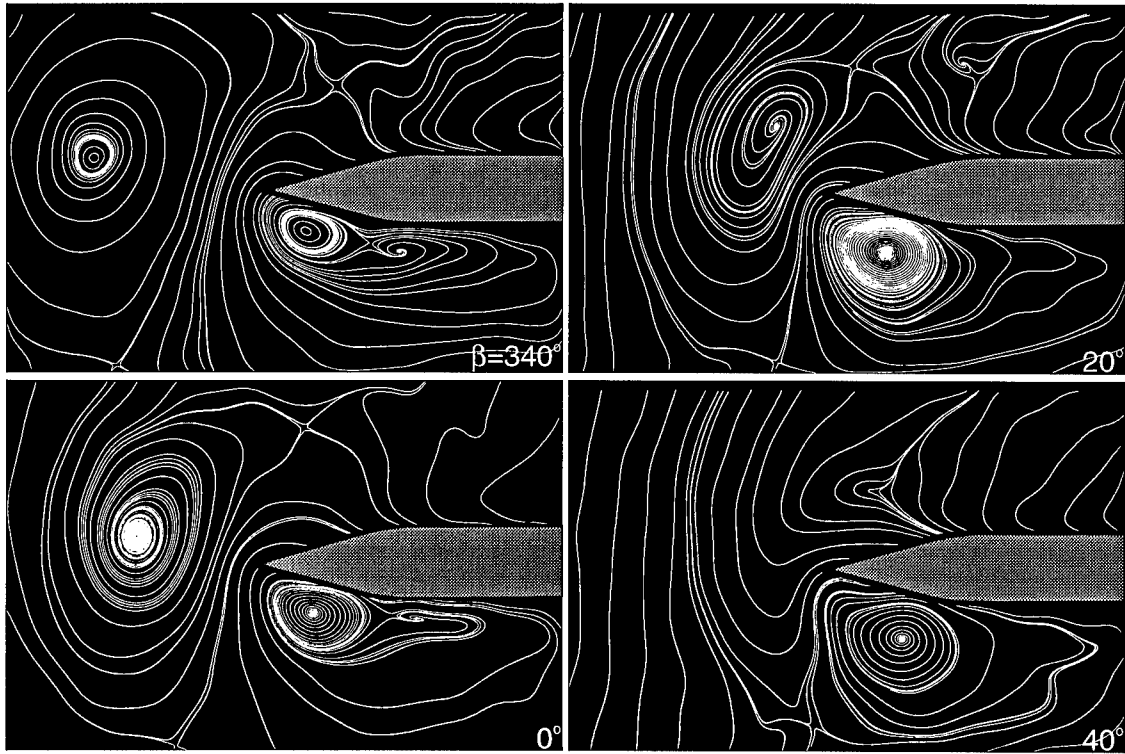
Figure 4.5: Streamline patterns in a reference frame moving at $U/U_\infty = 0.9$ for a clockwise vortex incident upon a stationary leading-edge.
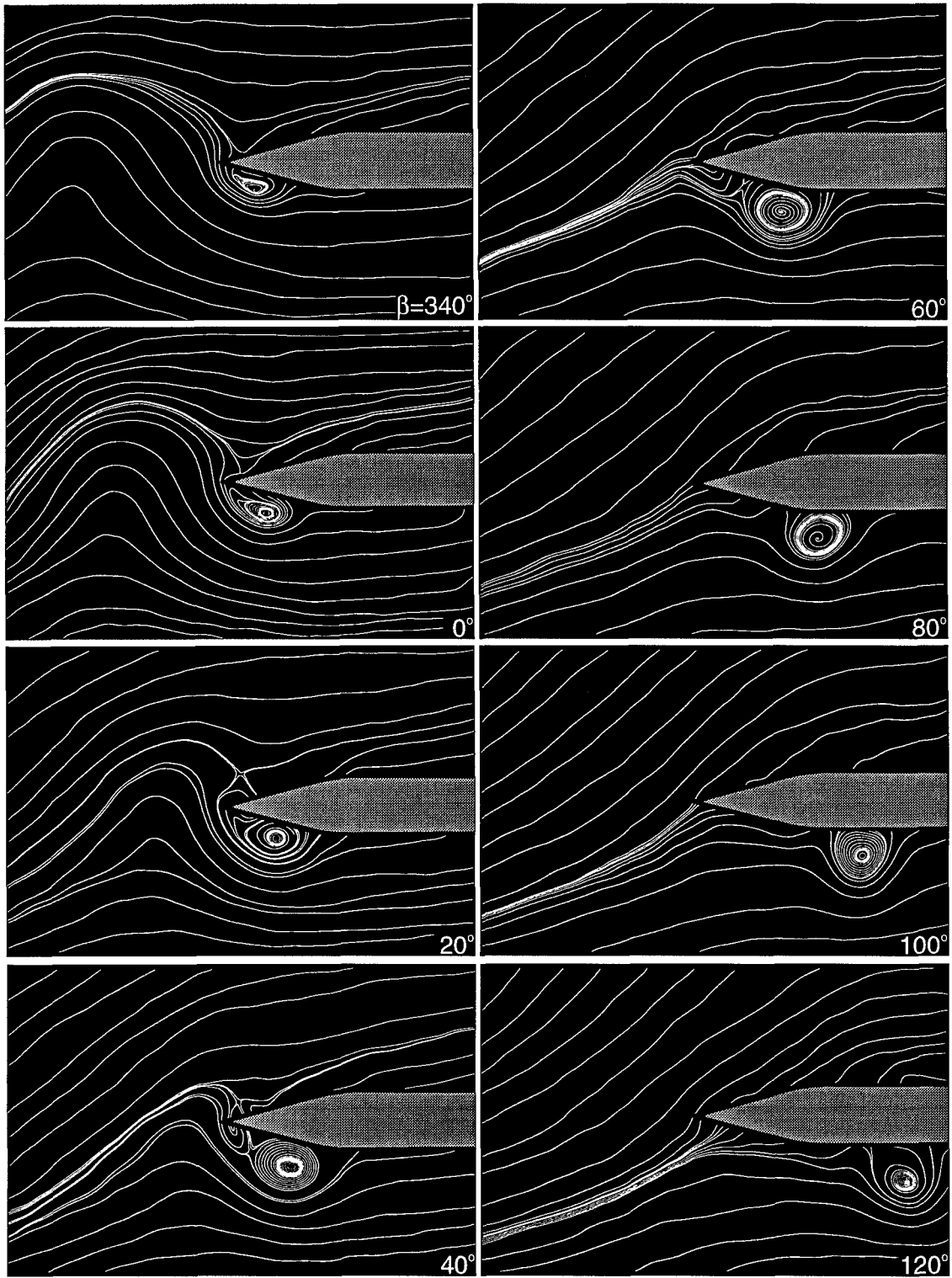
Figure 4.6: Streamline patterns in the laboratory reference frame for a stationary leading-edge with an incident clockwise vortex.
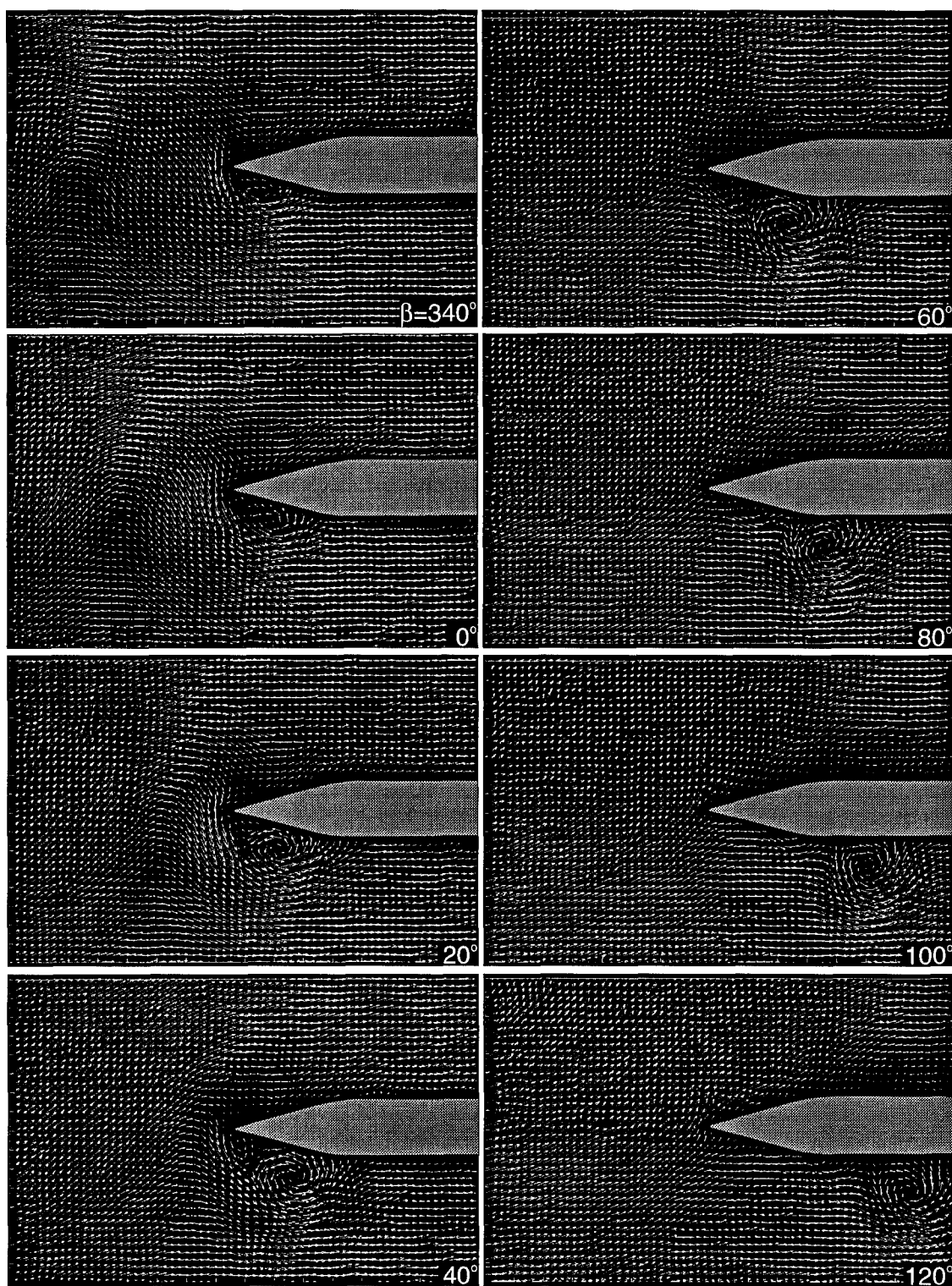
Figure 4.7: Instantaneous velocity field for a clockwise vortex impinging upon a stationary leading-edge at $\alpha=0°$.

5.0 VORTEX INTERACTION WITH AN OSCILLATING LEADING-EDGE

In Chapter 4, results of an incident vortex impinging upon a stationary leading-edge were presented. In this chapter, the structure and development of the flow past an oscillating leading-edge are described in much the same way, using a time sequence of PIV data. The case of an oscillating leading-edge in the absence of an incident vortex will provide a basis for comparison of the interaction mechanisms for a leading-edge oscillating at phase angles $\phi=0°$ and $\phi=180°$ with respect to an incident clockwise vortex. The flow structure of the interaction will then be compared at two values of Reynolds number.

5.1 Flow Structure for an Oscillating Leading-Edge without an Incident Vortex

5.1.1   Instantaneous Vorticity Distributions

Contours of constant vorticity for the oscillating leading-edge beginning at $\beta=340°$ are shown in figure 5.1 where dashed lines represent contours of negative vorticity corresponding to clockwise rotation, and solid lines denote contours of positive vorticity. At $\beta=0°$, the leading-edge is at an instantaneous angle-of-attack $\alpha=0°$ as it pitches upward. Although not shown, the maximum angle-of-attack of five degrees occurs at $\beta=90°$. Consequently, the leading-edge is at the same instantaneous angle-of-attack at, for example, $\beta=80°$ and $\beta=100°$ but the direction of motion differs.

In the three images corresponding to $\beta=340°$, $0°$ and $20°$, the development of a tip vortex along the lower surface initiates on the upper surface of the wedge very near its tip, suggesting that the stagnation line lies on the upper surface between the positive and negative concentrations of vorticity. As the tip vortex grows, two concentrations of vorticity can be identified on the lower surface of the wedge. In addition, a surface

64

vortex begins to develop on the lower surface at $\beta=0°$. It is located between the two vorticity peaks of the tip vortex. At $\beta=40°$, the tip vortex splits into larger and smaller concentrations, designated as "A" and "B", respectively. Vortex B still shows vorticity along the upper surface and appears to contain two vorticity peaks. It is interesting to note that the surface vortex remains confined to a region near the surface and does not erupt out into the flow, as has been observed in other vortex-wall interactions.

If the stagnation line is assumed to exist in the gap between concentrations of positive and negative vorticity along the upper surface of the wedge, this line moves towards the tip of the leading-edge and tip vortex B moves downward to the lower surface at $\beta=60°$. The tip vortices A and B, and surface vortex all begin to convect downstream at this cycle angle, maintaining the same relative positions with respect to each other. At $\beta=80°$ the stagnation line shifts to the lower wedge surface and vortex B coalesces into a vortex with one vorticity peak. Simultaneously, along the upper surface, concentrations of negative vorticity begin to accumulate near the tip. For $\beta=100°$ and 120°, the tip vortices A and B continue to convect along the surface while the surface vortex detaches from the shoulder region of the lower surface. Negative vorticity continues to accumulate on the upper wedge surface near the tip.

Figure 5.2 compares vorticity distributions at selected values of cycle angle β from the first half of the oscillation cycle with those from the second half of the cycle. The left column shows excerpts of the vorticity distributions found in figure 5.1, while the right column shows vorticity distributions for cycle angles that differ by 180° from those in the left column. By comparing these cycle angles, it can be seen that the flow structure about the oscillating leading-edge is nearly symmetric, as expected for an undisturbed freestream.

5.1.2 Evolution of Circulation

The circulation of the tip and surface vortices is plotted in figure 5.3 for cycle angles $\beta=340°$ to $120°$ and in figure 5.4 for $\beta=160°$ to $300°$. In figure 5.3, the circulation of the tip vortex increases with increasing cycle angle β. As seen in figure 5.1, the tip vortex splits at $\beta=40°$ and the summation of the circulation for both A and B nearly equals the circulation of the tip vortex just prior to splitting. As seen in the last chapter, this indicates that vorticity ceases to accumulate within the tip vortex before it splits. The surface vortex maintains a small and nearly constant value of circulation. The same trends noted for figure 5.3 are also evident in figure 5.4 with the exception that the tip vortex does not reach as high a magnitude before splitting. In addition, the tip vortex is seen to split at $\beta=240°$, one cycle interval later relative to the $\alpha=0°$ symmetry condition ($\beta=0°$, $180°$), than the split shown in figure 5.3.

The local circulation upstream of the edge and along its lower surface is shown in figure 5.5 as a time sequence for $\beta=340°$ to $120°$. (See figure 4.3 for a definition of the cell grid.) The tip vortex can be clearly distinguished by the curves of local circulation, including the two peaks of vorticity seen in figure 5.1 within the vortex before it splits. From the levels of local circulation at $\beta=20°$ to $40°$, it appears that some circulation is transferred from the upstream peak to the downstream peak, which corresponds to tip vortex A as the tip vortex splits.

5.1.3 Streamline Topology in the Laboratory Reference Frame

Streamline patterns in the fixed laboratory frame are shown in figure 5.6 for $\beta=340°$ to $120°$ and the corresponding instantaneous velocity fields are shown in figure 5.7. Referring to figure 5.6, a half-saddle or saddle point is visible very near the tip of the leading-edge on the upper surface for $\beta=0°$ to $40°$. At $\beta=20°$, the streamlines very close to the tip are nearly orthogonal to the surface and sweep around the tip toward the lower

66

surface. The saddle point disappears and the upstream streamlines appear to abruptly change their angle of approach toward the oscillating leading-edge at $\beta=60°$. This induces a much larger, positive angle-of-attack with a stagnation line very close to the tip. The stagnation line continues to remain on the lower surface close to the tip for the remaining values of cycle angle β.

The tip vortex along the lower surface corresponds to a combination of a saddle point and an unstable focus, which is first identifiable at $\beta=340°$. At $\beta=0°$ only, an unstable node appears on the lower surface upstream of the saddle-unstable focus combination and represents the upstream portion of the tip vortex. Later in the cycle, for $\beta=80°$ to $100°$, the unstable focus changes to a set of nested limit cycles. These revert back to an unstable focus at $\beta=120°$, during which the saddle point of the combination becomes a half-saddle point along the lower surface.

5.1.4   Concluding Remarks

The development, splitting and convection of a tip vortex and the formation of a surface vortex can be clearly seen in the vorticity distributions. The vorticity distribution shows that the tip vortex splits at $\beta=40°$. From $\beta=20°$ to $40°$, a shift in local circulation distribution occurs within the tip vortex, suggesting that within the tip vortex itself, vorticity transfers from one vorticity peak to another as the tip vortex splits. The sum of the circulation of tip vortices A and B nearly equals the circulation of the tip vortex before splitting and suggests that the vorticity flux from the tip region ceases prior to the occurrence of vortex splitting. The surface vortex remains at a nearly constant level of circulation and does not appear to erupt into the external flow when the tip vortex splits. The vorticity distributions, plots of total vortex circulation, as well as local circulation, all show a nearly symmetric flow development of the oscillating leading-edge about the instantaneous $\alpha=0°$ position.

The instantaneous vorticity distributions and streamline topology both indicate that the stagnation point moves from the upper to the lower surface, while remaining very near the tip, for $\beta=340°$ to $120°$. The corresponding streamline topologies show that the larger tip vortex A generally is a combination of a saddle point-and an unstable focus. The tip vortex B is not distinguished by a critical point but only by streamline curvature. The topology does not indicate a split in the tip vortex at the same instant shown in the vorticity distribution. The onset of a saddle point adjacent to an unstable focus along the lower surface early in the oscillation cycle suggests the tip vortex splits much earlier than the vorticity distributions indicate. The streamline topology, vorticity distributions and plots of local circulation all show that the tip vortex begins to convect downstream at $\beta=60°$. Also, beginning at $\beta=60°$, the angle of incidence of the streamlines increases abruptly, coinciding with the shift of the stagnation line to the lower surface.
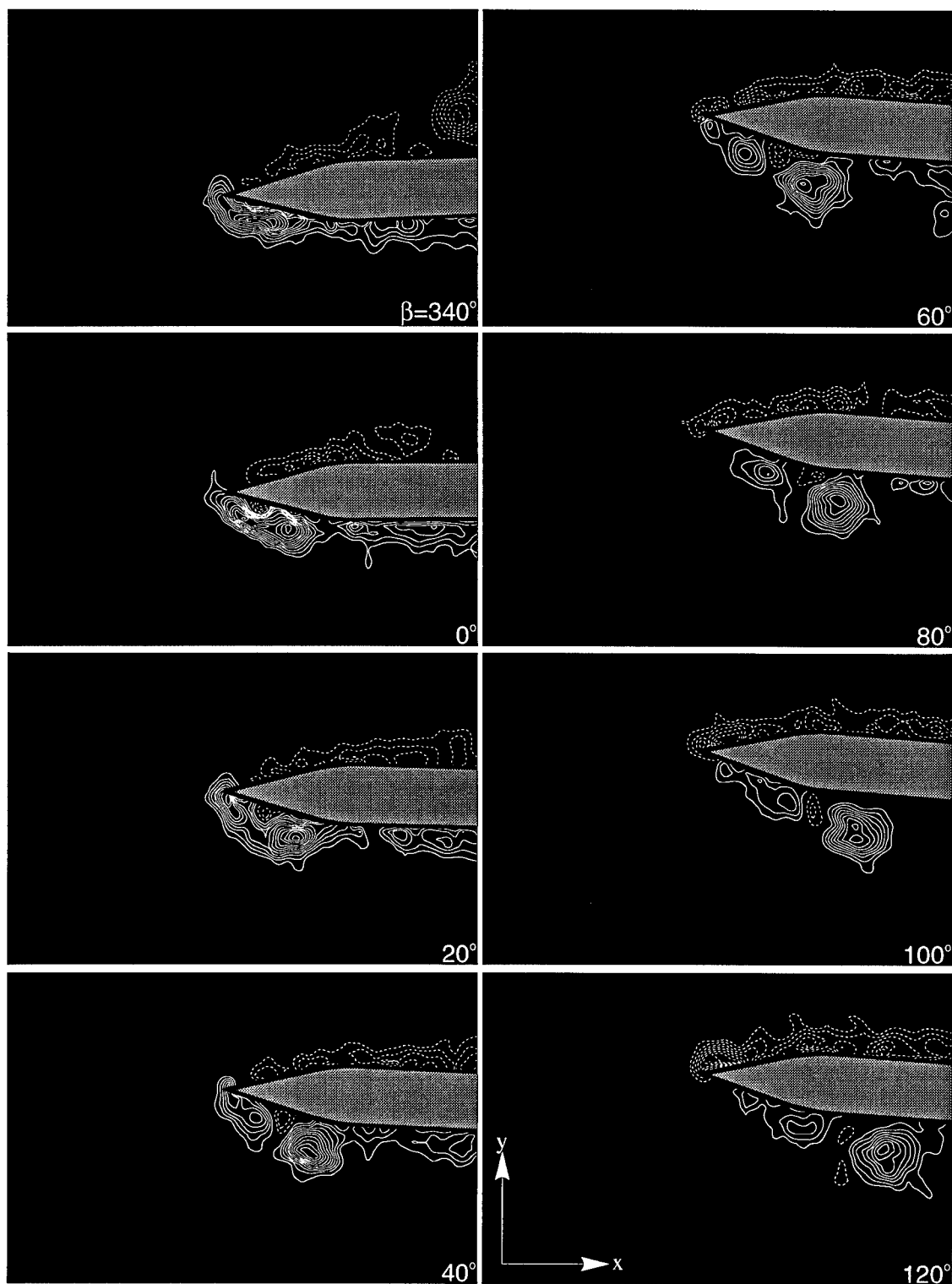
Figure 5.1: Instantaneous vorticity distributions for an oscillating leading-edge without an incident vortex. $|\omega_{min}| = 5$ sec^{-1} $\Delta\omega = 5$ sec^{-1}. Re= 6,250.

69
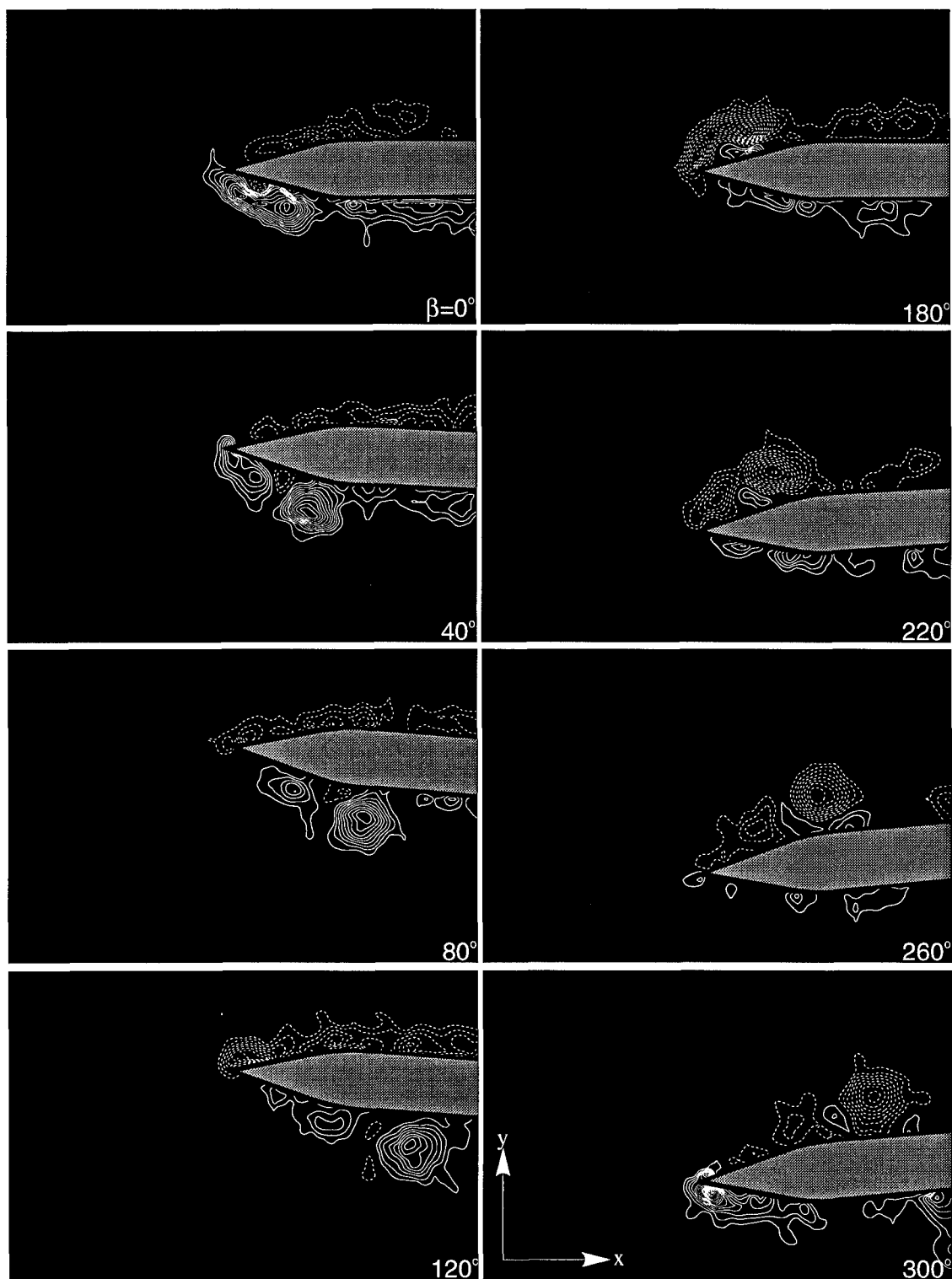
Figure 5.2: Instantaneous vorticity distributions showing symmetric vortex development for an oscillating leading-edge without an incident vortex. $|\omega_{min}| = 5$ sec^{-1}; $\Delta\omega = 5$ sec^{-1}. Re= 6,250.
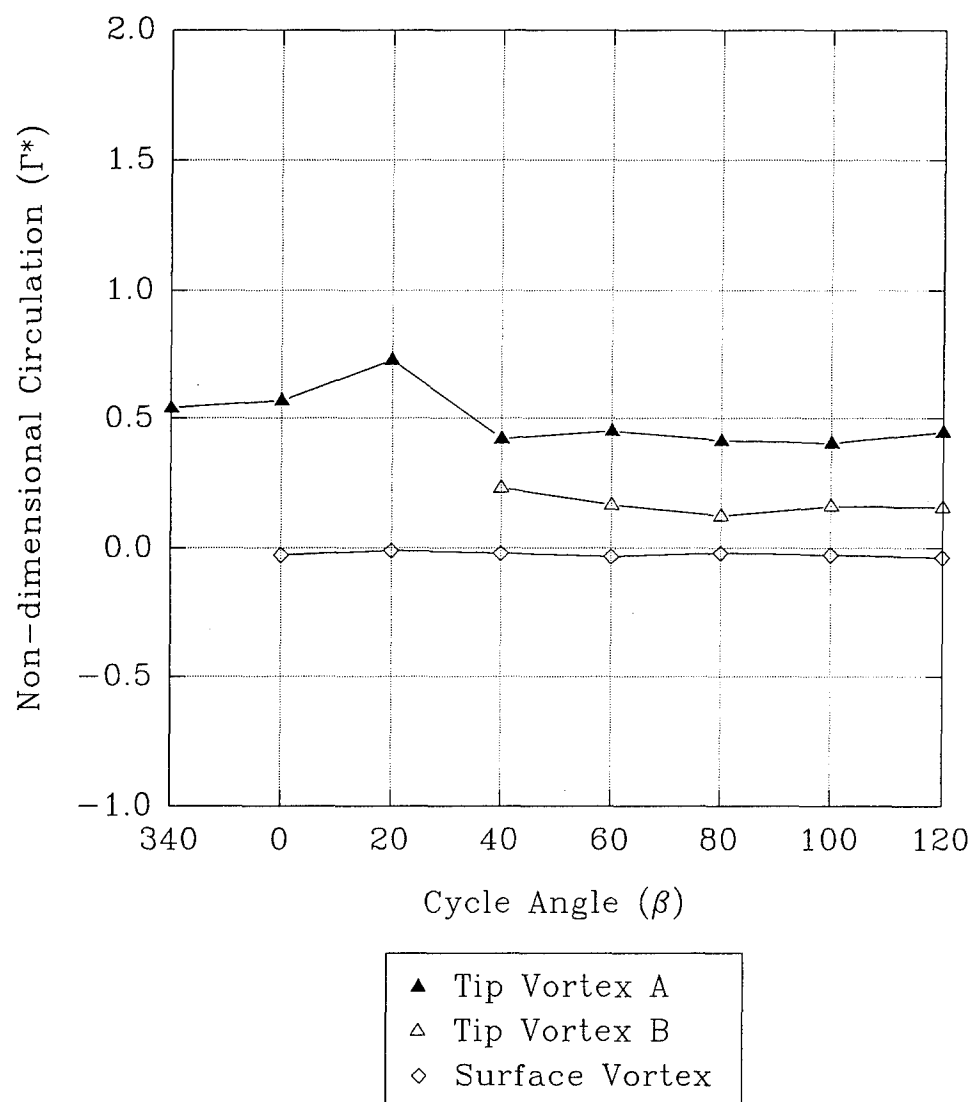
Figure 5.3: Non-dimensional circulation of the tip and surface vortices for an oscillating leading-edge without an incident vortex (β=340° to 120°)

71
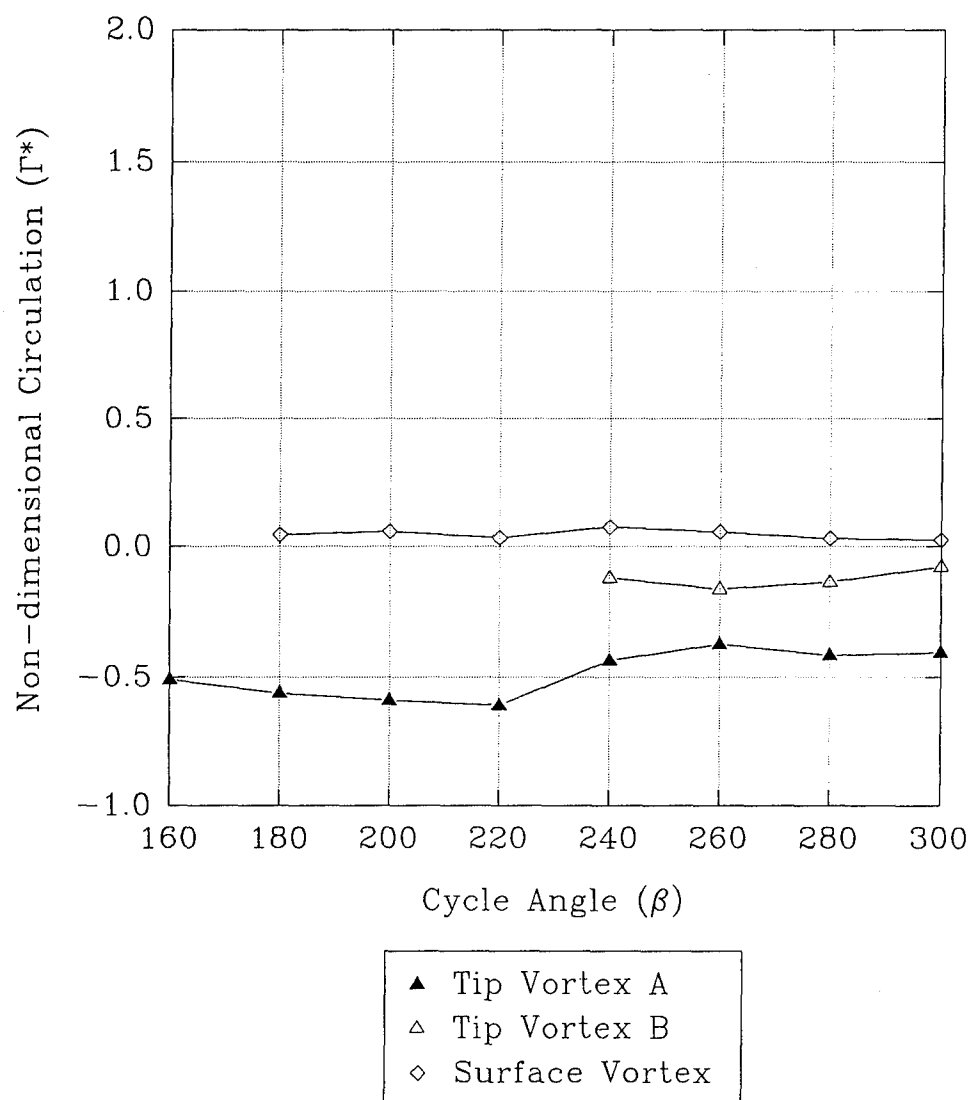
Figure 5.4: Non-dimensional circulation of the tip and surface vortices for an oscillating leading-edge without an incident vortex ($\beta=160°$ to $300°$)
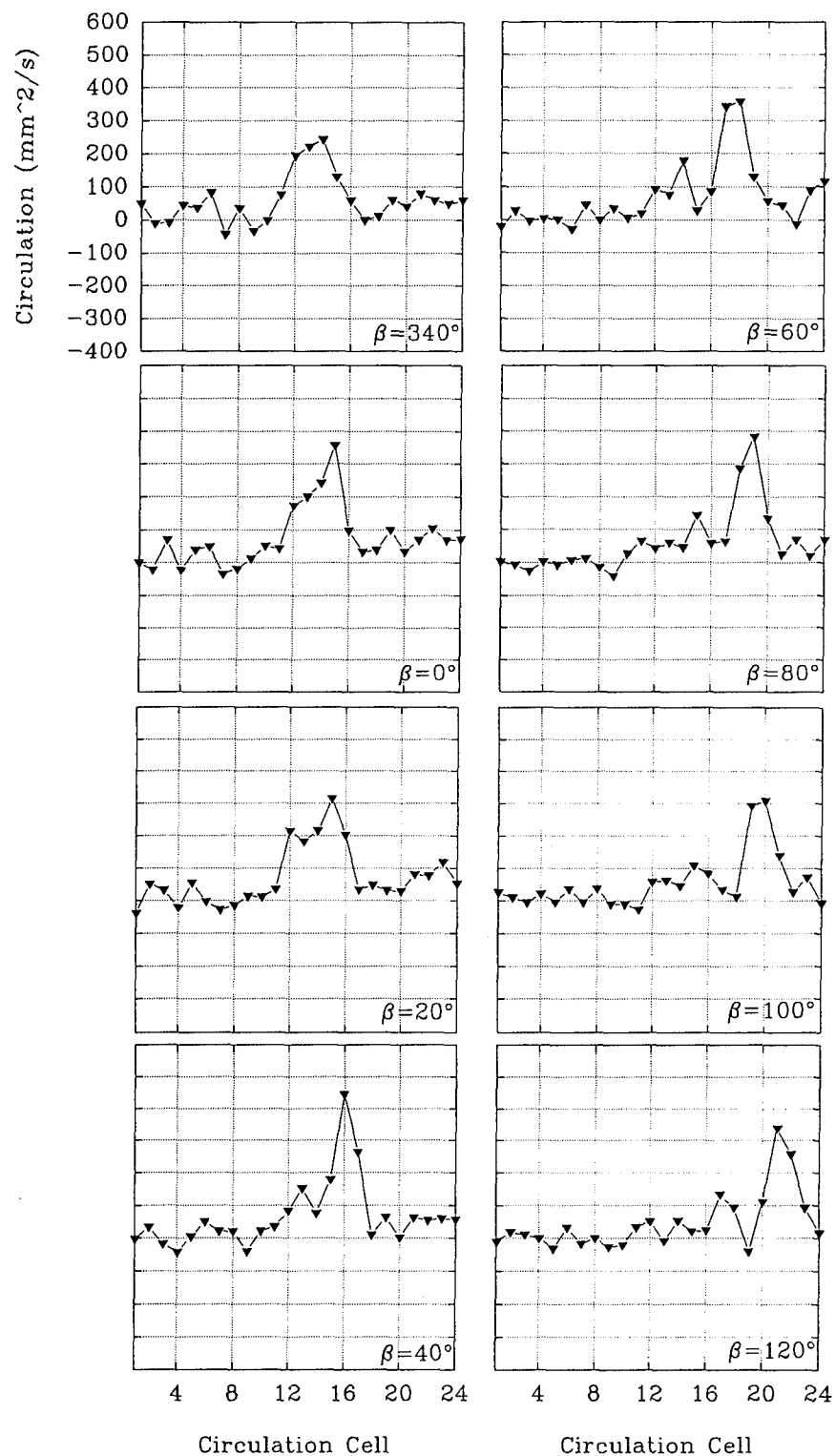
Figure 5.5: Local circulation upstream and along the lower surface of an oscillating leading-edge without an incident vortex
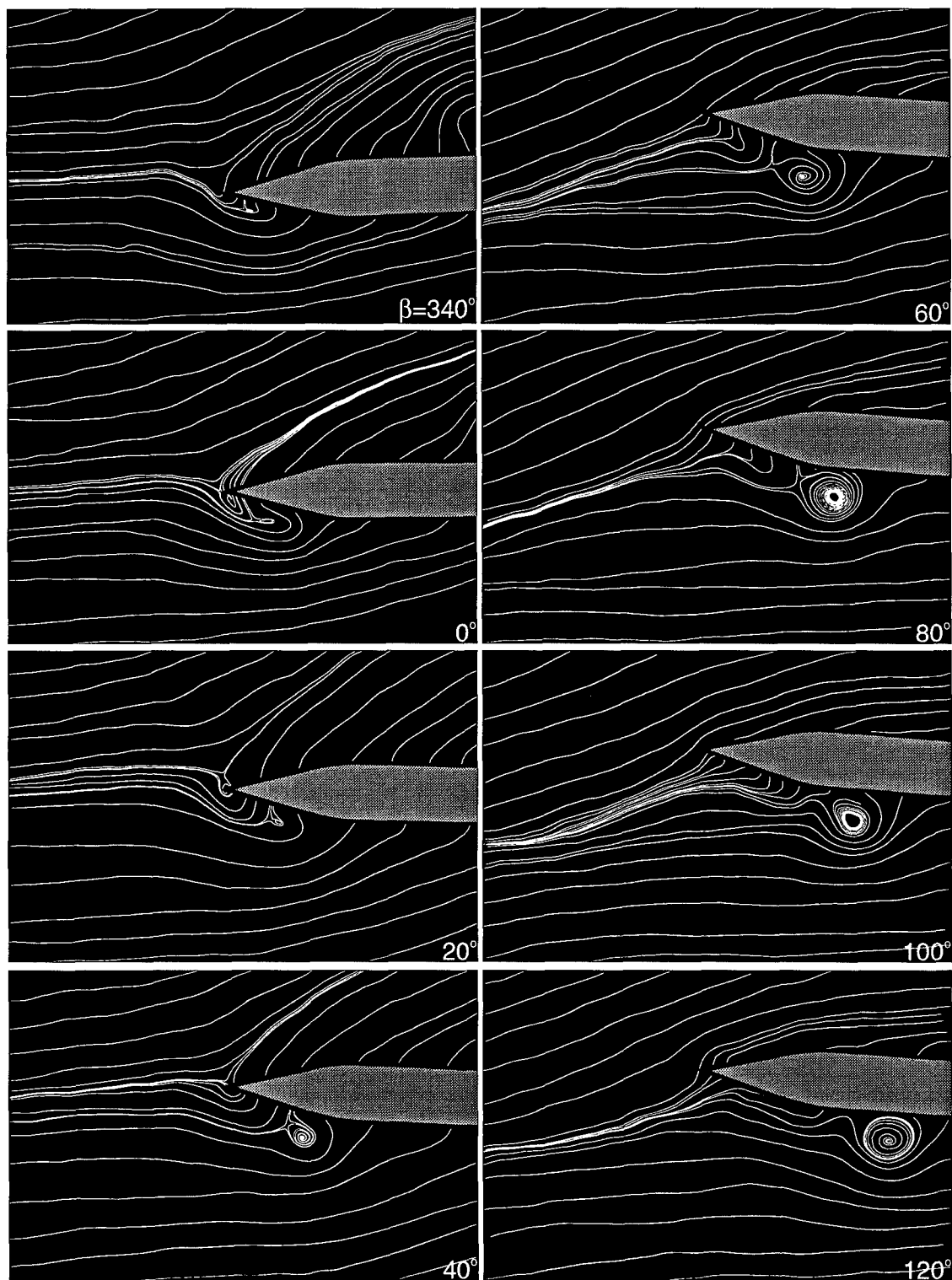
Figure 5.6: Streamline patterns in the laboratory reference frame for an oscillating leading-edge without an incident vortex. Re= 6,250.
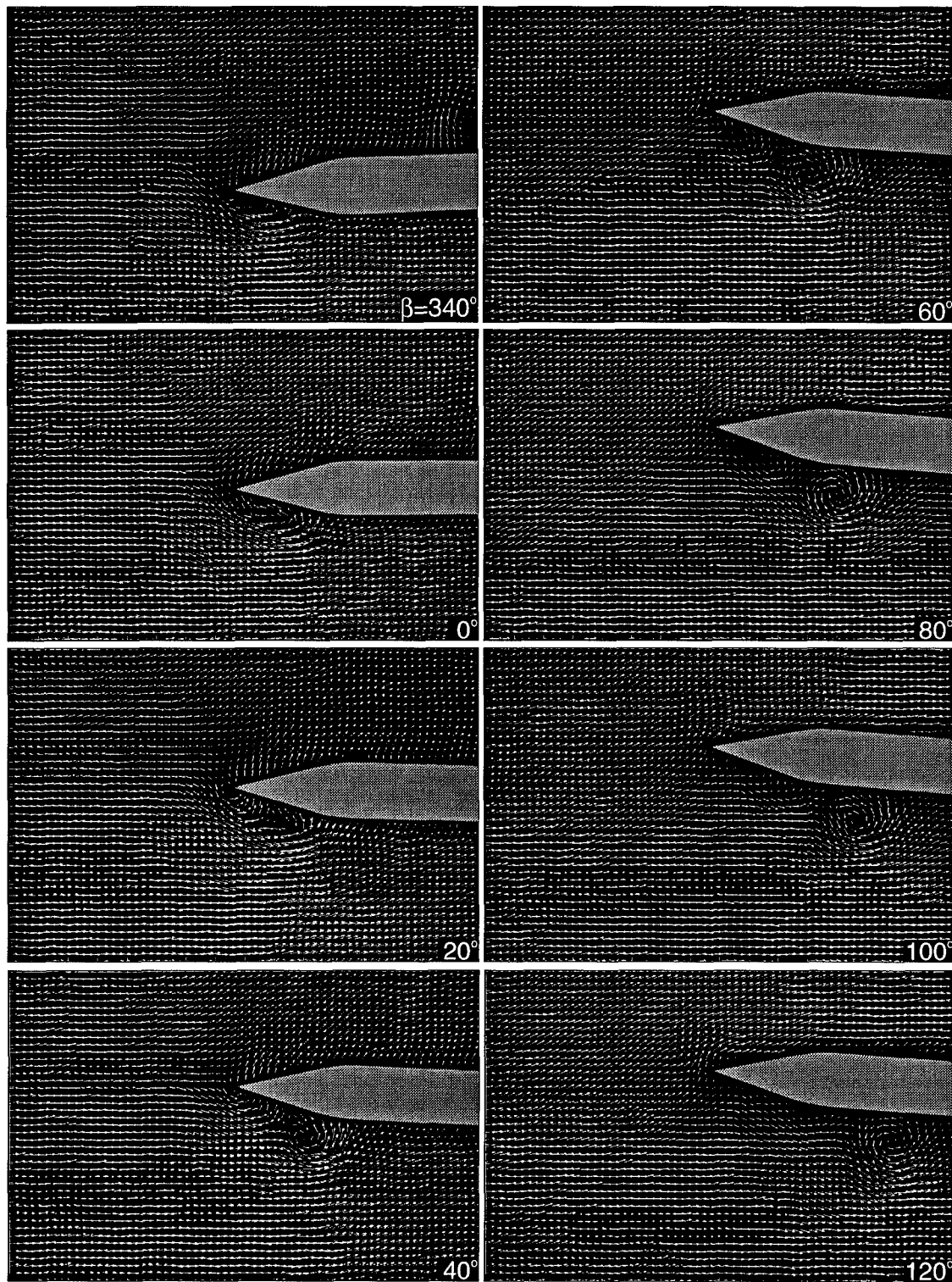
Figure 5.7: Instantaneous velocity field of an oscillating leading-edge without an incident vortex. Re= 6,250.

75

5.2 Vortex Interaction with an Oscillating Leading-Edge at Zero Phase Shift ($\phi=0°$)

5.2.1 Instantaneous Vorticity Distributions

Figure 5.8 shows the vorticity distributions obtained from the instantaneous velocity fields for the case of a leading-edge oscillating at a phase angle $\phi=0°$ with respect to an incident clockwise vortex. The phase angle is essentially equal to the cycle angle β of the oscillating leading-edge at the instant that the center of the incident vortex is within one vortex diameter of the leading-edge. Therefore, at $\beta=0°$ in figure 5.8, the leading-edge is at $\alpha=0°$ during its upstroke. (Refer to section 2.2 for a detailed definition of the phase angle ϕ).

Much of the flow development shown in figure 5.8 is similar to that described in Chapter 4 for a stationary leading-edge but is more pronounced and at a larger scale. The clockwise rotating vortex approaching the leading-edge is discernible by the contours of negative vorticity (dashed lines) visible on the left side of each image for $\beta=340°$ to 20°. At $\beta=20°$, the initial compression of the incident vortex in the x-direction and elongation in the y-direction can be seen as the vortex collides with the edge. Very severe distortion and stretching of the incident vortex by the tip vortex on the lower surface is shown in $\beta=40°$ to 100°, with perhaps a quarter of the incident vortex convecting along the upper surface. As the lower section of the incident vortex is distended by the development of the tip vortex, it breaks into smaller concentrations of vorticity, which continue to convect downstream. At $\beta=120°$, the contours of positive vorticity (solid lines) visible on the upper left side of the image show a portion of the approaching counter-clockwise vortex.

At $\beta=340°$, both the tip vortex and the surface vortex appear to be well developed. The tip vortex exhibits two peaks of vorticity. In a peculiar way, the tip vortex splits at $\beta=20°$, reconnects again at $\beta=40°$, and at $\beta=60°$ splits again. This peculiarity of the tip

vortex splitting is repeatable, as shown in figure 5.9, by the images acquired during two different cycles. Once the tip vortex has split into two separate vortices, the larger and smaller vortices are designated as tip vortex A and tip vortex B, respectively. Returning to figure 5.8, for $\beta=60°$ to $120°$, it appears that tip vortex A contains most of the vorticity that previously had formed the upstream peak of the tip vortex before splitting. Vortex A moves away from the surface as it convects downstream, while B remains along the lower wedge surface.

The surface vortex spans nearly the entire lower surface of the wedge at $\beta=340°$. For $\beta=0°$ to $20°$ the surface vortex continues to grow and appears to pinch and erupt through the tip vortex. At $\beta=40°$, it appears that a section of the surface vortex has been "severed" by the reconnecting tip vortex and is nearly embedded in the lowest section of the tip vortex. For $\beta=60°$ to $120°$ the surface vortex begins to convect downstream along the surface and gradually occupies a larger area. The surface vortex and the tip vortices A and B appear to convect downstream together, while maintaining approximately the same relative distance from one another.

Along the upper wedge surface, for $\beta=60°$ to $120°$, the vorticity levels of the boundary layer are augmented by that portion of the incident vortex adjacent to the boundary. Beginning as early as $\beta=80°$, the intensity of vorticity further increases along the upper surface of the wedge, at a location very near the tip. This continues until, at $\beta=120°$, both a tip vortex and surface vortex have formed on the upper surface.

5.2.2   Evolution of Circulation

The non-dimensional circulation of the vortical structures identified in figure 5.8 for $\beta=340°$ to $120°$ is shown in figure 5.10. It is obvious that the magnitude of the tip vortex is nearly three times larger than the magnitude of the incident vortex. As for the case of the stationary leading-edge (section 4.1.2), the magnitude of the tip vortex rises

77

as the incident vortex approaches, but it splits suddenly at $\beta=20°$. At this cycle angle, the magnitude of tip vortex B is much larger than it is for $\beta=60°$ to $120°$. Also, the sum of the values of circulation of the tip vortices A and B at $\beta=20°$ is substantially larger than the unsplit tip vortex at $\beta=0°$ and $\beta=40°$. These observations suggest that vorticity is still being accumulated within both vortices A and B when it first splits and that a significant amount of in-plane circulation is lost via three-dimensional or viscous effects when the tip vortices A and B recombine. Furthermore, for $\beta=60°$ to $100°$ the sum of the values of circulation for vortices A and B is approximately equal to the circulation of the tip vortex at $\beta=40°$, suggesting that vorticity accumulation in the tip vortex has nearly ended at $\beta=40°$.

The circulation of the surface vortex increases as the circulation of the tip vortex increases, reaching an apparent peak at $\beta=20°$, when the combined circulation of the tip vortex is maximum. For $\beta=40°$ to $60°$, the magnitude of the circulation of the surface vortex actually decreases and then begins to increase to its highest level at $\beta=120°$. It is interesting to note that this circulation increase of the surface vortex occurs when the tip vortex circulation remains nearly constant. The drop in the value of circulation of the tip vortex at $\beta=120°$ may actually be caused by not considering that part of the vortex that has moved beyond the field of view of the image in the circulation calculation.

The time sequence of local circulation upstream and on the lower surface of the leading-edge is shown in figure 5.11 for $\beta=340°$ to $120°$. For $\beta=340°$ to $40°$, the approaching incident vortex can be identified on the left by the negative circulation peak. The two positive circulation peaks correspond to the peaks of vorticity concentration shown in figure 5.8 within the tip vortex. At $\beta=60°$ the first peak of positive circulation decreases almost to zero. This occurs as the incident vortex collides with the tip region and its vorticity, as well as part of the vorticity of the tip vortex, are spread out over a large area. The decrease in the positive peak of the local circulation appears to be due to

78

an additive effect of negative circulation of the incident vortex and positive circulation of the tip vortex. The convection of vortex A can be seen in $\beta=60°$ to $120°$ by the shifting to the right of the remaining positive circulation peak. This peak also seems to maintain a relatively constant level.

5.2.3   Streamline Topology in a Moving Reference Frame

Instantaneous streamline patterns in figure 5.12 are shown in a frame of reference moving at 34.4 mm/s, corresponding to the convection speed of the incident vortex at $\beta=0°$. Length scales smaller than 6 mm, have been filtered out. For the images $\beta=340°$ to $20°$, the incident vortex is visible on the left side of the image; it shows a critical point that changes from a stable focus-unstable limit cycle, to an unstable focus, to concentric circles nested within an unstable limit cycle as it approaches the leading-edge and begins to deform. Saddle points below the incident vortex and above the leading-edge can also be seen. However, at $\beta=40°$, the critical points upstream and above the leading-edge, disappear, perhaps implying that the effect of the incident vortex diminishes.

The tip vortex is readily visible below the leading-edge and generally has the topology of concentric circles within an unstable limit cycle, except at $\beta=340°$ and $\beta=20°$ when the tip vortex also has a stable focus nested within it. At $\beta=20°$, the tip vortex separates into two vortices and then reverts to a single vortex at $\beta=40°$.

5.2.4   Streamline Topology in a Fixed Laboratory Reference Frame

In the series of streamline patterns for $\beta=340°$ to $120°$, shown in figure 5.13, the growing tip vortex on the lower surface is most evident and begins as a stable focus within an unstable limit cycle. For all cycle angles, except $\beta=60°$, the tip vortex has critical point topology that is nested within one or several limit cycles, indicating a transitional state of the tip vortex.

79

For the values of cycle angles shown, the topology of the interior of the tip vortex can be grouped into four stages if the exterior nesting limit cycles are not considered. For $\beta=340°$ to $0°$, the interior topology is a stable focus. At $\beta=20°$ the entire tip vortex splits into two sections with a saddle point between what appears to be an unstable focus very near the tip of the leading-edge, and a larger section with an unstable focus nested within several limit cycles. For $\beta=40°$ to $60°$ the interior critical point is a stable focus, although at $\beta=40°$ the tip vortex has the form of a single entity, and at $\beta=60°$ the vortex splits again. The other critical point that is seen at $\beta=60°$ corresponds to the surface vortex. Finally, for $\beta=80°$ to $120°$, the interior critical point of the tip vortex A is a circle within an unstable focus.

For $\beta=60°$ to $120°$, streamline patterns corresponding to the surface vortex are visible. For $\beta=60°$ to $80°$, the surface vortex appears first as an unstable focus and then changes to a stable focus within an unstable limit cycle. From $\beta=100°$ to $120°$ the streamline patterns do not show a critical point, but they do have substantial curvature just upstream of the tip vortex.

Several other features are evident. The saddle point above the leading-edge at $\beta=340°$ begins to move closer to the tip, until at $\beta=40°$ it is essentially at the tip. The streamlines below the saddle point on the upper surface at $\beta=340°$ to $20°$ are nearly orthogonal to the surface. From $\beta=60°$ to $120°$, the saddle point disappears but a stagnation streamline appears on the lower surface near the tip and moves aft with increasing cycle angle.

For $\beta=80°$ to $120°$, the streamlines appear to pass between the surface vortex and the surface of the wedge, nearly parallel to the surface, and then are entrained within tip vortex A. Comparison of these streamline patterns with images of the velocity field shown in figure 5.14 at the same values of cycle angle supports this conclusion. The higher velocities very close to the lower surface, which are induced by vortex A, suggest

80

that vortex-surface interactions produce additional negative vorticity. This would contribute to the growth of the surface vortex, as observed in figure 5.10.

Finally, the streamline patterns illustrate the formation of a tip vortex on the upper surface beginning at $\beta=100°$. The topology of the tip vortex along the upper surface is an unstable focus. The growth of this vortex appears to occur rapidly.

5.2.5 Concluding Remarks

Although similar in some ways to the flow development for a stationary leading-edge, the development of the tip vortex and the surface vortex for a leading-edge oscillating at $\phi=0°$ is more pronounced, with the circulation of the tip vortex reaching nearly three times that of the incident vortex. The tip and surface vortices on the lower surface are well developed with the surface vortex covering nearly the entire lower surface of the wedge at $\beta=340°$. The streamline patterns in the laboratory frame on the upper surface below the saddle point are nearly orthogonal to the upper surface of the wedge. This suggests that the large amount of vorticity flux into the tip vortex, which develops adjacent to the lower surface, originates on the upper surface from a combination of the pressure gradients, and the component of the acceleration tangent to the upper surface of the wedge during its oscillation.

The tip vortex along the lower surface splits into two distinct vortices A and B at two instants during its development. The instantaneous vorticity distributions and streamline patterns, as well as the values of circulation for tip vortices A and B, differ each time the vortex splits. These observations indicate that vorticity continues to accumulate within the tip vortex when it first splits, but that the vorticity flux ceases prior to the second split. These differences suggest two different mechanisms are involved in the splitting of the tip vortex.

For $\beta=80°$ to $120°$, the circulation of the surface vortex increases steadily to a level

81

that is approximately three-fourths that of the incident vortex. It appears that the generation of additional vorticity from the surface, due to the pressure gradient imposed by tip vortex A, is the origin of the increase of circulation. However, the corresponding circulation plots show a disproportionate rise in surface vortex circulation for a slight decrease in tip vortex A circulation.

Finally, at $\beta=120°$, new tip and surface vortices of opposite sense have developed on the upper surface of the wedge. Tip vortices A and B, as well as the surface vortex, develop in the same fashion as during the first part of the cycle.
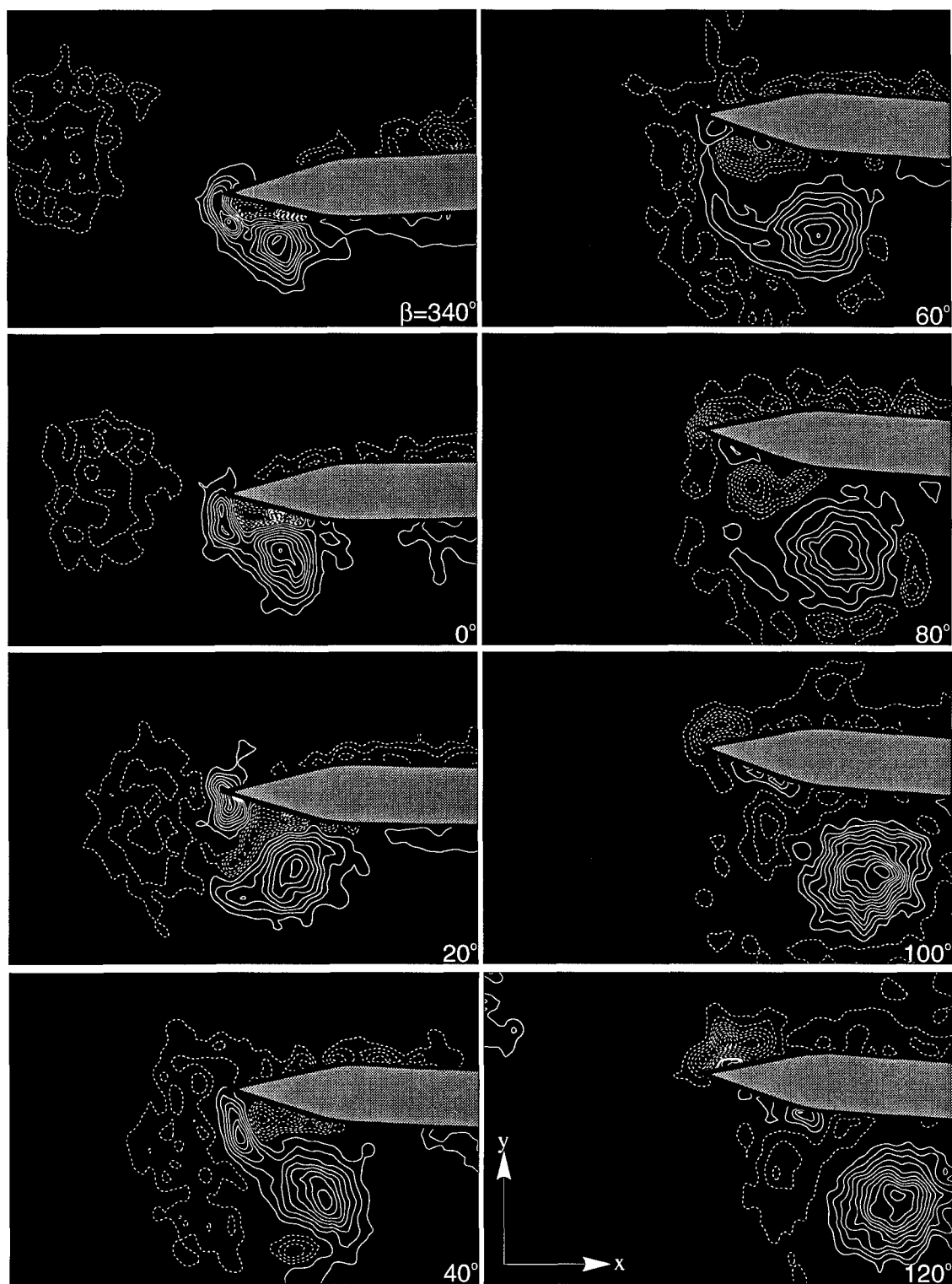
Figure 5.8: Instantaneous vorticity distributions for an oscillating leading-edge at $\phi = 0°$ with respect to an incident clockwise vortex. $|\omega_{min}| = 5\ sec^{-1}$. For $\beta = 340°\text{-}80°$, negative contours, $\Delta\omega = 5\ sec^{-1}$; positive contours, $\Delta\omega = 10\ sec^{-1}$. For $\beta = 100°\text{-}120°$, negative contours, $\Delta\omega = 10\ sec^{-1}$; positive contours, $\Delta\omega = 5\ sec^{-1}$. Re= 6,250.
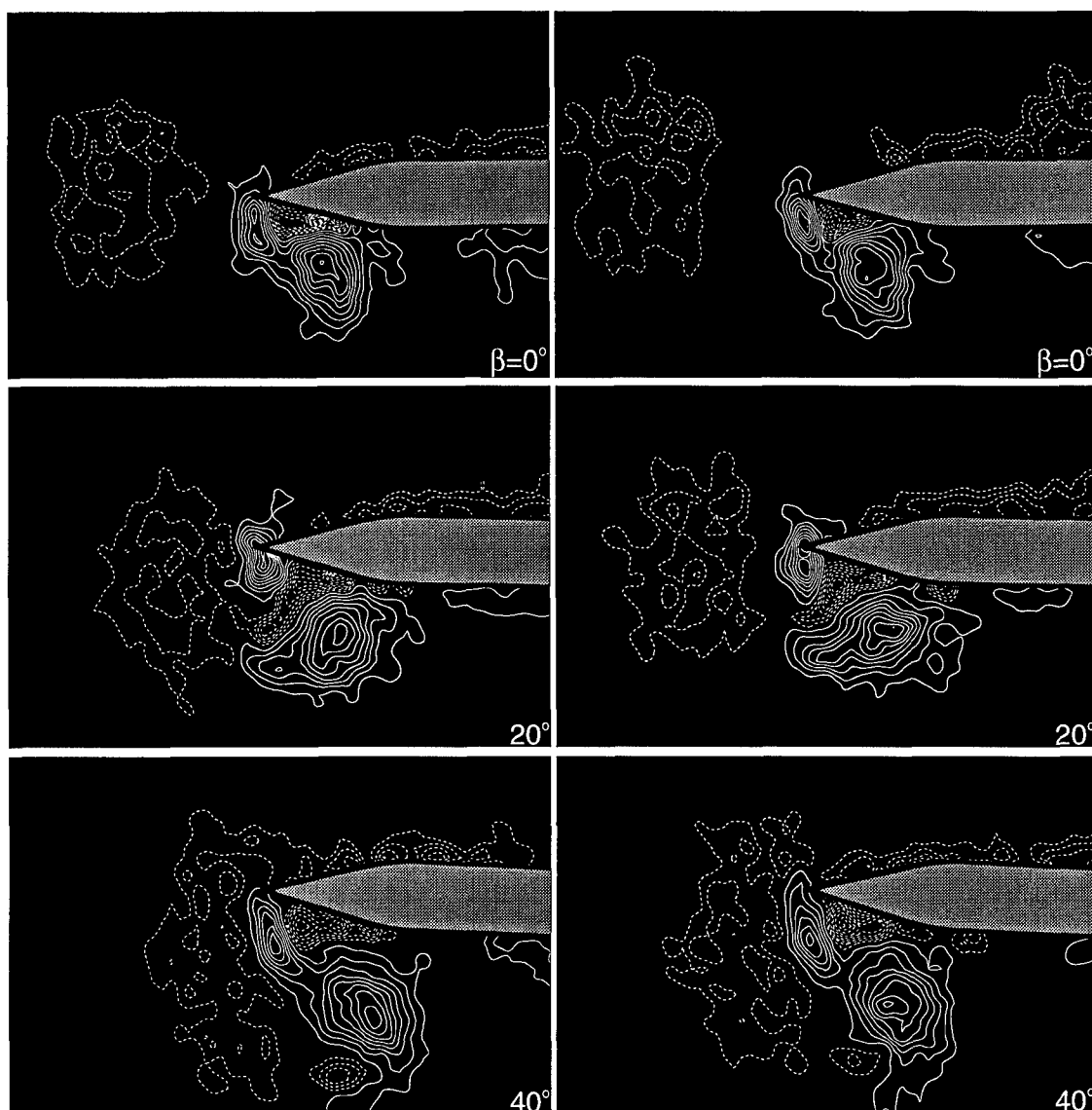
Figure 5.9: Comparison of the instantaneous vorticity distributions from two different cycles for an oscillating leading-edge at $\phi = 0°$ with respect to an incident clockwise vortex. $|\omega_{min}| = 5$ sec^{-1}; negative contours, $\Delta\omega = 5$ sec^{-1}; positive contours, $\Delta\omega = 10$ sec^{-1}. Re= 6,250.
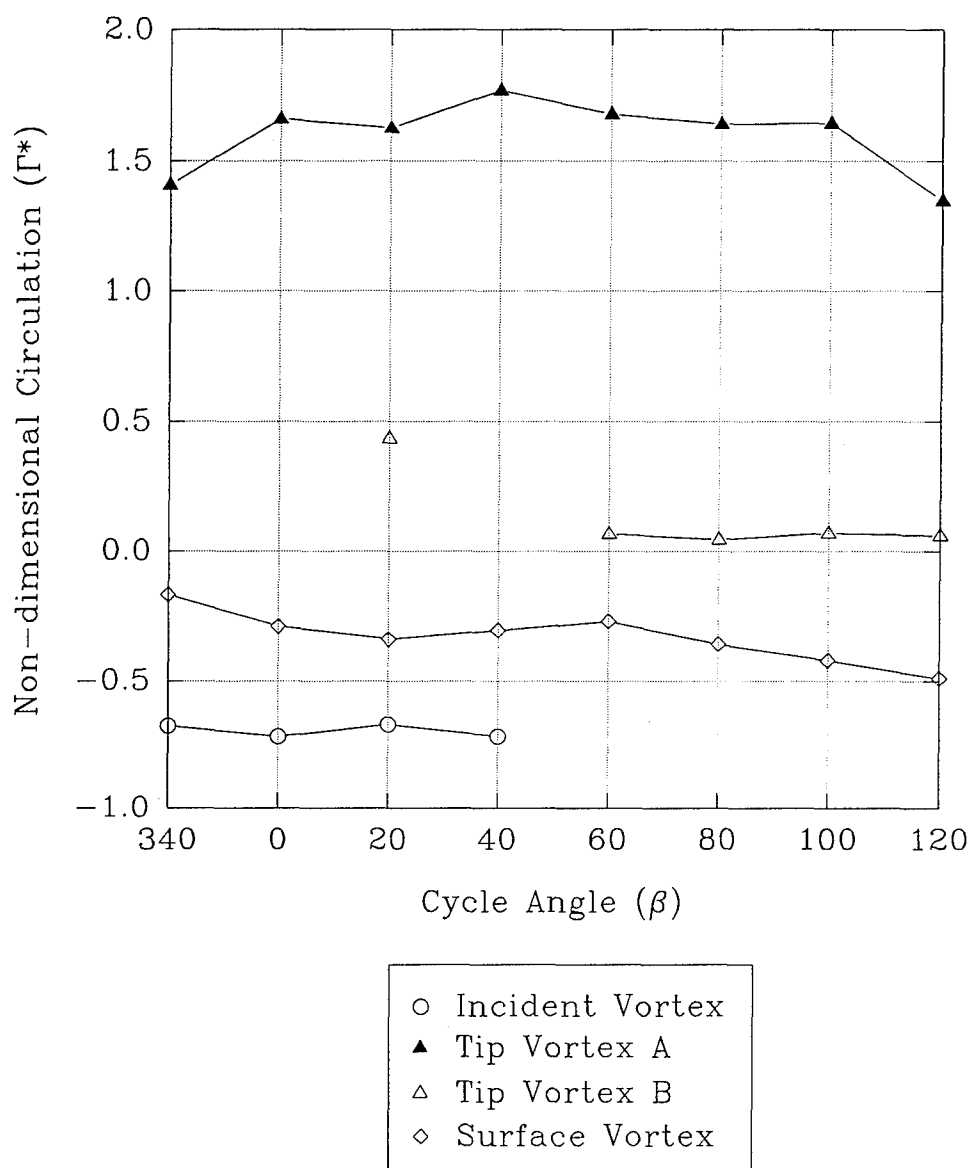
Figure 5.10: Non-dimensional circulation of the incident, tip and surface vortices for a leading-edge oscillating at $\phi=0°$ with respect to the incident vortex.
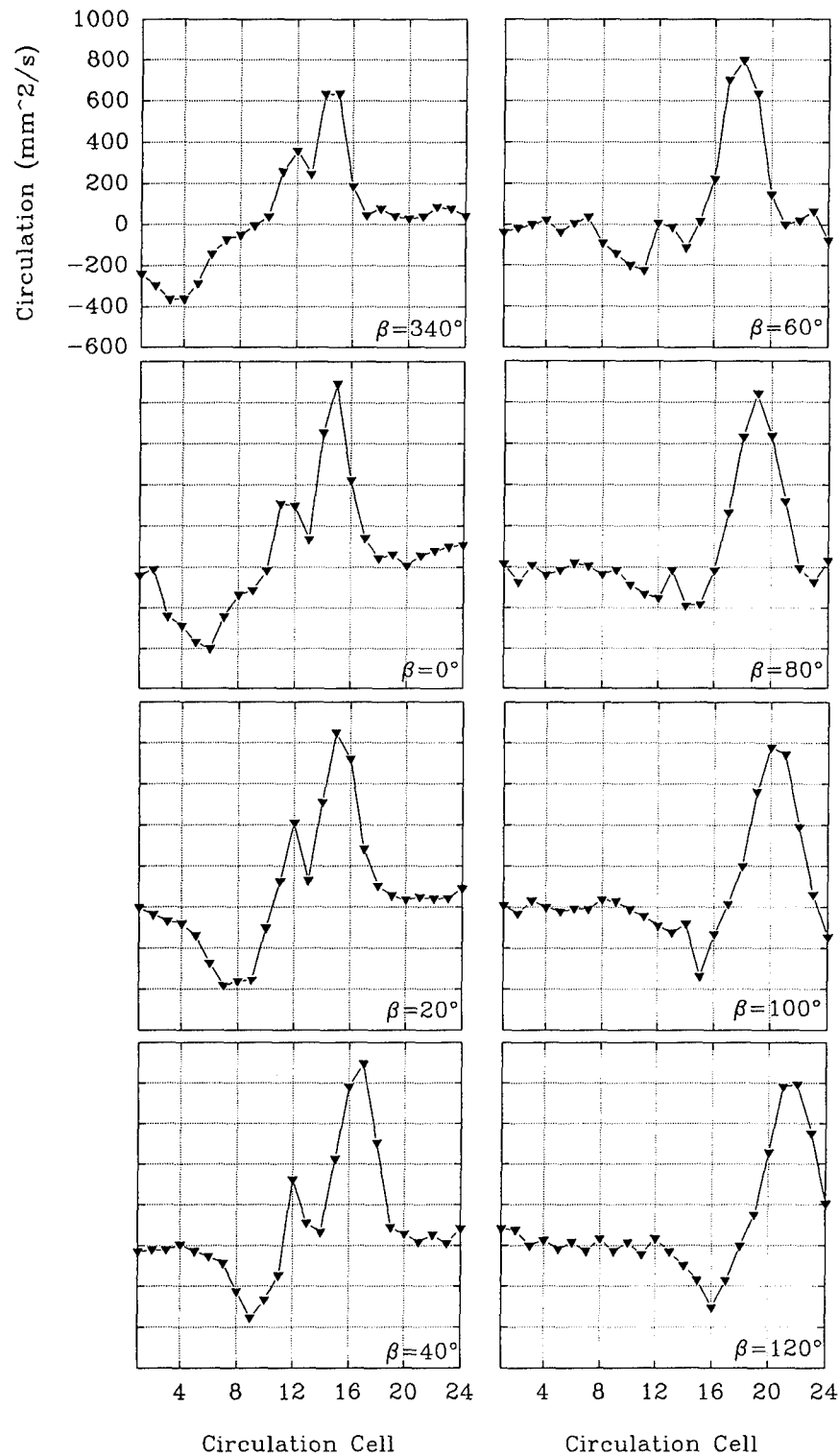
Figure 5.11: Temporal evolution of the local circulation upstream of and along the lower surface of a leading-edge oscillating at a phase angle $\phi=0°$ with respect to an incident vortex
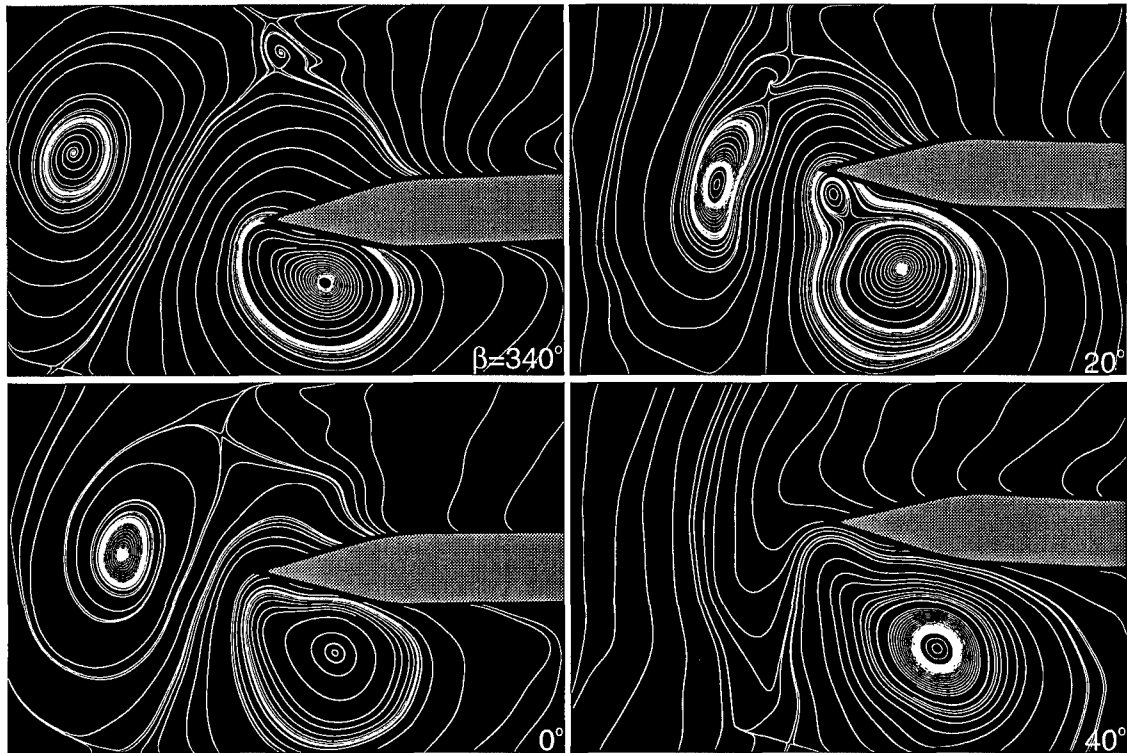
Figure 5.12: Streamline patterns in a moving reference frame for an oscillating leading-edge at $\phi = 0°$ with respect to an incident clockwise vortex. Re= 6,250
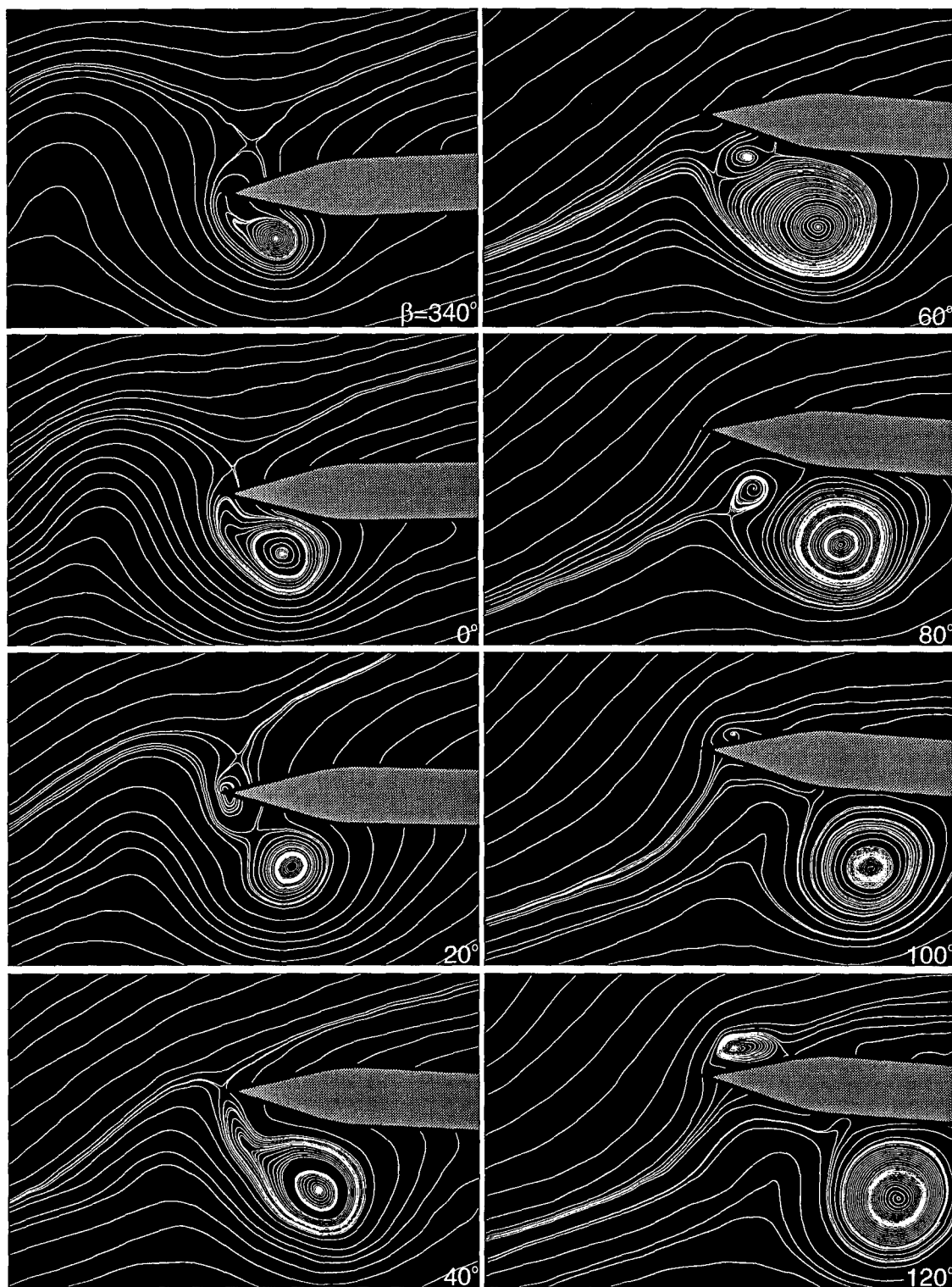
Figure 5.13: Streamline patterns in the laboratory reference frame for an oscillating leading-edge at $\phi = 0°$ with respect to an incident clockwise vortex. Re= 6,250.
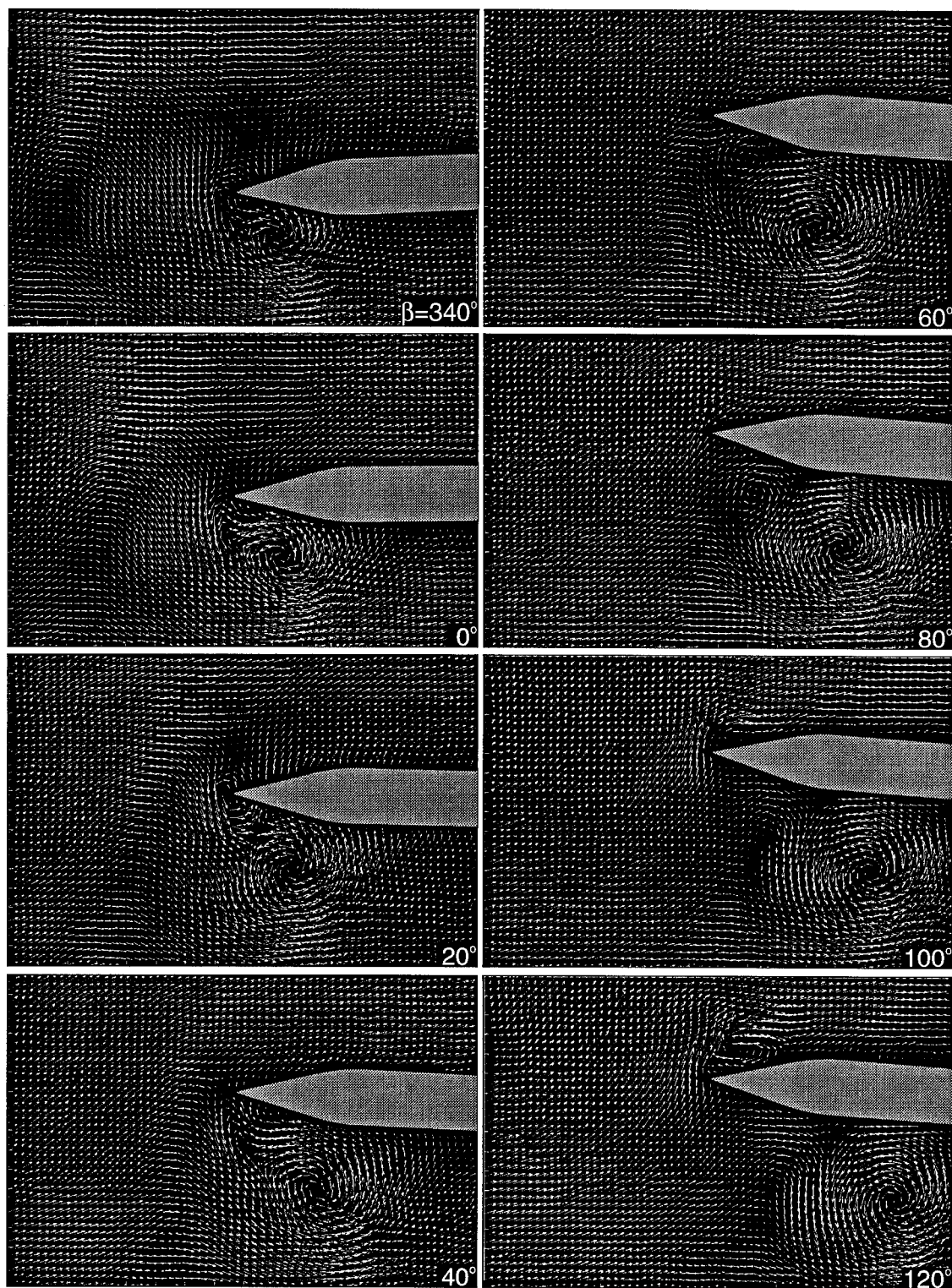
Figure 5.14: Instantaneous velocity field of an oscillating leading-edge at $\phi =0°$ with respect to an incident clockwise vortex. Re= 6,250.

5.3 Vortex Interaction with an Oscillating Leading-Edge at $\phi=180°$

5.3.1 Instantaneous Vorticity Distributions

Figure 5.15 shows the instantaneous vorticity distributions for a leading-edge that is oscillating at a phase angle $\phi=180°$ with respect to an incident clockwise vortex. Consequently at $\beta=180°$, the instant that the center of the incident vortex is within one diameter of the leading-edge, the leading-edge is at $\alpha=0°$ during its downstroke. (Refer to section 2.2 for a detailed definition of phase angle β.)

In figure 5.15, the incident vortex of negative vorticity (dashed lines) is visible throughout the entire range of cycle angle β. It approaches the oscillating leading-edge for $\beta=160°$ to 200°, and then passes along the upper surface for $\beta=220°$ to 300°. For $\beta=160°$ to 200°, the incident vortex convects slightly above, rather than along the plane of symmetry of the edge, as for the case of a stationary leading-edge (see Chapter 4). This difference in transverse offset of the incident vortex as it approaches the edge is attributed solely to the effect of the oscillation of the leading-edge at $\phi=180°$. The induced velocity at the tip of the oscillating leading-edge at $\beta=180°$ will be in the positive y-direction due to the edge motion. This induced velocity appears sufficient to displace the incident vortex upwards when it is close enough to the tip.

Interestingly, there is little indication of development of a tip vortex and no development of a surface vortex throughout the cycle angles shown in figure 5.15. At $\beta=200°$, 240°, and 300°, significant levels of positive vorticity are generated near the tip and it appears that a tip vortex begins its early formation. However for $\beta=200°$ and 240°, the next cycle angle shows tip vortex growth to be retarded or even reversed such that no vortex is formed. Although $\beta=320°$ is not shown in figure 5.15, the same result occurs in that no tip vortex forms as the counterclockwise incident vortex approaches.

For $\beta=160°$ to 180° the vorticity distribution on the upper and lower surfaces of the

90

leading-edge appear remarkably symmetric, being similar to a very thick boundary layer. The location of the stagnation line, inferred from the vorticity distributions, appears to be at the tip of the leading-edge on the upper surface, opposite to where it would be in the absence of the incident vortex. This indicates the influence of the incident vortex is greater than that due to the leading-edge oscillation in absence of the incident vortex. For the remainder of the cycle angles, the incident vortex is directly above the upper surface and the upper surface vorticity distribution varies dramatically to the point where no negative vorticity is visible at $\beta=300°$. In addition, at $\beta=240°$, contours of positive vorticity cover over half of the upper wedge surface and suggests the stagnation line moves very far aft under the influence of the incident vortex.

5.3.2   Evolution of Circulation

Since no tip or surface vortices were formed during the interaction of the incident clockwise vortex with the edge, the non-dimensional circulation of the incident vortex plotted in figure 5.16 is compared to the circulation of the visible vorticity that is distributed over the upper and lower surfaces of the leading-edge. The non-dimensional circulation of the incident vortex seems to fluctuate slightly about $\Gamma^* = -0.7$ for $\beta=160°$ to 260°, then drops quickly to a level close to $\Gamma^* = -0.5$ for $\beta=280°$ to 300°. The circulation along the lower and upper surface begins at nearly the same magnitude at $\beta=160°$, but then begins to drop. The circulation vanishes for the upper surface when no vorticity is visible on the upper surface in figure 5.15 and occurs for $\beta=280°$ to 300°. The circulation along the lower surface decreases until $\beta=260°$, after which it begins to rise again, coinciding with the change in the direction of leading-edge oscillation.

Because of the more significant variations in local circulation that are caused when the incident vortex convects above the upper surface, the temporal evolution of the local circulation upstream of and along the upper surface, rather than the lower surface, is

91

shown in figure 5.17. The convection of the incident vortex is evident as the negative peak of the circulation moves along the surface. In addition, the circulation of the incident vortex appears to become more widely distributed over the area of the incident vortex, rather than rising to a single peak.

5.3.3   Streamline Topology in a Moving Reference Frame

Instantaneous streamline patterns obtained by moving the frame of reference at 37.1 mm/s, the convection speed of the incident vortex at $\beta=180°$, and by filtering out length scales smaller than 6 mm, are shown in figure 5.18. The incident vortex can be identified in all images, as it convects downstream and begins to move along the upper surface, usually appearing as an unstable focus. At $\beta=200°$ the incident vortex topology changes to a stable focus nested within an unstable limit cycle and then at $\beta=220°$ reverts to an unstable focus nested within two limit cycles. The switch to a stable focus suggests a stretching along the axis of the vortex which may be due to the apparent deformation of the vortex at $\beta=200°$ as it impinges the edge and moves toward the upper surface. The smaller scale, ill-defined topology located downstream of the incident vortex and above the upper surface of the edge at $\beta=200°$, does not appear to represent any physically reasonable structure shown in the vorticity distribution. Since streamline topology is reference frame dependent and knowing that the convection speed of the incident vortex varies significantly in this case (see figure 5.21), this smaller-scale topology is most likely caused by small fluctuations in the velocity field viewed in the reference frame, and is not significant.

5.3.4   Streamline Topology in the Laboratory Reference Frame

The streamline topology in a fixed reference frame, shown in figure 5.19, does not show any critical points until $\beta=240°$, when an unstable focus is the dominant structure

along the upper wedge surface. Streamlines that emanate from the unstable focus curve in the upstream direction along the upper surface before sweeping across the tip. In addition, a combination saddle point and unstable node are located adjacent to the upper surface. The stagnation point appears to be immediately below the unstable node. At $\beta=260°$, the unstable node disappears and the saddle point has moved to the surface, becoming a half-saddle point and indicating the location of the stagnation point. The unstable focus changes to a stable focus, with a stable node-saddle point pair appearing just below. For $\beta=280°$ to $300°$, nearly all critical points vanish. Only a half-saddle point appears on the upper wedge surface and moves to the tip.

For $\beta=160°$ to $180°$ there is no distinct and clearly discernible stagnation line. Referring to the corresponding velocity fields in figure 5.20, it appears that the stagnation point is at the tip and that the velocity at the tip induced by the motion of the leading-edge nearly cancels the orthogonal velocity component induced by the incident vortex. Referring again to figure 5.19, as the vortex impinges upon the edge, it appears that the velocity induced at the tip overcomes the effects of tip motion and a clear stagnation line is visible on the upper wedge surface at $\beta=200°$. At $\beta=220°$, several streamlines on the upper wedge surface appear almost like stagnation lines, in that there is very little curvature near the surface. This indicates perhaps that along the upper surface of the wedge, the velocity of the flow is of the same order as the induced velocity of the surface during its downward motion. An analogous situation arises for $\beta=300°$.

5.3.5   Concluding Remarks

When an incident clockwise vortex interacts with a leading-edge that is oscillating at $\phi=180°$, the flow field near the leading-edge appears to depend on whether the influence of the leading-edge oscillation or the influence of the incident vortex dominates. At certain cycle angles the observed flow field exhibits characteristics that suggest the two

93

influences are balanced. Consequently, a persistent tip vortex is never formed for $\beta=160°$ to $300°$.

The influence of the incident vortex appears to dominate at $\beta=240°$. Figure 5.21 shows the incident vortex convection speed is slowest, with a maximum value of azimuthal velocity (V_θ) at $\beta=240°$ (refer to section 3.2 for a definition of V_θ). In a potential flow field, the convection speed of a clockwise rotating two-dimensional vortex in a freestream will decrease due to the induced field of its image below the surface. Therefore, at $\beta=240°$, the incident vortex lingers longer over the surface, affording a greater influence over the flow field along the upper surface and generating positive vorticity over much of the upper surface of the wedge, as seen in figure 5.15. The slower convection speed could also explain the appearance of the unstable focus in the laboratory frame for $\beta=240°$ to $260°$.

Similarly, the effects of leading-edge oscillation dominate over the influence of the incident vortex near the tip at $\beta=280°$ to $300°$. This is manifested by the accumulation of positive vorticity along the lower surface, which would occur in the absence of the incident vortex when the leading-edge begins to pitch upward. In another example, at $\beta=160°$ to $180°$, the induced velocity at the tip due to the oscillation of the edge displaces the incident vortex upward as it approaches the edge.

At certain cycle angles, the velocities induced by the incident vortex and the edge oscillation are balanced sufficiently to produce a distinct flow field. For $\beta=160°$ to $180°$, nearly symmetrical distributions of vorticity along the upper and lower surfaces are generated without the usual tip vortices produced by the edge oscillation or vortex impingement alone. Furthermore, the stagnation line appears to be very close to the tip. This suggests that the velocity at the tip, induced by the edge oscillation, nearly cancels the velocity induced at the tip by the incident vortex. The resulting velocity field is void of critical points. At $\beta=200°$, this balance is offset slightly on the upper surface of the

94

wedge when the influence of the incident vortex is sufficient to reveal a stagnation streamline in the laboratory frame. At $\beta=220°$, another type of balance on the upper wedge surface occurs when the induced velocity of the incident vortex nearly matches the velocity of the edge in its downward motion. Finally, when the upper surface vorticity disappears for $\beta=280°$ to $300°$, it does so because the effect of the oscillation neutralizes the influence of the incident vortex along the upper surface and causes a decrease in its circulation. In all of these cases, this balance seems to occur in a local region and not necessarily over the entire leading-edge.
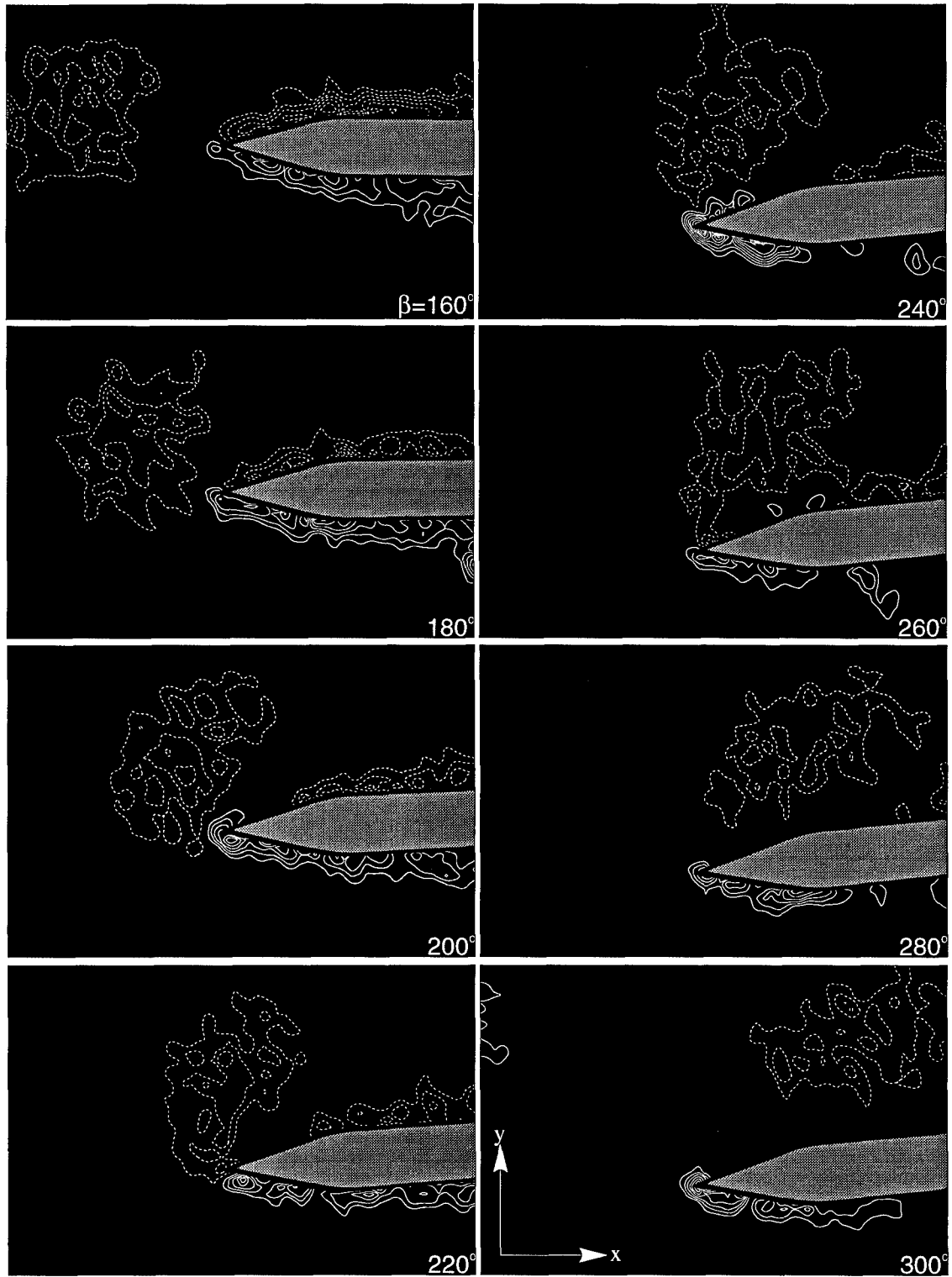
Figure 5.15: Instantaneous vorticity distributions for an oscillating leading-edge at $\phi = 180°$ with respect to an incident clockwise vortex. $|\omega_{min}| = 5$ sec^{-1}; $\Delta\omega = 5$ sec^{-1}. Re= 6,250.

96
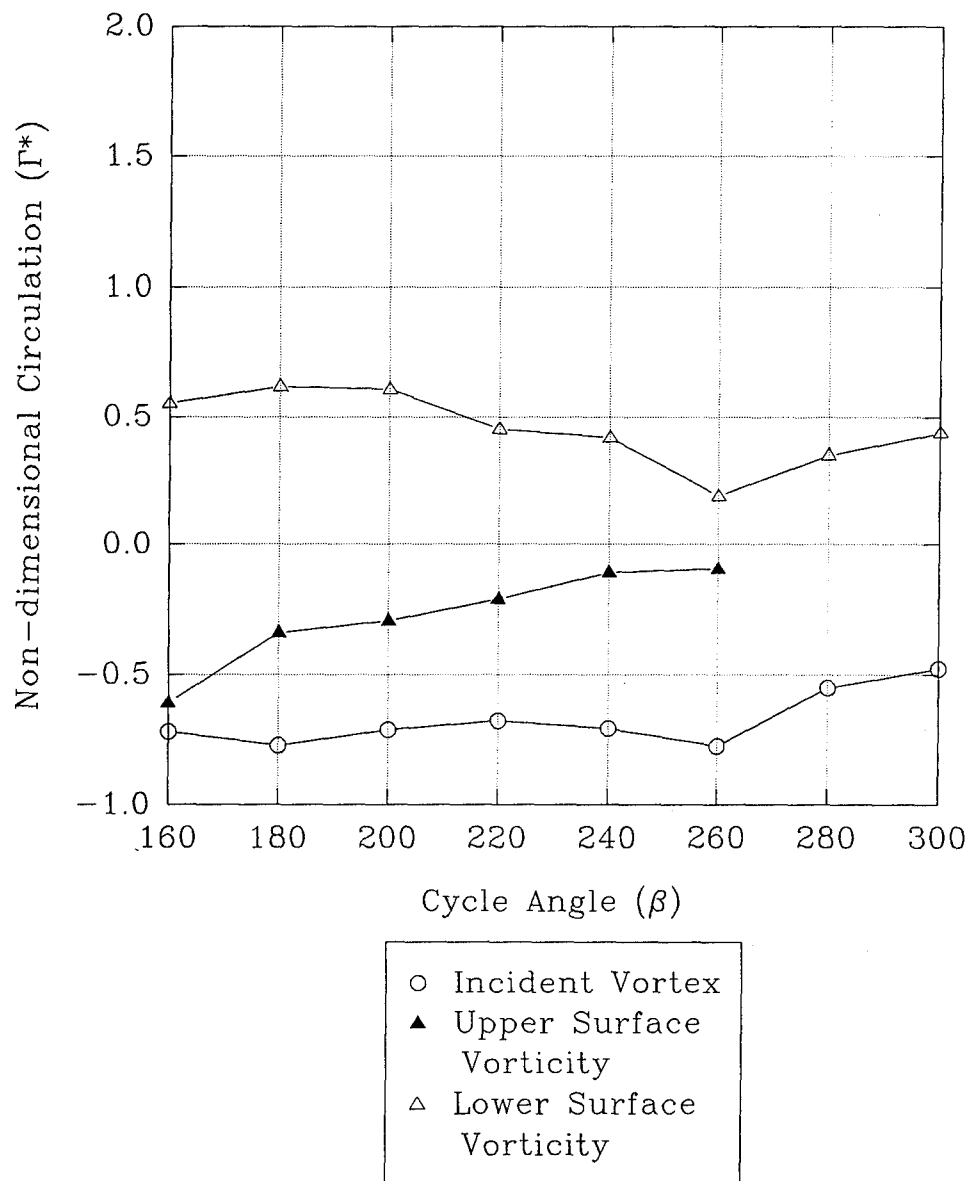
Figure 5.16: Non-dimensional circulation of an incident vortex and the visible surface vorticity on an oscillating-leading-edge at $\phi=180°$

97
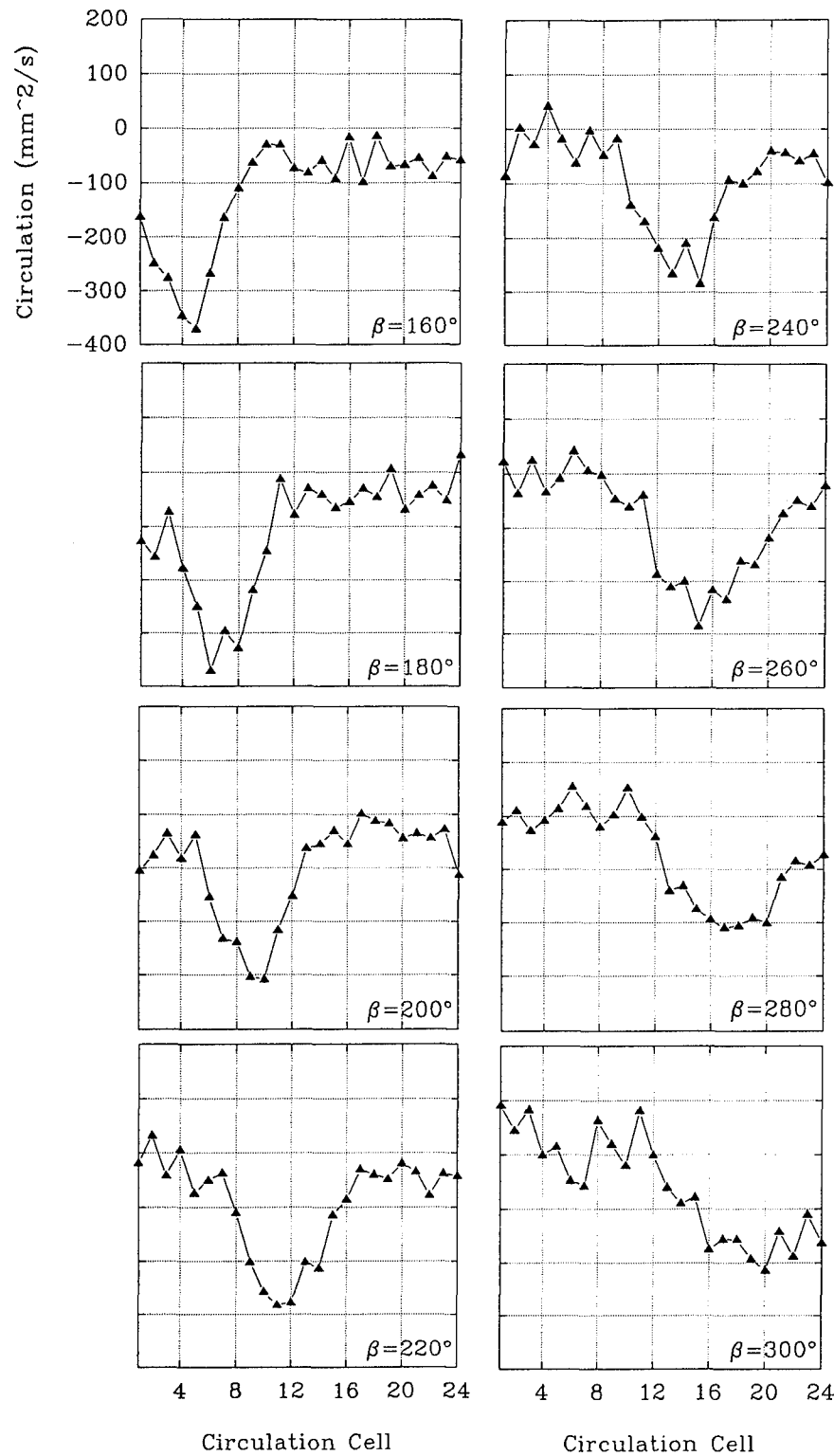
Figure 5.17: Temporal evolution of the local circulation upstream of and along the upper surface of an oscillating leading-edge at $\phi=180°$ with respect to an incident vortex
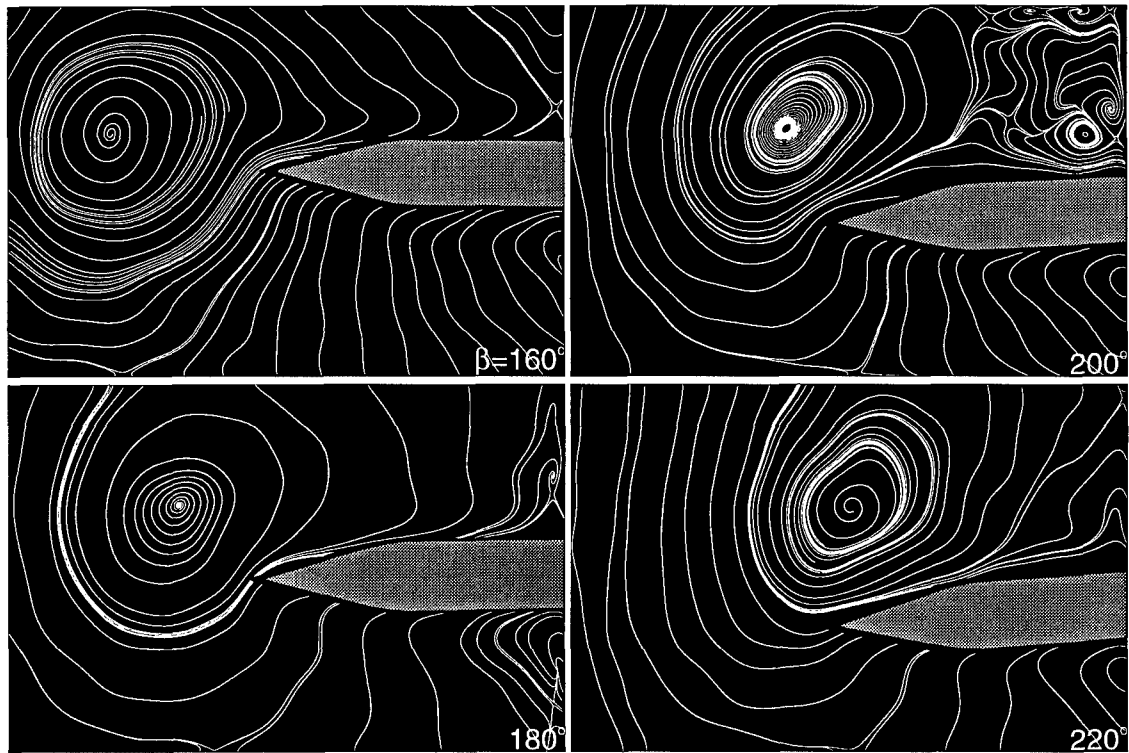
Figure 5.18: Streamline patterns in a moving reference frame for an oscillating leading-edge at $\phi = 180°$ with respect to an incident clockwise vortex. Re= 6,250.
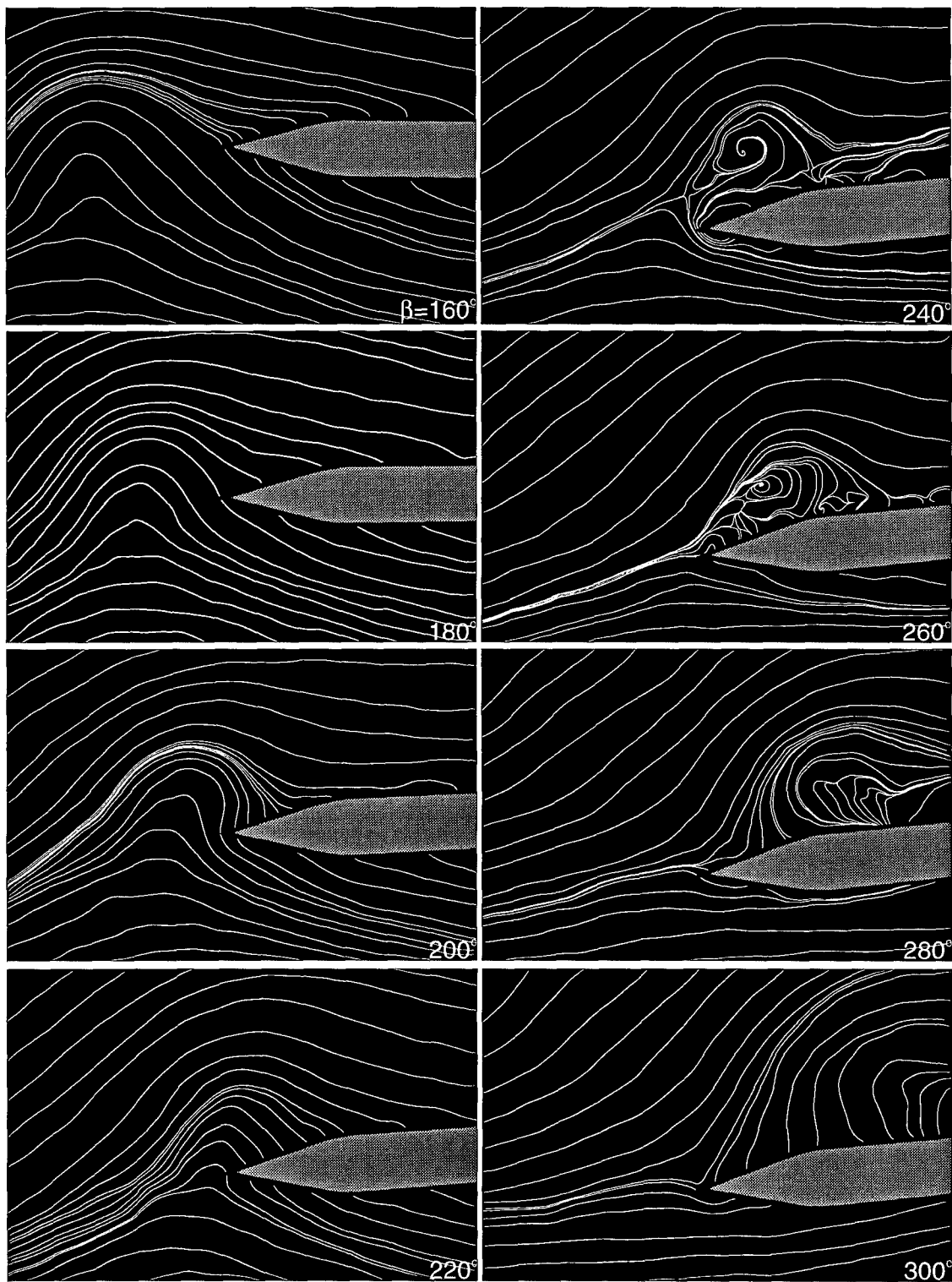
Figure 5.19: Streamline patterns in the laboratory reference frame for an oscillating leading-edge at $\phi = 180^\circ$ with respect to an incident clockwise vortex. Re= 6,250.
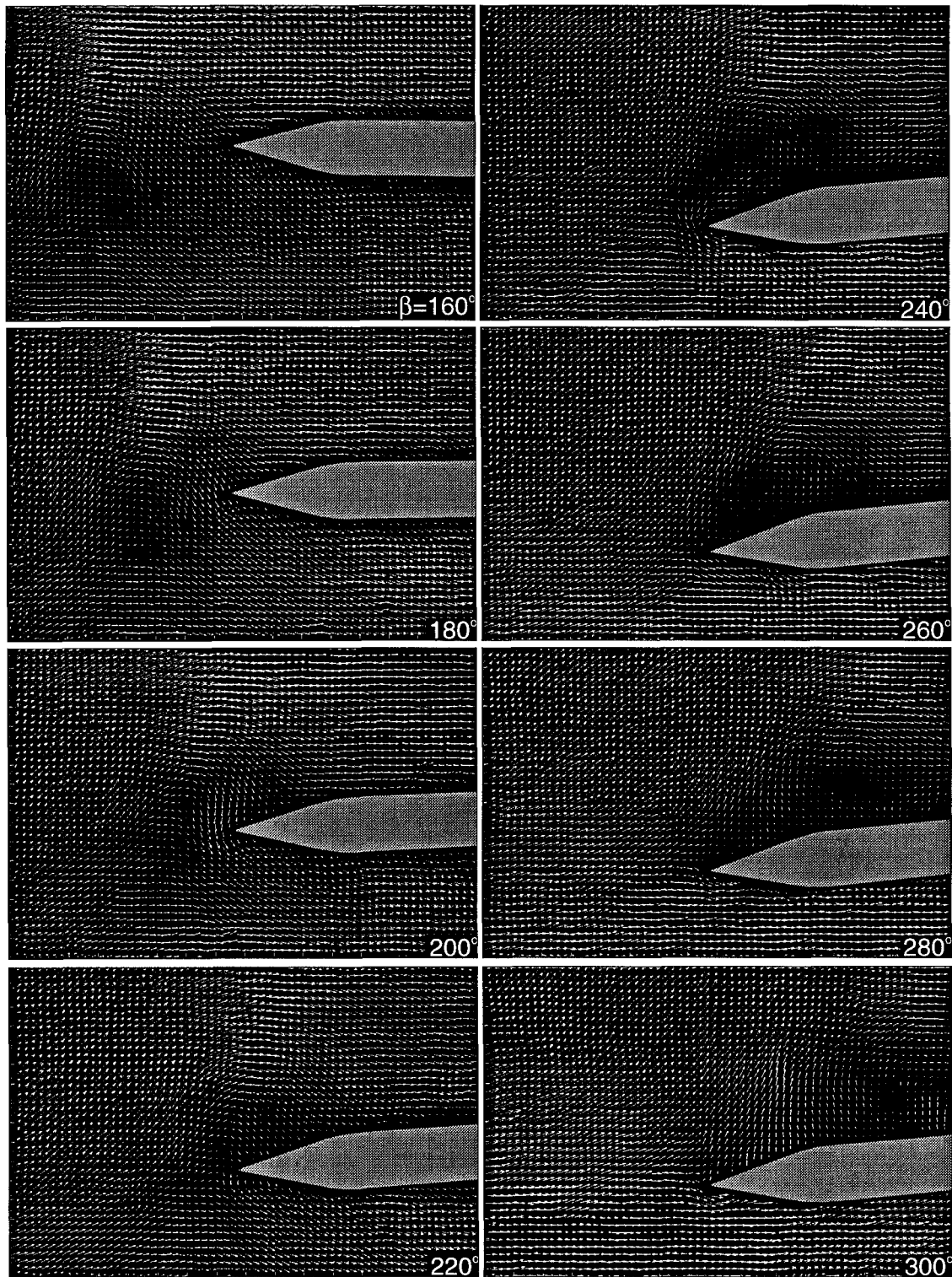
Figure 5.20: Instantaneous velocity field of an oscillating leading-edge at $\phi = 180°$ with respect to an incident clockwise vortex. Re= 6,250.
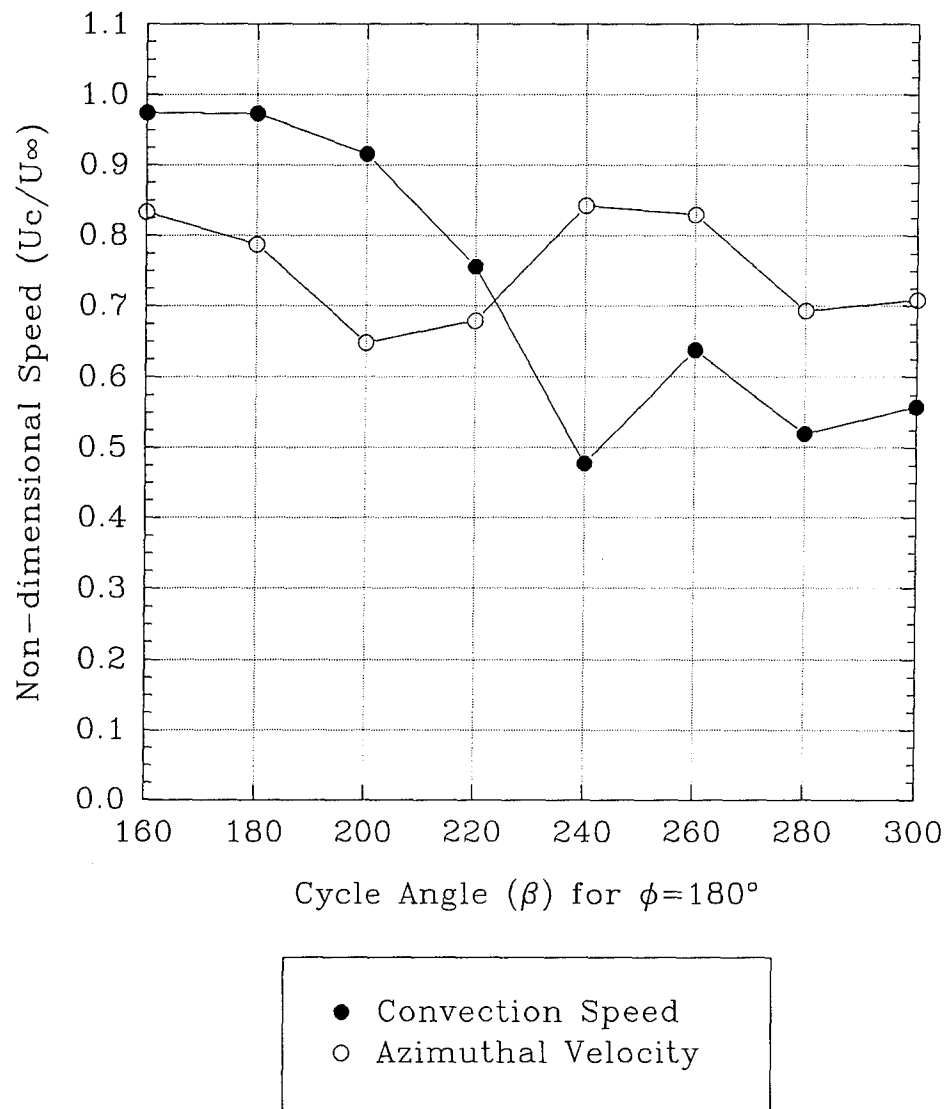
Figure 5.21: Non-dimensional convection speed and azimuthal velocity of an incident clockwise vortex interacting with an oscillating leading-edge at $\phi=180°$

102

5.4 Effect of Reynolds Number on Interaction

5.4.1   Vortex Interactions with an Oscillating Leading-Edge at $\phi=0°$

Instantaneous vorticity distributions and streamline patterns in the laboratory and moving reference frames, at Reynolds numbers of 6,250 (left column) and 25,000 (right column), are compared in figure 5.22 for a single value of cycle angle $\beta=0°$. At each Reynolds number, the leading-edge is oscillating at a reduced frequency $k=5$ and amplitude $A=5°$.

In the top row of figure 5.22, the vorticity distributions for both Reynolds number (Re) cases are similar. The center of the incident vortex is at the same relative position upstream of the leading-edge. The incident vortex for the higher Re case appears smaller but at a much higher level of minimum vorticity. Tip and surface vortices have also formed along the lower wedge surface. However, the tip vortex for the higher Re case has split with the lower portion of the tip vortex containing two prominent peaks of positive vorticity. The surface vortex in this case appears to have severed the tip vortex.

The streamline patterns in the laboratory reference frame are shown in the middle row. Both cases show the saddle point above the upper surface with the saddle point in the higher Re case being slightly further aft. The lower Re case depicts the tip vortex as a stable focus nested within concentric circles and two limit cycles. The higher Re case shows the tip vortex has split into an unstable focus nested within a stable limit cycle below, and a stable focus near the tip.

Streamline patterns in a reference frame moving with the incident vortex are shown in the bottom row. Very similar critical points are observed in both Re cases. The core of the incident vortex in the higher Re case is shown as concentric circles, suggesting two-dimensional flow. A stable focus is shown in the core of the incident vortex for the lower Re case.

103

5.4.2   Vortex Interactions with an Oscillating Leading-Edge at $\phi=180°$

Reynolds number comparisons of the vorticity distributions and streamline patterns at $\beta=180°$ for a leading-edge oscillating at $\phi=180°$ with respect to an incident clockwise vortex are shown in figure 5.23. The vorticity distributions in the upper row of figure 5.23 show that the incident vortex has already collided with, and begun to deform around, the leading-edge in the higher Re case. However, both cases show essentially symmetrical distributions of vorticity along the upper and lower surfaces of the leading edge. Streamline patterns are nearly identical in both reference frames with the topology of the incident vortex depicted as an unstable focus in the moving frame for both cases.

5.4.3   Concluding Remarks

For a sharp oscillating leading-edge, the general flow development and structure appear nearly independent of Reynolds number. The most significant effect of Re is to alter the development of the vortex formed from the lower surface. A higher value of Re appears to advance the growth of the surface vortex which may cause early splitting of the tip vortex.
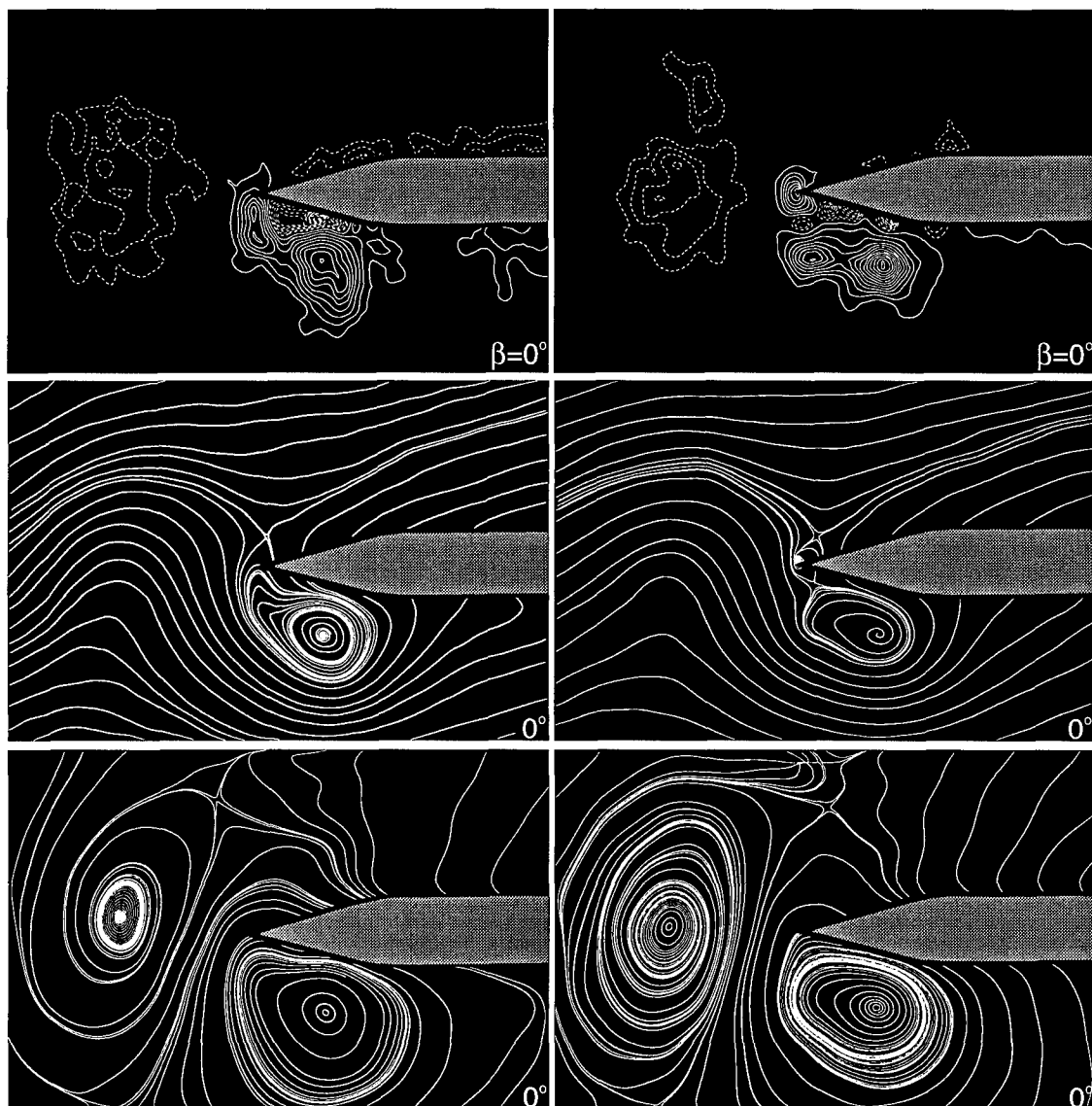
Figure 5.22: Reynolds number comparison of an oscillating leading-edge at $\phi = 0°$ with respect to an incident clockwise vortex. The left column shows Re= 6,250, with $|\omega_{min}| = 5$ sec^{-1}, negative contour $\Delta\omega = 5$ sec^{-1}, and positive contour $\Delta\omega = 10$ sec^{-1}. The right column shows Re = 25,000 with $|\omega_{min}| = 20$ sec^{-1}, negative contour $\Delta\omega = 20$ sec^{-1}, and positive contour $\Delta\omega = 40$ sec^{-1}.
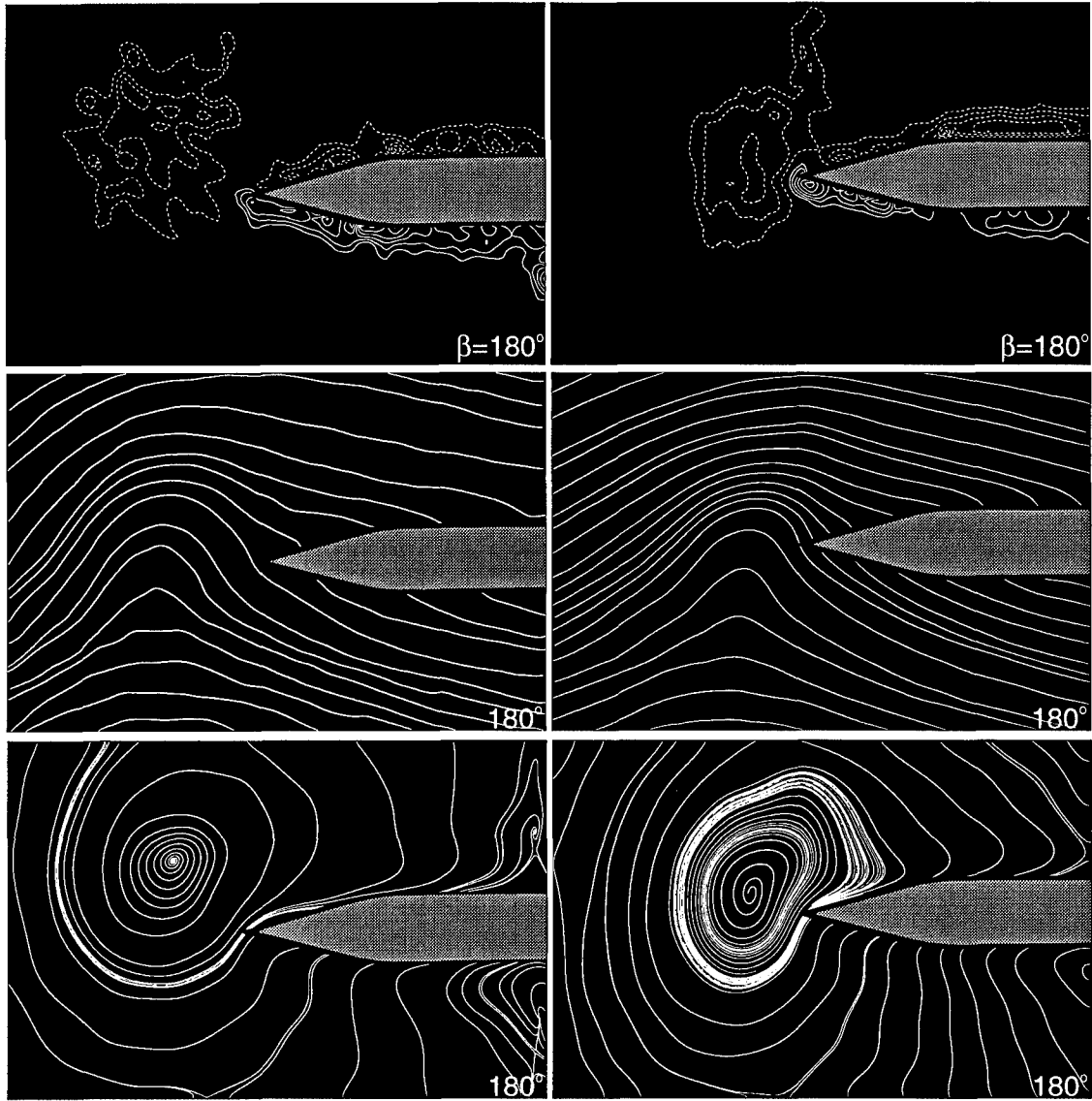
Figure 5.23: Reynolds number comparison of an oscillating leading-edge at $\phi = 180°$ with respect to an incident clockwise vortex. The left column shows Re= 6,250 with $|\omega_{min}| = 5$ sec^{-1} and contour interval $\Delta\omega = 5$ sec^{-1}. The right column shows Re = 25,000 with $|\omega_{min}| = 20$ sec^{-1} and contour interval $\Delta\omega = 20$ sec^{-1}.

6.0 COMPARISON OF VORTEX INTERACTIONS WITH A STATIONARY AND OSCILLATING LEADING-EDGE

In chapters four and five, experimental results obtained by high density particle image velocimetry were presented for each case of vortex interactions. In this chapter, direct comparisons of the results are made in an effort to better understand the mechanisms which cause both similar and distinct flow structure in the cases presented. Vortex interactions with a stationary leading-edge are compared first in 6.1 with those of an oscillating leading-edge without an incident vortex. The superposition of the results of these two cases is then compared in section 6.2 to the results obtained for the leading-edge oscillating at $\phi=0°$ and $\phi=180°$ with respect to the incident vortex. Next, the effect of phase angle on the interactions with an oscillating leading-edge is assessed in section 6.3. Finally, in section 6.4 the stages of tip vortex development are identified.

6.1 Stationary Versus an Oscillating Leading-Edge without an Incident Vortex

6.1.1 Non-Stationary Airfoil Theory

Assuming the incompressible flow about an arbitrary airfoil is two-dimensional and that the airfoil thickness and amplitude of oscillation are small compared to the chord (where the resulting disturbance velocity $\tilde{v}$ is such that $\tilde{v}/U_\infty \ll 1$), Sears (1941) applies aspects of non-stationary airfoil theory to show the lift and moment on a sinusoidally oscillating airfoil varies with the reduced frequency

$$k = \frac{\omega C}{2U_\infty}$$

(1),

where C is the airfoil chord and ω is the frequency of oscillation in rad/sec. The lift and moment of a stationary airfoil subjected to a sinusoidal gust was also shown by Sears to vary with the reduced frequency of the convecting gust such that

$$k_g = \frac{\pi C}{\lambda}\left(\frac{U_c}{U_\infty}\right)$$

<div align="right">(2),</div>

where U_c is the convection speed and λ the wavelength of the sinusoidal gust. Furthermore, Kemp (1952) shows the lift of a stationary airfoil subjected to a sinusoidal gust must be proportional to the circulation of a sinusoidally oscillating airfoil, which also varies with reduced frequency.

If flow is considered two-dimensional and incompressible, and the airfoil thickness and amplitudes of motion are small, Sears (1941) shows that the more complex case of an airfoil oscillating while subjected simultaneously to a sinusoidal gust, may be considered as the superposition of the two independent cases. For example, the calculated moment of the oscillating airfoil in a freestream may be added to the calculated moment of the stationary airfoil subjected to a sinusoidal gust to obtain the total moment of an airfoil subjected to both motions. This concept of superposition serves as a framework for evaluating the extent to which the observations of the present study are linearly additive or highly nonlinear.

6.1.2   Flow Structure Comparison

In this investigation, as seen from the streamline patterns in the laboratory reference frame for a stationary leading-edge, the incident vortex street produces a sinusoidal gust with a reduced frequency $k_g=5$. Even though the flow is not entirely two-dimensional and the amplitudes of oscillation may be too large to strictly apply non-stationary airfoil theory, it should be useful to compare the results of a vortex impinging a stationary leading-edge to those of the sinusoidally oscillating leading-edge without an incident vortex.

Figure 6.1 and 6.2 compare the instantaneous streamline patterns and vorticity distributions at representative cycle angles for a vortex street impinging upon a

stationary leading-edge (left column) with those of an oscillating leading-edge in a freestream (right column). Referring first to figure 6.1, the topology at $\beta=0°$ for the two cases is similar with a half-saddle point on the upper surface near the tip. On the lower surface both images depict tip vortex formation with the left image showing a stable limit cycle, and the right, an unstable node, saddle point and unstable focus. At $\beta=100°$, the flow structure is even more similar with corresponding stable limit cycles. For $\beta=180°$ and 280°, the topologies differ with the images for the oscillating leading-edge showing well-developed tip vortices on the upper surface and those of the stationary edge showing no tip vortex development.

Similar trends are observed in figure 6.2. At $\beta=0°$ and 100°, the tip vortex development and along the lower surface is nearly identical. The vorticity from the incident vortex can be seen on the left side of the image, at $\beta=100°$ along the upper surface, below the tip vortex; it constitutes the only difference between the two cases. However, for $\beta=180°$ and 280°, the incident vortex is entirely above the centerline of the leading-edge and appears to induce a substantially different flow field along the upper surface.

6.1.3   Average Tip Velocity

The velocity component orthogonal to the line of symmetry of the leading-edge was averaged along a 4 mm segment upstream of the tip for the stationary and the oscillating leading-edge. Distributions of this averaged velocity are shown in figure 6.3. In addition, the induced velocities shown in figure 3.4 are also plotted in figure 6.3 for reference.

In general, the average orthogonal velocity for both the stationary and oscillating edge case appear to vary sinusoidally with cycle angle. In both cases, the velocities are positive from $\beta=60°$ to 220°. The largest differences between the stationary and

oscillating edges occur at $\beta=320°$ to 40° and $\beta=180°$ to 200°, when an incident vortex approaches the stationary leading-edge.

Peaks of averaged velocity for the stationary edge occur at $\beta=160°$ and 340° with magnitudes that are approximately symmetrical about the zero line, but exceed the calculated induced velocity. After reaching the peak at $\beta=340°$, the average orthogonal velocity in the stationary case levels off until $\beta=40°$. Such a leveling indicates that a higher magnitude could exist between the cycle angles shown.

Based on the nearly symmetrical development of the vorticity field shown in chapter 5, it is quite unexpected that the magnitude of the average orthogonal velocity for the oscillating edge is not symmetrical about the zero line but is larger when positive, peaking at $\beta=140°$. The negative peak occurs at $\beta=300°$. Moreover, this averaged velocity shows several large excursions from the induced velocity curve resulting from the motion of the edge alone. Interestingly, at $\beta=0°$ and 180°, the average velocity is close to the value of the curve.

6.1.4   Concluding Remarks

The average velocity orthogonal to the line of symmetry of the leading-edge for both the stationary and oscillating leading-edge cases varies sinusoidally, with a change in direction occurring at $\beta=60°$ and 240°. This direction change corresponds in both cases to the movement of the stagnation line or saddle point from one surface to the other, even though the distance of the stagnation point from the tip varies somewhat between each case. Such variations would occur for differing induced angles-of-attack. These observations agree with the observations by Sears (1941) that an oscillating leading-edge and a stationary leading-edge subjected to vortex impingement "see" a sinusoidal incident flow. The sinusoidal flow will also be at the same frequency if $k=k_g$. The incident flow fields shown in figure 6.3 appear to be at the same frequency with a

relative phase angle between them equal to zero.

The magnitudes of the average orthogonal velocities in both cases are comparable except when the incident clockwise vortex approaches the stationary leading-edge and the magnitude increases substantially. This suggests that the influence of the incident vortex on the orthogonal velocity near the tip of the leading-edge is larger than the influence of edge motion alone since the stationary leading-edge is not located along the centerline of the impinging vortex street. This asymmetric alignment of the incident vortex street would account for the lower orthogonal velocity when the counter-clockwise vortex passes above the stationary edge. At this point, the velocities of the oscillating and stationary leading-edge more closely match, even though the streamline topologies and vorticity fields are much different. A tip vortex on the upper surface of the oscillating edge suggests its induced angle-of-attack is larger than that of the stationary leading-edge. Figure 6.4 indeed shows this to be the case.

Comparing the average measured velocity to the calculated induced velocity, orthogonal to the line of symmetry, reveals large differences in magnitude for both cases, with an unexpected asymmetry about the zero line for the oscillating leading-edge case. Furthermore, the measured velocity changes from a negative value to a positive value at $\beta=60°$, but the calculated velocity changes at $\beta=100°$. These observations suggest, that in both cases, the average orthogonal velocity is also significantly affected by other influences. These influences may include the presence of the tip vortex. In the case of the oscillating edge, a large influence was noted in chapter 5, when the angle of incidence of the entire flow field increased dramatically at $\beta=60°$. This global change in the incident flow field for the oscillating leading-edge may be due to the influence of the unsteady circulation about the entire flat plate that is generated by its own oscillation.

111
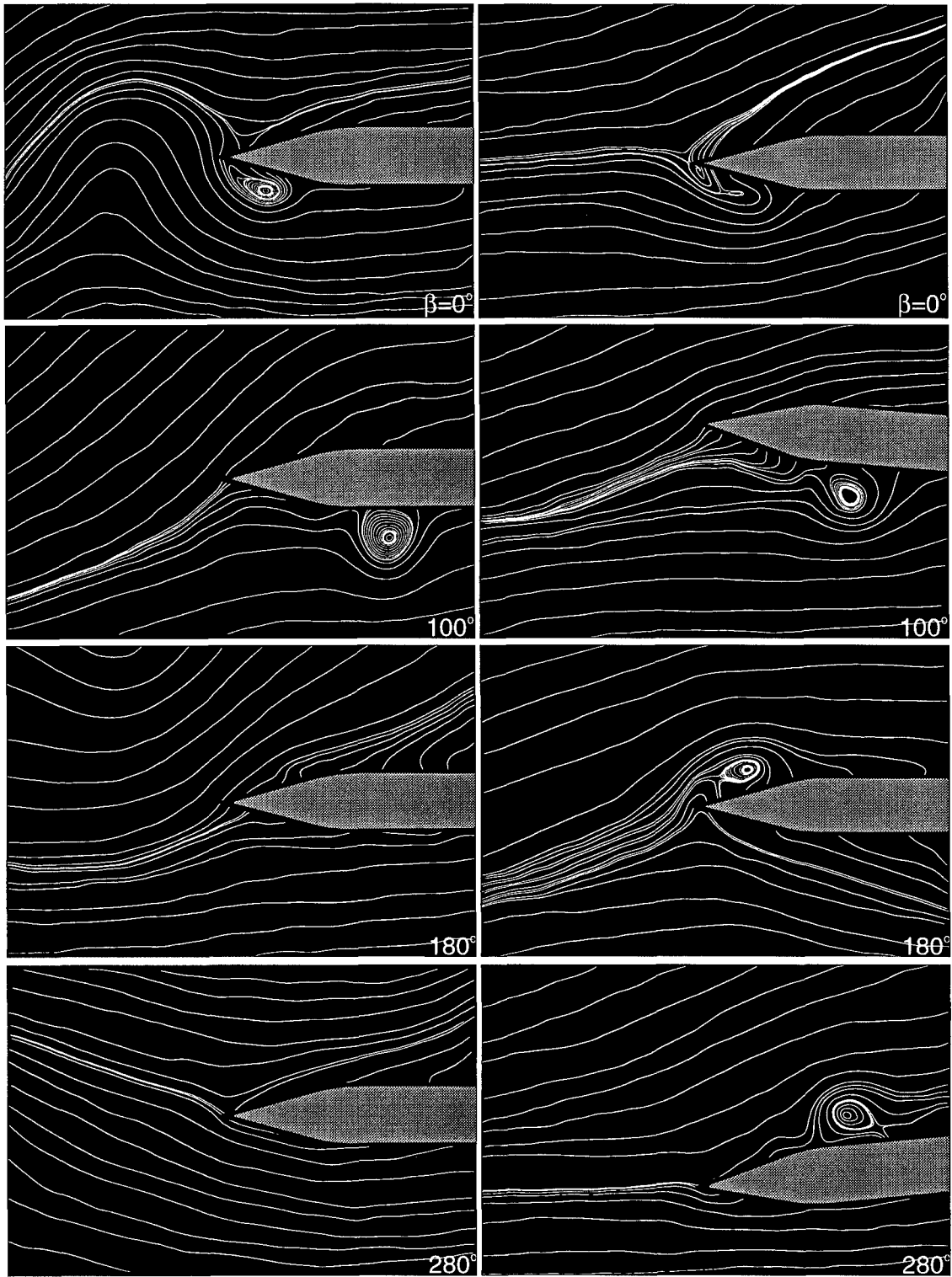
Figure 6.1: Comparison of streamline patterns in the laboratory reference frame for a stationary leading-edge (left column) with those of a leading-edge oscillating without an incident vortex (right column). Re=6,250.

112
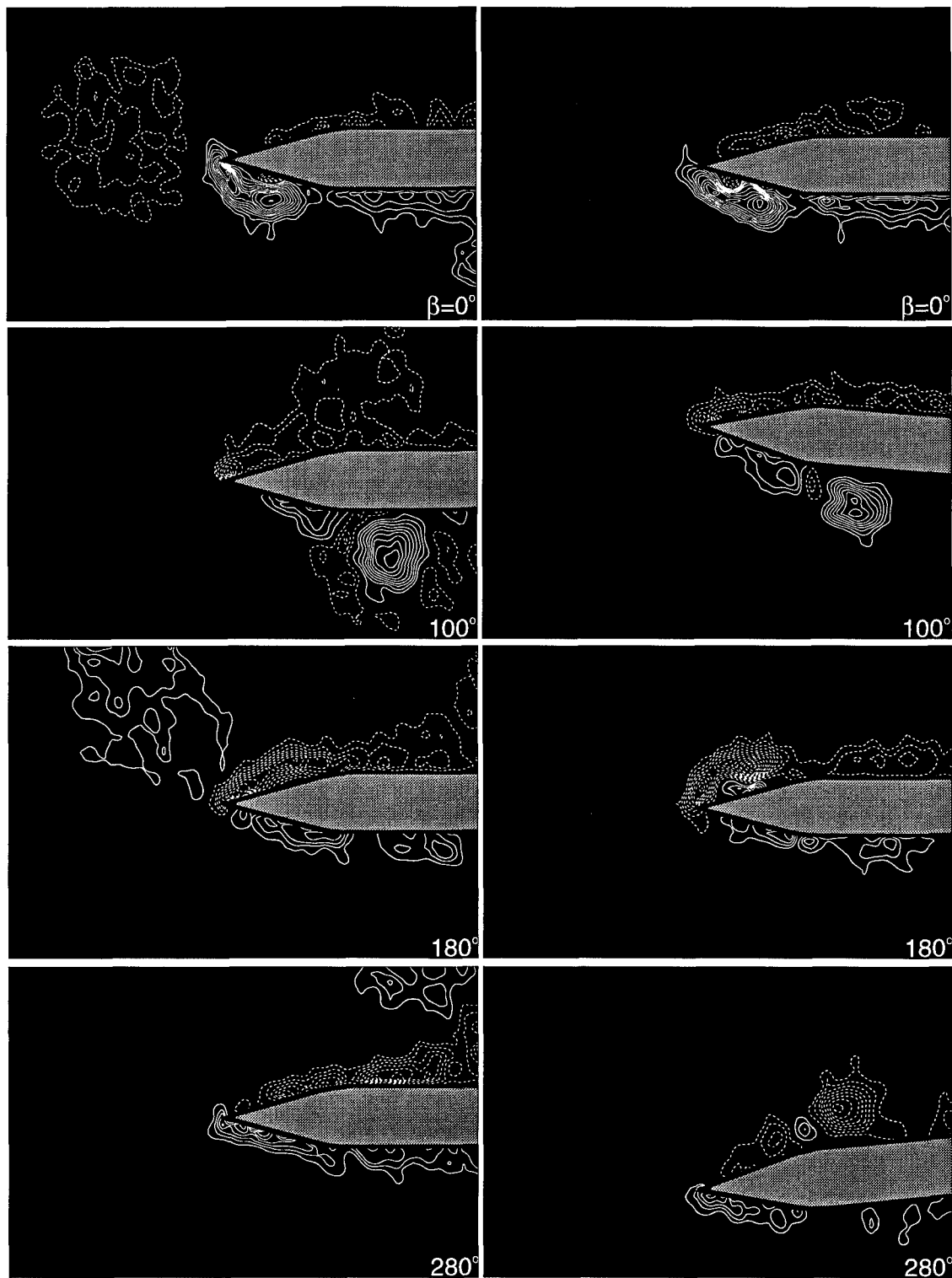
Figure 6.2: Comparison of the vorticity distributions for a stationary leading-edge (left column) with those of a leading-edge oscillating without an incident vortex (right column). $|\omega_{min}| = 5$ sec^{-1}; $\Delta\omega = 5$ sec^{-1}. Re= 6,250.

113
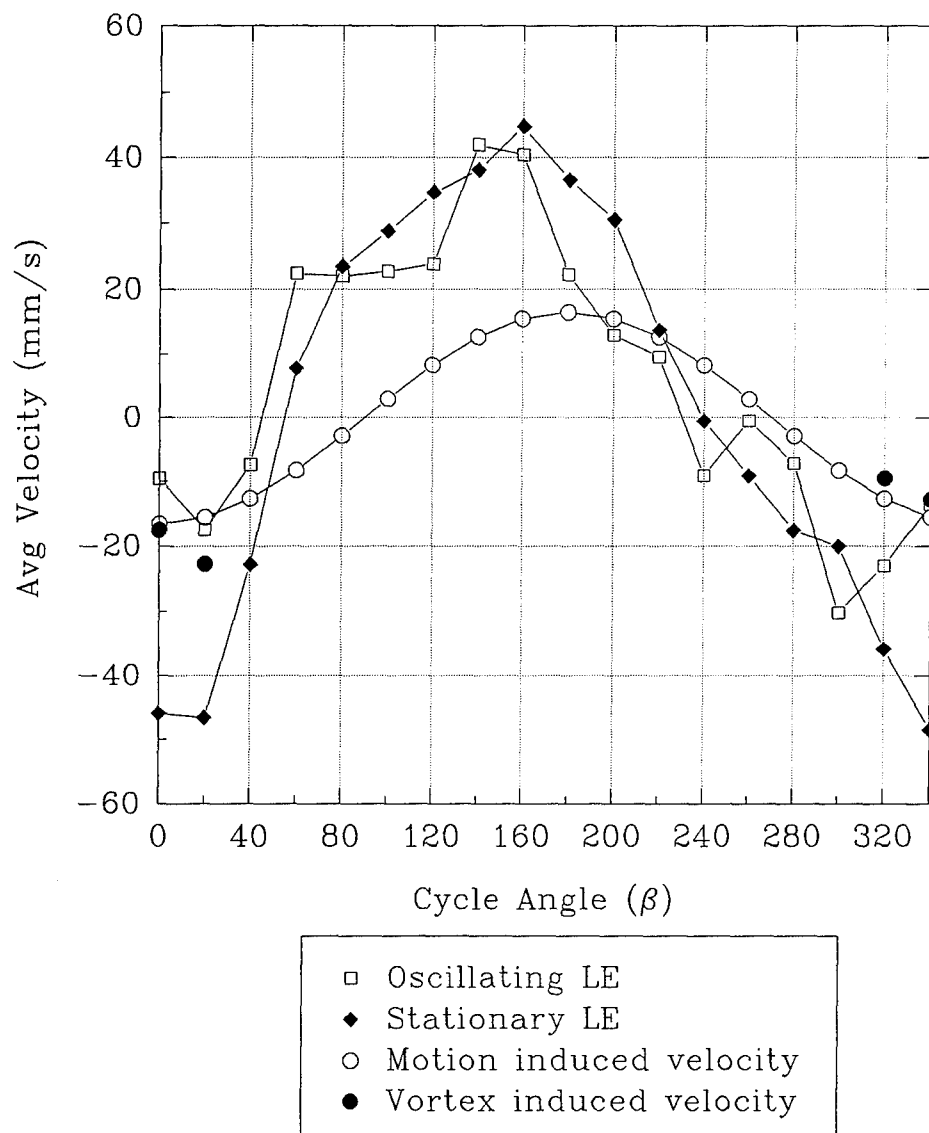
Figure 6.3: Average velocity orthogonal to the line of symmetry of an oscillating leading-edge without an incident vortex and a stationary leading-edge. The calculated velocities induced by tip motion alone and by a vortex incident upon a stationary leading-edge are also compared.

114
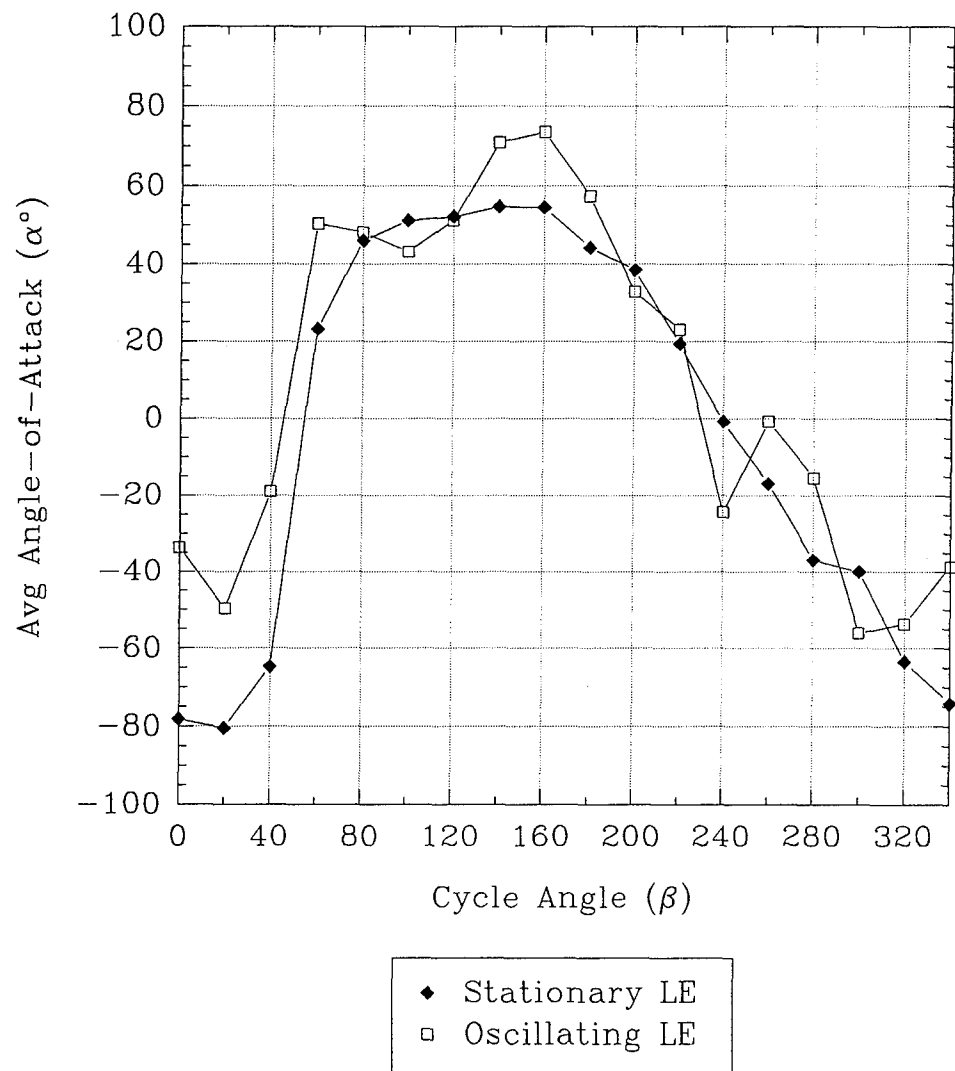
Figure 6.4: Average induced angle-of-attack at the tip of a stationary leading-edge with an incident vortex and an oscillating leading-edge without an incident vortex

115

6.2 Superposition of Flow Structure of a Stationary and Oscillating Leading-Edge

If the assumptions of non-stationary airfoil theory are met, as described in section 6.1.2, Sears (1941) demonstrated that the moment of an airfoil in a complex flow could be found by the superposition of the moments obtained in simpler flows. In this investigation the flow is considered quasi-two dimensional, with a maximum transverse displacement at the tip of the leading-edge being only 4.4% of the flat plate chord. Although a direct determination of the fluid dynamic forces over the entire flat plate cannot be made, some insight into the physical mechanisms of vortex interactions with an oscillating leading-edge may be gained by applying superposition. The total flux and circulation of local segments or cells upstream of and along the surface of the leading-edge, as well as the average velocity near the tip of a stationary leading-edge with an incident vortex (S) and an oscillating leading-edge without an incident vortex (NV) were added. These superposition curves are compared to the corresponding curves of a leading-edge oscillating at $\phi=0°$ and $180°$ with respect to an incident vortex street.

6.2.1   Local Circulation and Total Flux

Representative plots of the local circulation and total vorticity flux upstream and along the upper and lower surfaces of the leading-edge are shown in figure 6.5. The total vorticity flux is defined as $TF = \int u_0 \omega_z \, ds$, where ω_z and u_0 are respectively, the components of vorticity along, and velocity orthogonal to, a line segment s. The left column of figure 6.5 compares the superposition of the S and NV cases at $\beta=0°$ with the corresponding cycle angle of the oscillating leading-edge at $\phi=0°$. Since, for the $\phi=180°$ case, the incident clockwise vortex does not interact with the leading-edge until the second half of the oscillation cycle, the right column of figure 6.5 compares the superposition of the S case at $\beta=0°$ (when the incident vortex approaches the stationary

116

leading-edge) and the NV case at β=180°, to the φ=180° case at a cycle angle of β=180°.

In figure 6.5 the leading-edge surface extends approximately from x = 24 mm to 48 mm, corresponding to circulation cells 12-24. Upstream of the leading-edge in all the plots, the approaching clockwise rotating vortex is clearly evident. The superposition curves of total flux and circulation most closely match the magnitude and shape of the φ=0° and 180° curves upstream of the leading-edge. Along the surface of the leading-edge, the fluctuations of the superposition curves, namely the peaks and valleys, often match the location of the corresponding fluctuations in the φ=0° and 180° curves. However, the superposition magnitudes are much different, dramatically overshooting the φ=180° curves and either overpredicting or underpredicting the φ=0° curves.

6.2.2 Average Velocity

Figure 6.6 depicts the velocities orthogonal to the symmetry line of the leading-edge that have been averaged along a 4 mm segment upstream of the tip. Corresponding averages of the induced angle-of-attack α at the leading-edge are shown in figure 6.7. In both figures, the curves with dashed lines are the superposition curves where at each cycle angle for the φ=0° case, velocities from S have been added to those of NV. At each cycle angle β for the φ=180° case, the velocities for S at β+180° are added to the NV velocities at β.

Referring to figure 6.6, the superposition curves predict remarkably well the fluctuations and overall shape of the corresponding φ=0° and φ=180° curves, but their magnitudes usually exceed those of the φ=0° and 180° curves. Considering the general trends of the curves, it is interesting to note the magnitudes of the φ=180° curve are usually within +/- 20 mm/s, while the magnitudes of the φ=0° curve vary between +/- 80 mm/s. When β=220° to 320°, the superposition curve varies most from the φ=180°

117

curve. During these cycle angles in the ϕ=180° case, the incident clockwise vortex convects along the upper surface of the leading-edge.

In figure 6.7, the curves for the ϕ=0° case appear sinusoidal and reach high values of angle-of-attack, essentially doubling the angle-of-attack in the ϕ=180° case. The ϕ=180° curves in figure 6.7 are generally not sinusoidal. The trend of the superposition curve departs significantly from the ϕ=180° curve at β=60° to 140° and 220° to 280°. In the ϕ=0° case, the superposition curve generally follows the trend of the measured curve.

6.2.3   Concluding Remarks

The superposition of local circulation and total vorticity flux from the S and NV cases closely resembled the ϕ=0° and ϕ=180° curves upstream of the leading-edge where the flow is essentially inviscid. This was not the case along the surface of the leading-edge, although the fluctuations of the curves matched fairly well. This suggests the separation effects at the tip and the interactions of the tip vortex with the surface alter the magnitudes of the circulation and total flux.

It was anticipated that the superposition curves of average orthogonal velocity near the tip and the corresponding curves of average induced angle-of-attack would closely match both the magnitude and shape of the corresponding ϕ=0° and 180° curves. However, this did not occur, with the exception that the fluctuations of the superposition curves were very similar. This suggests the fluctuations of the ϕ=0° and ϕ=180° flow fields can indeed be approximated by superposition but the magnitudes will not be correct since the influence of separation significantly influences the flow field near the tip

Larger discrepancies between the superposition curve and the ϕ=180° curve at β=220° to 280° correspond to the convection of the incident vortex above the leading-edge. This suggests that some of the differences in magnitude of the average velocity

118

and angle-of-attack are also due to a shift in the position of the incident vortex. Since the incident vortex never convected entirely above the stationary leading-edge in this investigation, the effect of a change in its position cannot be accounted for in the superposition curve.
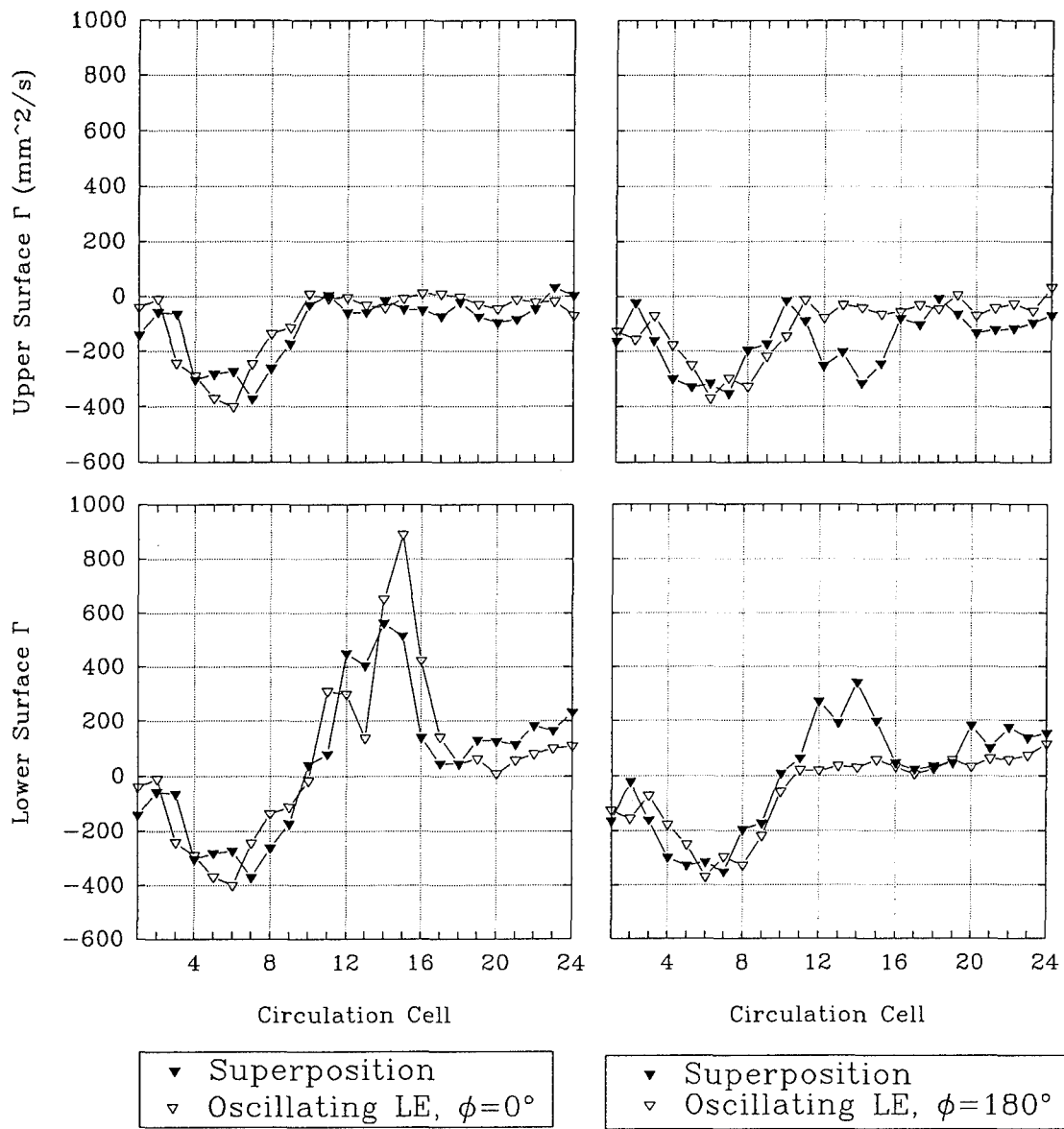
Figure 6.5a: The local circulation upstream and along the upper and lower surface of a leading-edge oscillating at φ=0° and φ=180° compared to the corresponding circulation obtained by superposition.

120
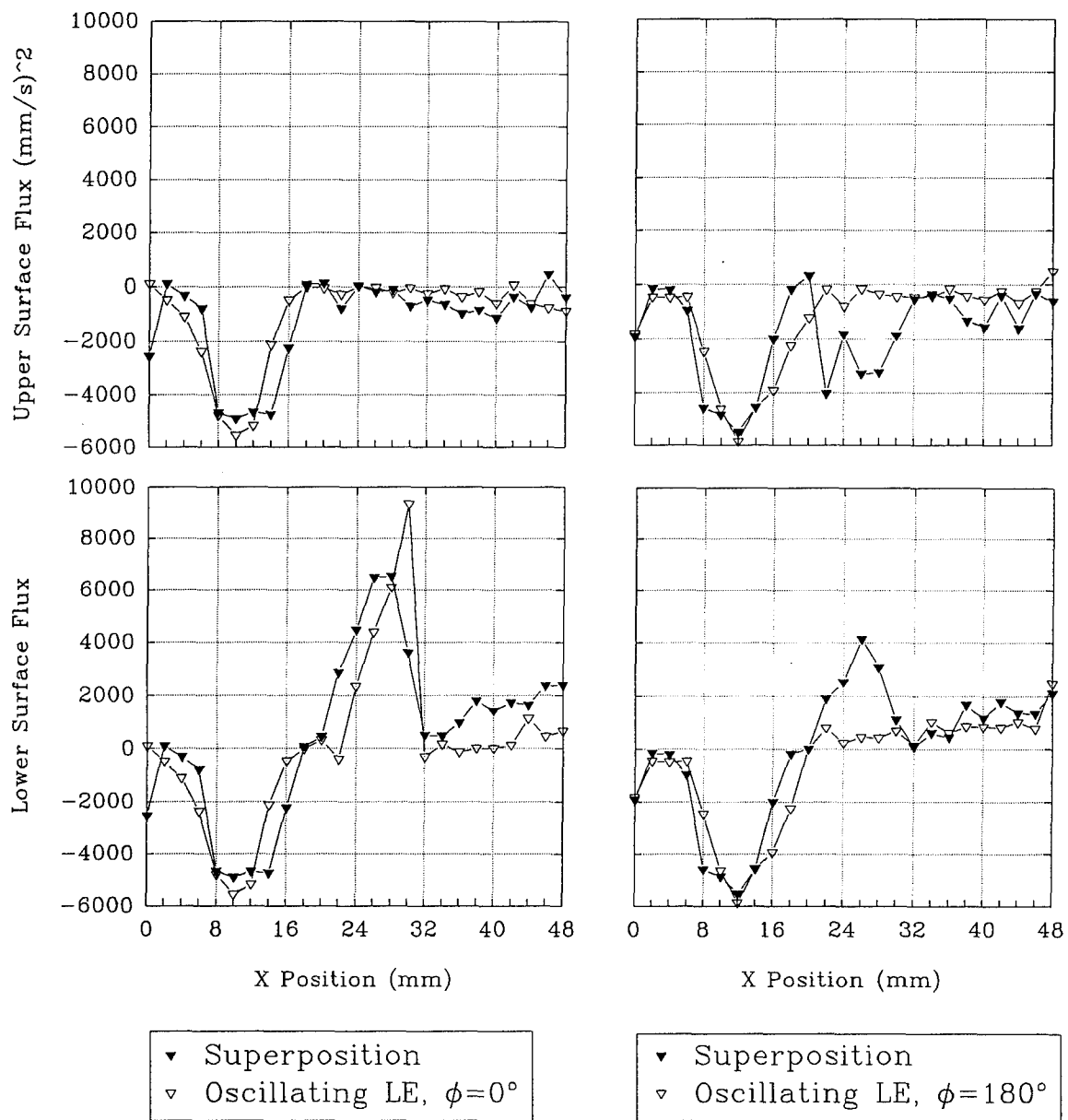
Figure 6.5b: The total vorticity flux upstream of and along the upper and lower surface of a leading-edge oscillating at $\phi=0°$ and $\phi=180°$ compared to the corresponding flux obtained by superposition.

121
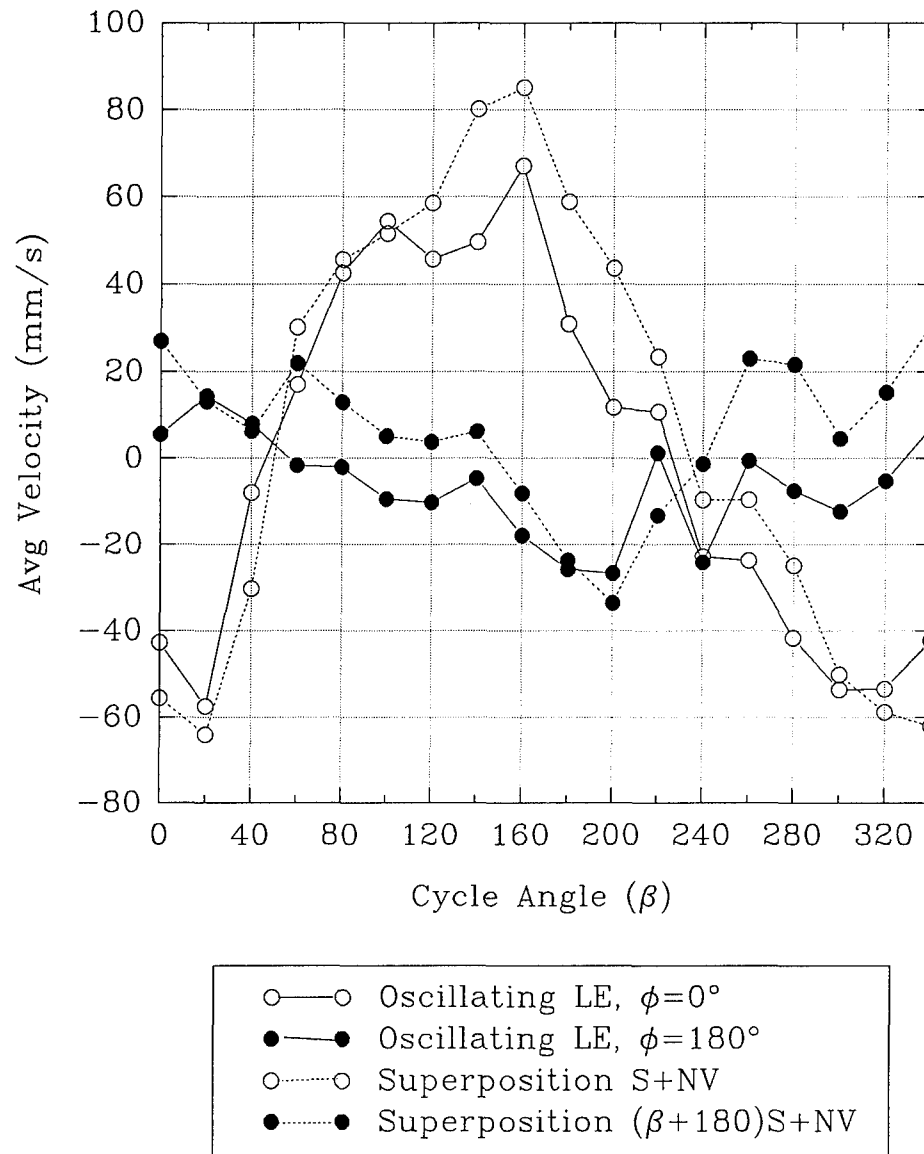
Figure 6.6: The average velocity orthogonal to the line of symmetry of a leading-edge oscillating at φ=0° and φ=180° is compared to the velocity obtained by superposition.
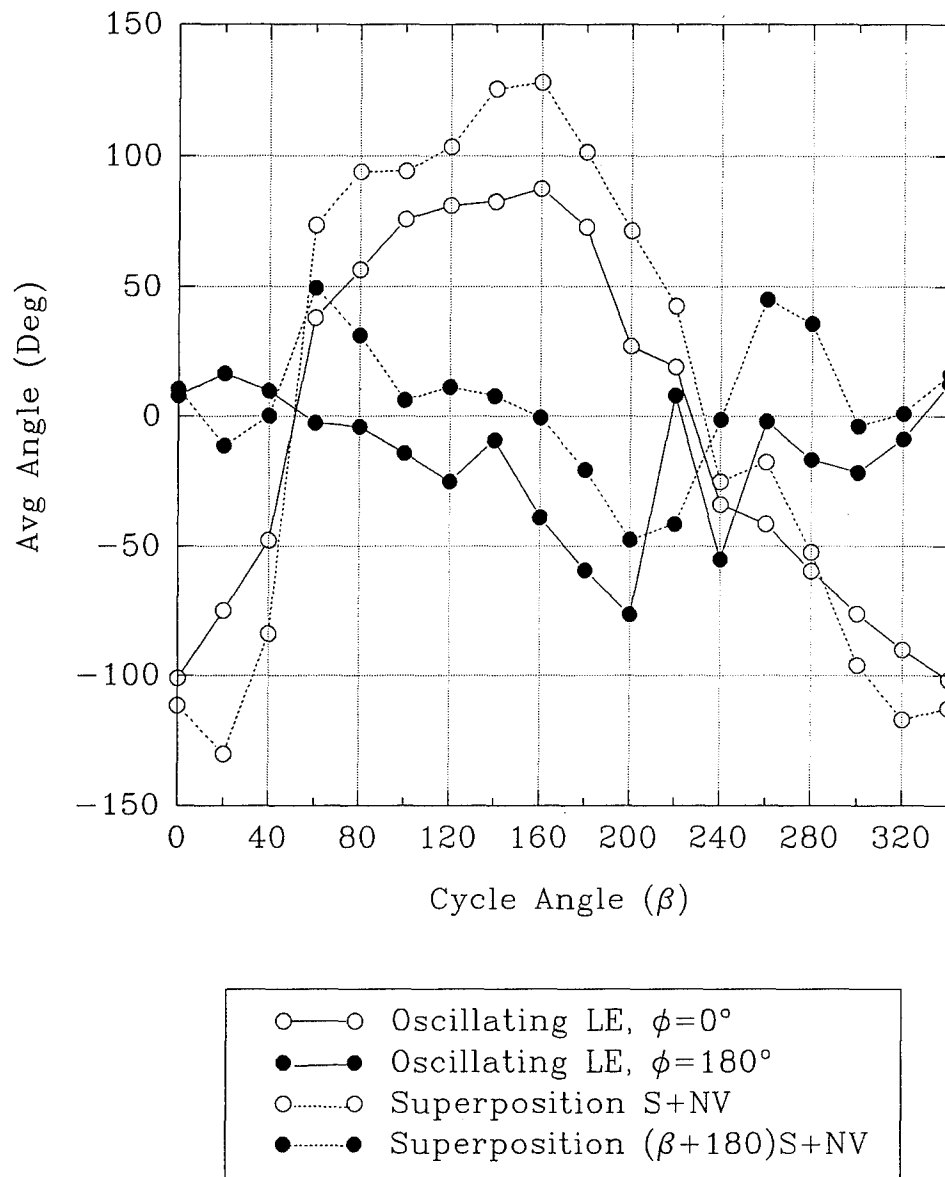
Figure 6.7: The average induced angle-of-attack of a leading-edge oscillating at $\phi=0°$ and $\phi=180°$ is compared to the angle-of-attack obtained by superposition.

6.3 Effect of Phase Angle

Interactions of a vortex with a stationary leading-edge and with a leading-edge oscillating at $\phi=0°$ and $180°$ relative to the vortex are examined in this section by comparing instantaneous flow structure, local circulation and vorticity flux across the tip of the leading-edge. These comparisons are used to highlight the effects of varying phase angle.

6.3.1 Flow Structure

The instantaneous flow structure just prior to the impingement of an incident clockwise vortex is shown in figures 6.8-6.10 for the stationary leading-edge and the leading-edge oscillating at $\phi=0°$ and $180°$. In figure 6.8 the vorticity distributions reveal the location of the incident vortex just upstream of the tip. When the leading-edge is stationary, the centroid of the incident vortex appears slightly above an imaginary extension of the symmetry line of the leading-edge. When the leading-edge oscillates at $\phi=0°$, the induced velocity at the tip due to motion alone is in the negative y direction. The centroid of the incident vortex in this case appears slightly below the symmetry line. Conversely, when the edge oscillates at $\phi=180°$ and the induced velocity is in the positive y direction, the centroid is substantially above the line of symmetry. Furthermore, the tip and surface vortices formed on the lower wedge surface of the stationary leading-edge are enlarged when the leading-edge oscillates at $\phi=0°$ and non-existent when the leading-edge oscillates at $\phi=180°$.

Figure 6.9 shows the streamline patterns in the laboratory reference frame corresponding to the vorticity patterns in figure 6.8. A half-saddle point is seen on the upper wedge surface of the stationary leading-edge, becoming a saddle-point above the tip when the leading-edge is oscillating at $\phi=0°$ and disappearing entirely when

124

oscillating at $\phi=180°$. For the stationary leading-edge, a series of concentric circles nested within two limit cycles appears along the lower wedge surface and corresponds to the tip vortex seen in figure 6.8. When the leading-edge oscillates at $\phi=0°$, the topology corresponding to the tip vortex appears enlarged and more dominant and, with the exception of a stable focus at the center, is identical to the topology in the stationary case. When the leading-edge oscillates at $\phi=180°$, all critical points disappear.

The streamline patterns in a moving reference frame are shown in figure 6.10. In this reference frame, the topology shown for the stationary leading-edge changes in the two oscillating edge cases. Most significant is the disappearance of the critical points along the lower wedge surface for the $\phi=180°$ case.

6.3.2 Local Circulation

Figure 6.11 compares the local circulation upstream and along the upper and lower surfaces of the leading-edge for the three vortex interaction cases, at the cycle angles shown in figures 6.8-6.10. In all the cases, the negative profile of the incident clockwise vortex is clearly visible upstream of the leading-edge. Along the lower surface of the stationary leading-edge, a circulation peak at cell 12 and a slightly larger peak at cell 14 are associated with the tip vortex. Comparing this to the lower surface in the $\phi=0°$ case, similar dual peaks that are wider and more distinct are visible with the largest peak reaching a value approximately three times that of the corresponding peak in the stationary edge case. In addition, the "valley" between the two peaks is at the same cell location as the valley in the stationary edge case. In contrast to the previous two cases, no prominent peaks along the upper or lower surfaces of the leading-edge oscillating at $\phi=180°$ are visible. Instead, there are lower levels of fluctuating circulation which are nearly symmetric about the line of symmetry of the leading-edge.

6.3.3 Vorticity Flux across the Tip of the Leading-Edge

The vorticity flux orthogonal to the line of symmetry of the leading-edge in the stationary and oscillating leading-edge cases is shown in figure 6.12. In general, the magnitude of the flux is largest when the leading-edge oscillates at $\phi=0°$ and smallest when oscillating at $\phi=180°$. During much of the oscillation cycle in the $\phi=180°$ case, there is little vorticity flux across the tip. The exceptions occur when the incident clockwise vortex convects above the upper surface.

For the $\phi=180°$ case, notable changes in the flux occur at $\beta=200°$, $220°$, $240°$ and $300°$, and at $\beta=20°$, $40°$, $60°$ and $100°$ for the stationary and $\phi=0°$ cases. The vorticity flux at $\beta=240°$ in the $\phi=180°$ case exceeds the corresponding flux for the $\phi=0°$ and stationary edge cases at $\beta=60°$. Referring to the instantaneous vorticity distributions of figures 4.1 and 5.8, it can be seen that at $\beta=60°$ in the stationary and $\phi=0°$ cases, the incident vortex is being distended and split as it impinges the leading-edge. From figure 5.15, at $\beta=240°$ in the $\phi=180°$ case, the entire incident vortex is just above the leading-edge, where it was shown to override the influence of edge oscillation.

6.3.4 Concluding Remarks

Varying the phase angle of the leading-edge oscillation with respect to an incident clockwise vortex has a dramatic effect on the developing flow structure, circulation and vorticity flux sweeping across the tip of the leading-edge. In general, the instantaneous flow structure and associated topology observed during vortex interactions with a stationary leading-edge are enhanced when the leading-edge oscillates at $\phi=0°$, and essentially removed when oscillating at $\phi=180°$. Similarly, the level of local circulation along the surface of the stationary leading-edge is amplified three times when the leading-edge oscillates at $\phi=0°$ and disappears when it oscillates at $\phi=180°$. The transverse position of the incident vortex is also observed to shift in the direction

opposite to the motion of the edge. This suggests that the velocity field induced when the leading-edge oscillates has considerable upstream influence and causes the shift.

Finally, the flux of vorticity orthogonal to the line of symmetry of the leading-edge is generally larger when the leading-edge oscillates at $\phi=0°$ and smaller when oscillating at $\phi=180°$, in comparison with that due to vortex interaction with a stationary leading-edge. In the $\phi=180°$ case, it was shown that the vorticity flux was significantly altered when the position of the incident vortex, relative to the leading-edge, influenced the flow more than the effects of edge oscillation alone.

STATIONARY
LEADING-EDGE

OSCILLATING
LEADING-EDGE
$\phi = 0°$
(Upstroke)

OSCILLATING
LEADING-EDGE
$\phi = 180$
(Downstroke)

$\beta = 0°$

$0°$

$180°$
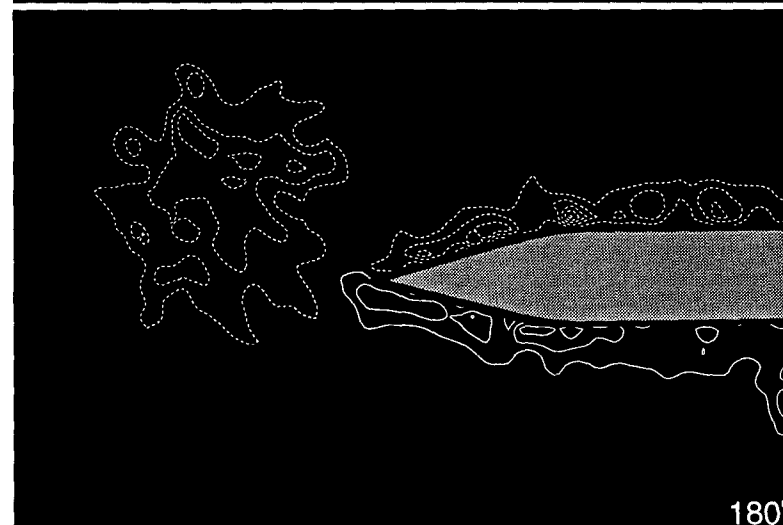
Figure 6.8: Instantaneous vorticity distributions showing the interaction of an incident clockwise vortex with a stationary and oscillating leading-edge. The minimum contour level is $|\omega_{min}| = 5 \ sec^{-1}$, with negative contour intervals $\Delta\omega = 5 \ sec^{-1}$ and positive contour intervals $\Delta\omega = 10 \ sec^{-1}$.

128

STATIONARY
LEADING-EDGE
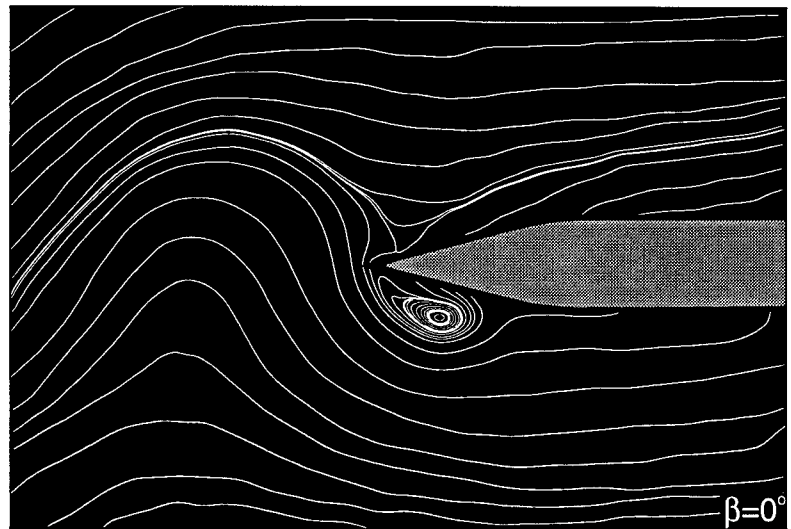
OSCILLATING
LEADING-EDGE
$\phi=0°$
(Upstroke)
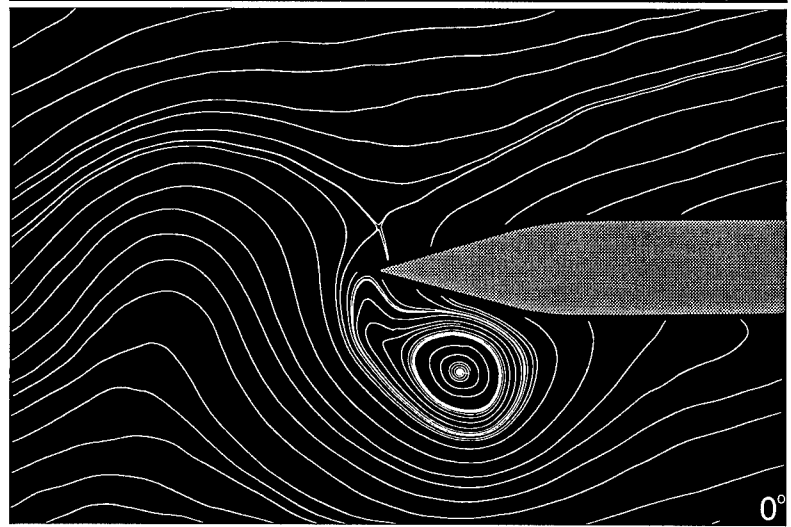
OSCILLATING
LEADING-EDGE
$\phi = 180$
(Downstroke)
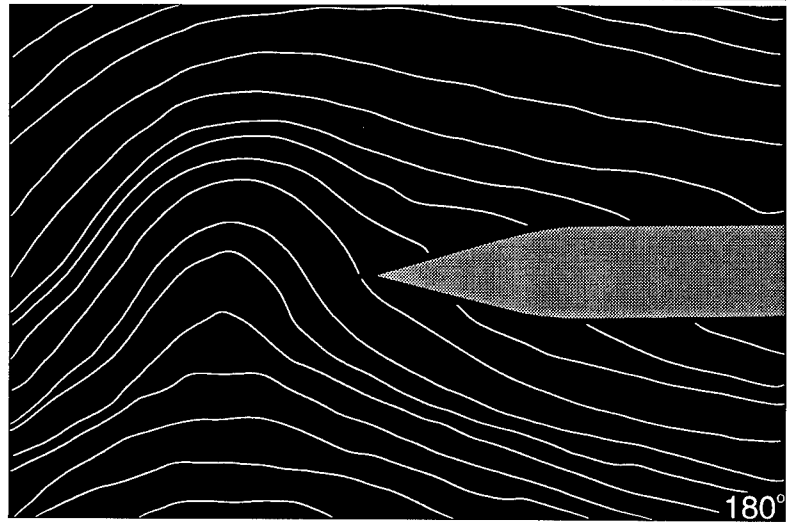
Figure 6.9: Instantaneous streamline patterns in the laboratory reference frame showing the interaction of an incident clockwise vortex with a stationary and oscillating leading-edge. Re= 6,250.

129

STATIONARY
LEADING-EDGE

OSCILLATING
LEADING-EDGE
$\phi=0°$
(Upstroke)

OSCILLATING
LEADING-EDGE
$\phi = 180$
(Downstroke)

$\beta=0°$

$0°$

$180°$
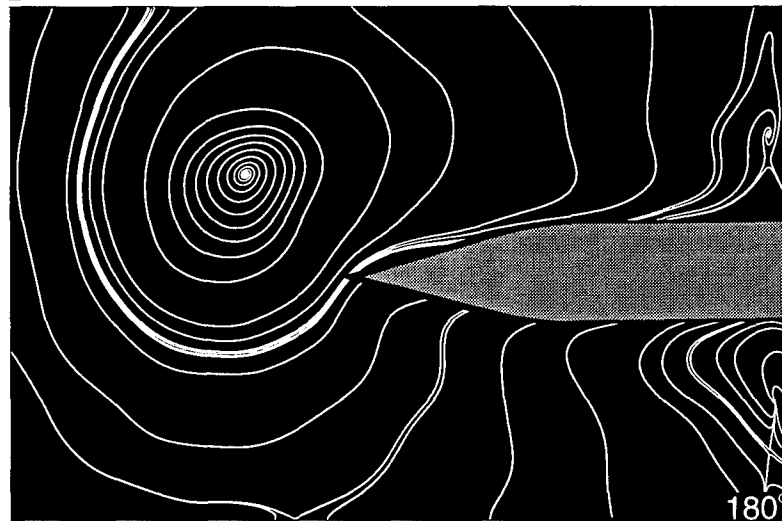
Figure 6.10: Instantaneous streamline patterns in a moving reference frame showing the interaction of an incident clockwise vortex with a stationary and oscillating leading-edge. Re= 6,250.

130
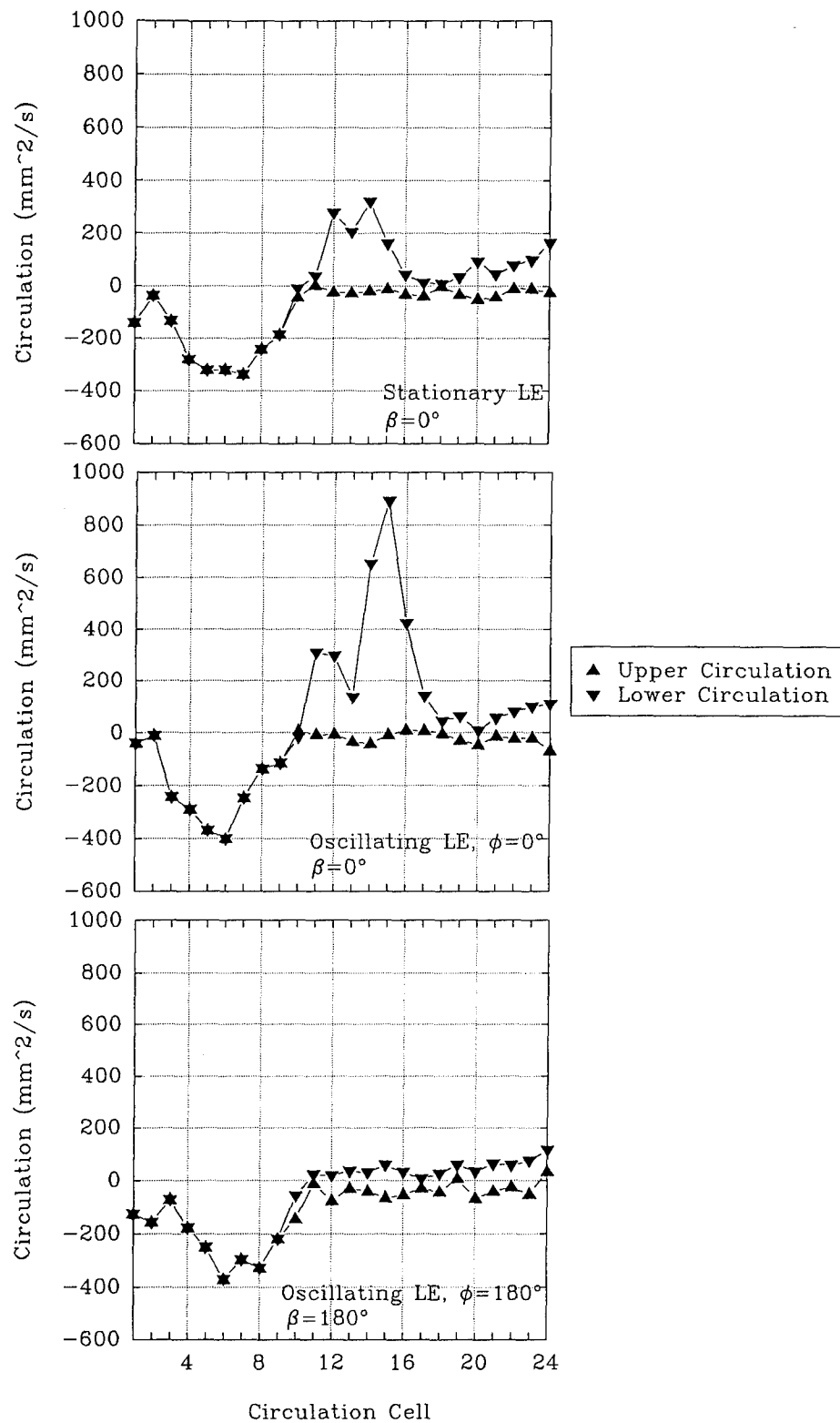
Figure 6.11: Local circulation upstream of and along the upper and lower surfaces of a leading-edge

131
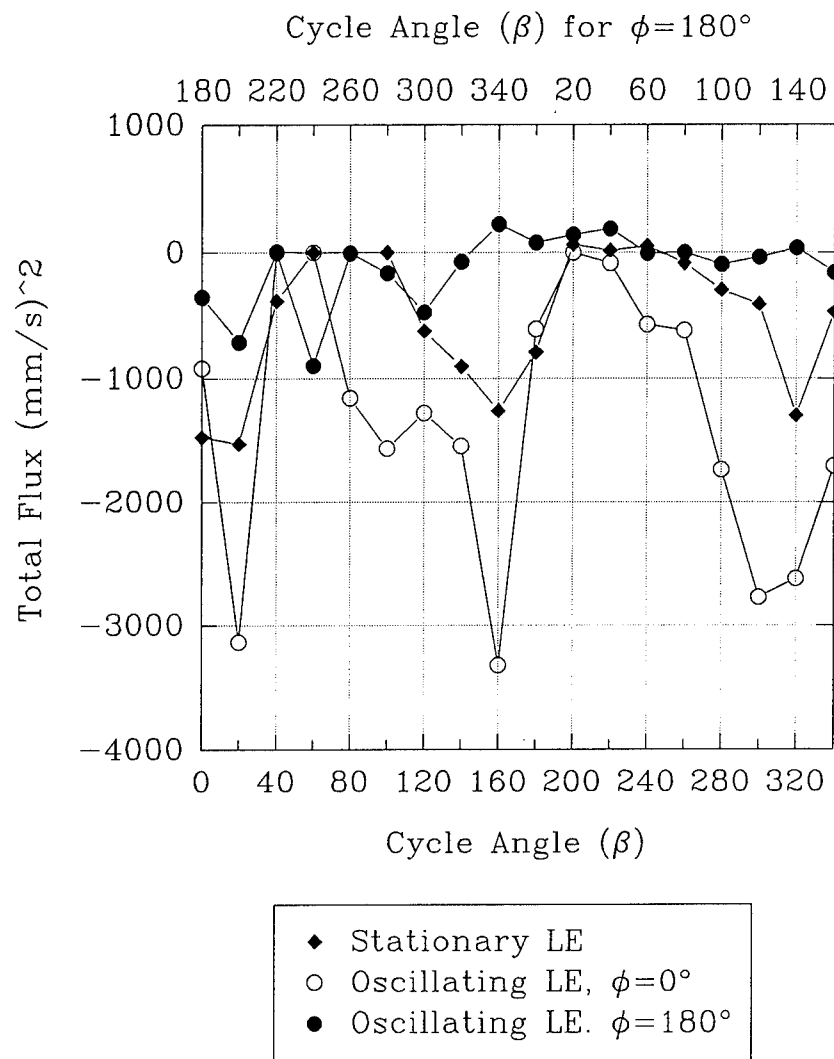
Figure 6.12: Total vorticity flux orthogonal to the line of symmetry of a leading-edge

6.4 Stages of Vortex Development Along the Surface of the Leading-Edge

For all the cases of vortex interactions presented, with the exception of a leading-edge oscillating at ϕ=180°, a tip vortex formed along the surface of the leading-edge and later induced the formation of a surface vortex. Identifiable stages in the development of each vortex can be classified according to the vorticity distributions and streamline patterns in the laboratory reference frame. The stages of vortex development along the surface will be established using the baseline case of a clockwise vortex impinging a stationary leading-edge. Each of the defined stages will then be identified, where possible, when the leading-edge oscillates. Possible causes of each stage of vortex development will also be suggested.

6.4.1   Stationary Leading-Edge

Figure 6.13 depicts the instantaneous vorticity distributions and streamline patterns in the laboratory frame in which six stages of tip vortex development during the interaction of a clockwise vortex with a stationary leading-edge are identified. The descriptions of the stages of development will be done by describing characteristics seen in figure 6.13. However, these descriptions would also apply for interactions with a counterclockwise vortex except the stages of development would occur on the opposite surface of the edge with vorticity of opposite sign.

Stage one in the development of the tip vortex begins when significantly higher levels of positive vorticity are concentrated near the tip, within which discrete peaks of vorticity are also visible. A gap also appears between the concentrations of vorticity along the lower wedge surface, but no contours of negative vorticity, which correspond to the formation of a surface vortex, are evident within the gap. The streamline topology depicts a half-saddle point on the upper wedge surface and a focus nested within a limit

133

cycle along the lower wedge surface.

Stage two is marked by the initial formation of a surface vortex as indicated by the appearance of negative vorticity between the lower wedge surface and the tip vortex. In addition, the positive vorticity peaks within the tip vortex are more clearly defined with approximately equal levels of vorticity concentration. The topology does not change significantly from stage one.

Stage three is identified by the change in the tip vortex topology where an unstable node and saddle point appear adjacent to the lower wedge surface, upstream of the original nested focus. In addition, the half-saddle point of stage two on the upper surface rises above the surface becoming a full saddle point. The vorticity distributions also show significant growth of the surface vortex with increasing levels of negative vorticity. Furthermore, the vorticity peaks of the tip vortex appear imbalanced with the aft peak reaching much higher levels than the peak just below the tip.

Stage four begins when the saddle point above the upper wedge surface in stage three moves to the very tip of the leading-edge, becoming again a half-saddle point. Concurrently, the tip and surface vortices begin to convect downstream along the lower surface, evidenced by comparing the locations of the tip vortices in stage four with those in stage three. Finally, the positive vorticity contours of the tip vortex are all below the line of symmetry of the leading-edge. These events mark the end of positive vorticity production from the upper surface which feeds into the tip vortex. This conclusion is substantiated by the curve of vorticity flux shown in figure 6.12. The continual imbalance of the positive vorticity peaks therefore indicates vorticity from the upstream peak is being transported to the peak downstream, which also appears to have detached from the lower surface.

Stage five is identified in the vorticity distributions by the splitting of the tip vortex into two independent vortices A and B, allowing the release of the surface vortex. The

upstream B vortex continues to convect along the lower wedge surface while vortex A appears to distend the surface vortex. The corresponding streamline patterns show that the saddle point, previously adjacent to vortex A, moves to the lower surface and becomes a half-saddle point. Furthermore, a stagnation line appears on the lower wedge surface near the tip.

Stage six is denoted when the surface vortex has been pulled away from the lower surface by tip vortex A. Vortex A also appears to convect away from the lower surface while vortex B continues to convect along the surface.

6.4.2   Oscillating Leading-Edge

As shown in chapter five, a tip vortex develops when the leading-edge oscillates without an incident vortex or at $\phi=0°$ relative to an incident vortex. Although there are differences in the flow field of each case leading to the development of the tip vortex, most of the six stages identified in the baseline stationary leading-edge case are also observed in the oscillating leading-edge cases. These stages are identified in figures 6.14-6.15.

6.4.2.1   Oscillating Leading-Edge without an Incident Vortex

From figure 6.14, five of the six stages of tip vortex development are observed when the leading-edge oscillates without an incident vortex. Stage one actually begins at $\beta=300°$, even though the streamline patterns differ somewhat from the those in the baseline case for stage one development. Stage two is not identified since the tip vortex streamline topology on the lower wedge surface visibly splits at $\beta=340°$ before the vorticity contours show any negative vorticity indicating the formation of a surface vortex (see figures 5.1 and 5.6). Stage three is therefore identified after the surface vortex is visible at $\beta=0°$. As in the baseline case, stage four occurs when the half-saddle

135

point or stagnation line is on the tip, and the tip and surface vortices begin to convect. Interestingly, the vorticity contours show the tip vortex has split, which is a stage five characteristic in the baseline case. However, unlike the baseline case, in stage four the surface vortex does not appear to extend beyond the tip vortex even with a gap present. Stage five occurs at $\beta=100°$ when the streamline patterns show the stagnation line moves to the lower wedge surface. Vorticity distributions also indicate that tip vortex A and the surface vortex are detached. Finally, stage six is identified when the streamline pattern shows a half-saddle-point on the lower surface adjacent to the unstable focus corresponding to tip vortex A.

6.4.2.2   *Oscillating Leading-Edge at $\phi=0°$ Relative to an Incident Vortex*

All six stages of tip vortex development are observed in figure 6.15 along the lower surface when the leading-edge oscillates at $\phi=0°$. At $\beta=300°$, stage one characteristics are very similar to the baseline except a full saddle-point is seen above the upper surface. Stage two occurs at $\beta=320°$ when the surface vortex initiates along the lower wedge surface. Stage three is identified when the streamline topology denoting the tip vortex splits. This topology closely resembles the baseline topology. However, the vorticity distribution is much different than the baseline case and reveals an apparent eruption of the surface vortex, which splits the tip vortex. As shown in figure 5.8, the tip vortex recombines at the next cycle angle. Stage four occurs at $\beta=60°$ when convection is most noticeable and a half-saddle point occurs at the tip. Although in stage five the streamline topology along the lower surface is more complex than the baseline, a half-saddle point on the lower surface adjacent to the tip vortex topology, and a stagnation line on the lower wedge surface are evident. Stage six is identified when, according to the vorticity distribution, the surface vortex appears to detach from the lower surface.

6.4.3   Concluding Remarks

Six stages of tip vortex development were defined as a baseline using instantaneous vorticity distributions and streamline patterns in the laboratory frame during vortex interactions with a stationary leading-edge. Nearly all of the stages could be identified when the leading-edge oscillates without an incident vortex and at $\phi=0°$ relative to an incident vortex. However, the vorticity distributions or topology of an identified stage often did not exactly match those of the baseline stage. For example, when the topology of the tip vortex split during stage three, the vorticity distributions may or may not have indicated the split. The streamline patterns for stages three, four and five were more heavily considered when determining when a particular stage occurs during the oscillation cycle. In the case of the oscillating leading-edge without an incident vortex, stage two could not be identified.

In general, the first three stages of tip vortex development were found to occur in all cases when the induced angle-of-attack (α) at the tip of the leading-edge is negative (see figure 6.16). Vorticity flux across the tip, shown in figure 6.17 for the three cases considered, reaches its highest levels during stages one through three. Furthermore, when the leading-edge oscillates, the first three stages occur earlier in the oscillation cycle than for a stationary leading-edge. From figure 6.16, α becomes more negative earlier in the oscillation cycle when the leading-edge oscillates at $\phi=0°$ or without an incident vortex, than when the leading-edge is stationary. These findings suggest that development of the tip vortex in the first three stages depends significantly on the incident flow field and the resulting production and flux of vorticity from the upper surface.

It was found that stage four always occurs at $\beta=60°$, when α first becomes positive. This also corresponds to the moment the half-saddle point is coincident with the tip and the tip vortex begins to convect. Furthermore, the vorticity flux across the tip is zero or

137

toward the upper surface at this cycle angle. This suggests that vorticity from the upper surface no longer accumulates within the tip vortex and that the development of the tip and surface vortices for stages four through six depends more upon the local interaction between the individual vortices and the surface.
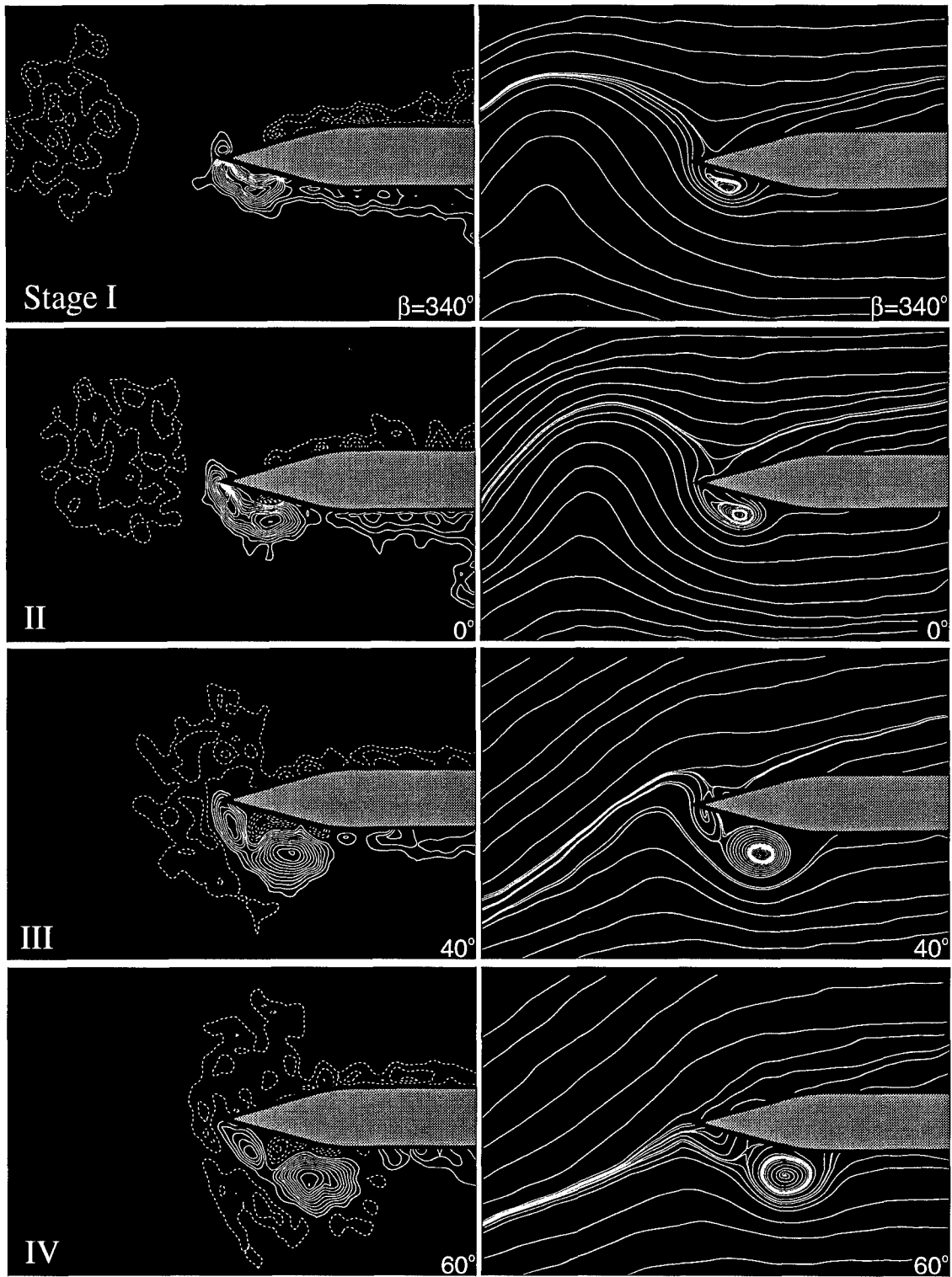
Figure 6.13: Instantaneous vorticity distributions and streamline patterns in the laboratory reference frame depicting the stages of tip vortex development for a stationary leading-edge with an incident clockwise vortex. $|\omega_{min}| = 5$ sec^{-1} and $\Delta\omega = 5$ sec^{-1}. Re = 6,250.
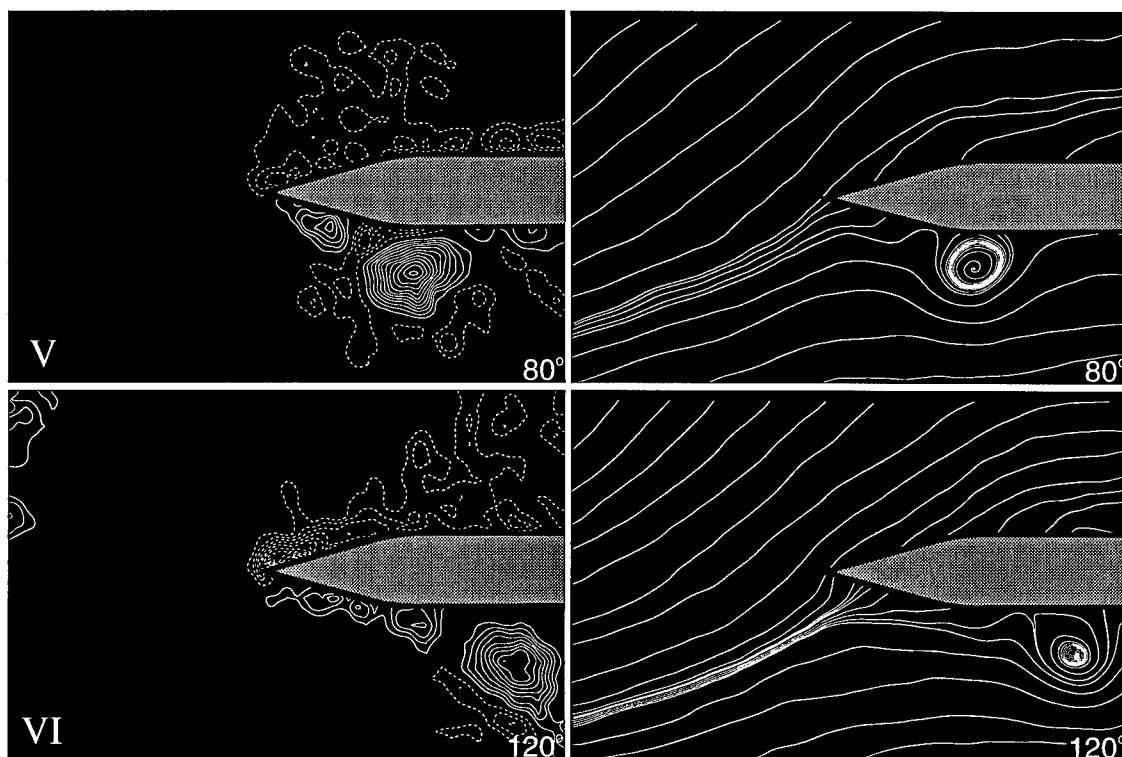
Figure 6.13: (Continued)
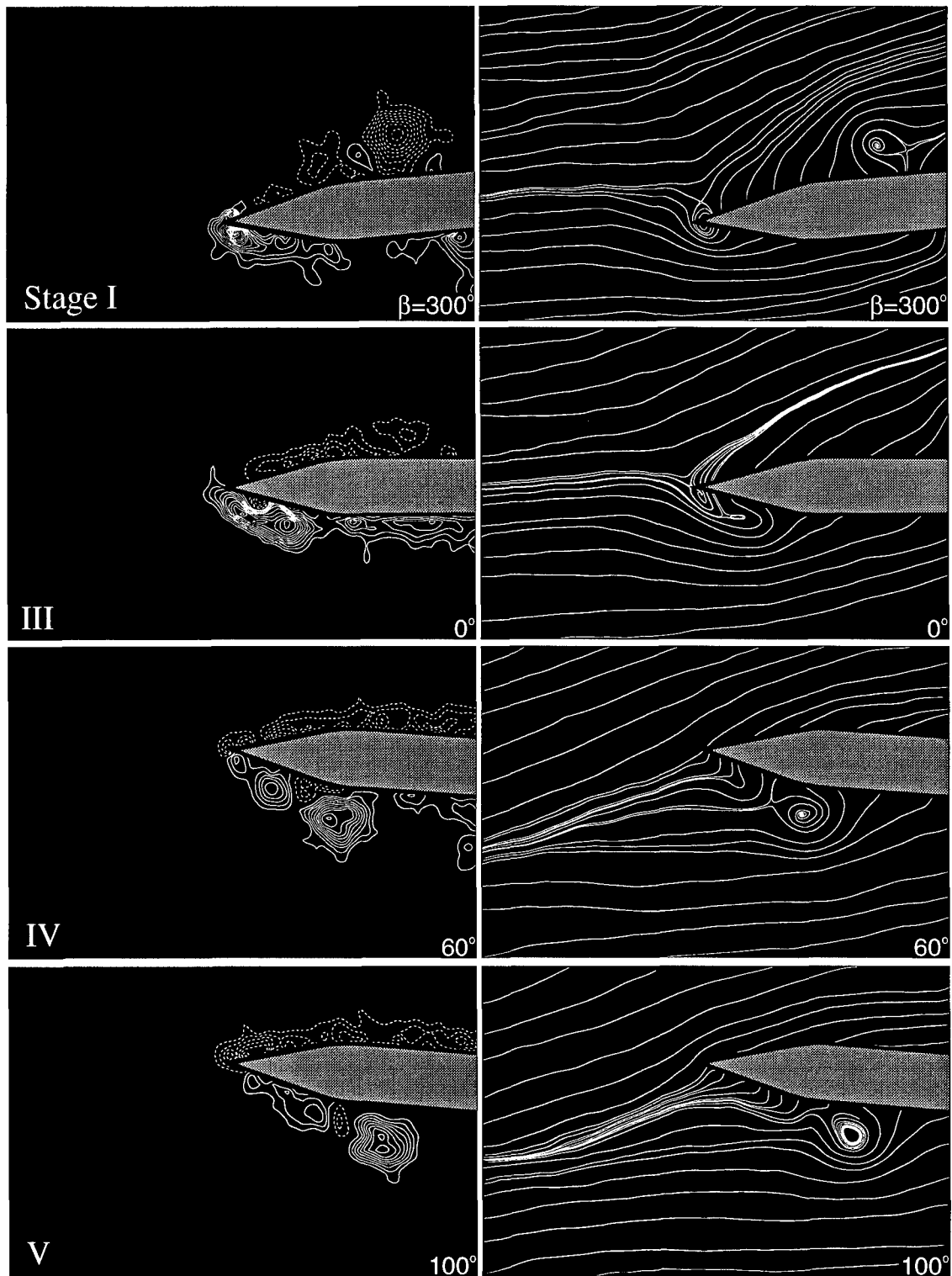
Figure 6.14: Instantaneous vorticity distributions and streamline patterns in the laboratory reference frame depicting the stages of tip vortex development for an oscillating leading-edge without an incident vortex. $|\omega_{min}| = 5$ sec^{-1} and $\Delta\omega = 5$ sec^{-1}. Re = 6,250.

141
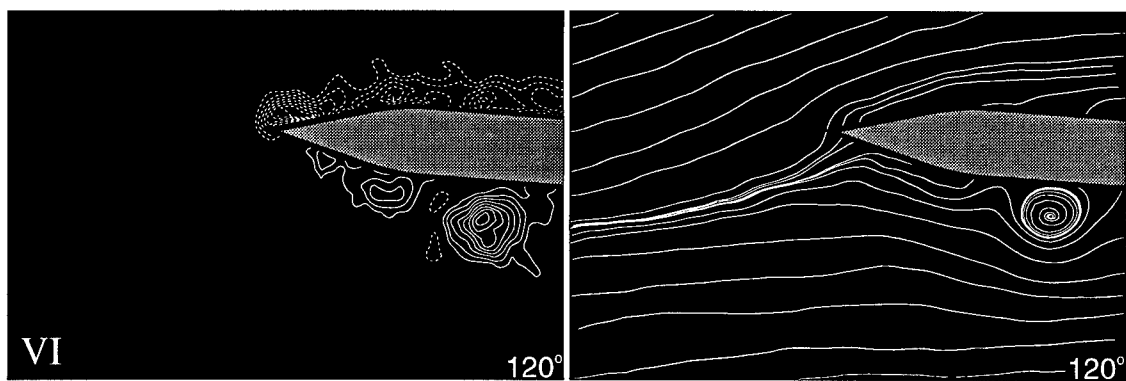
Figure 6.14: (Continued)
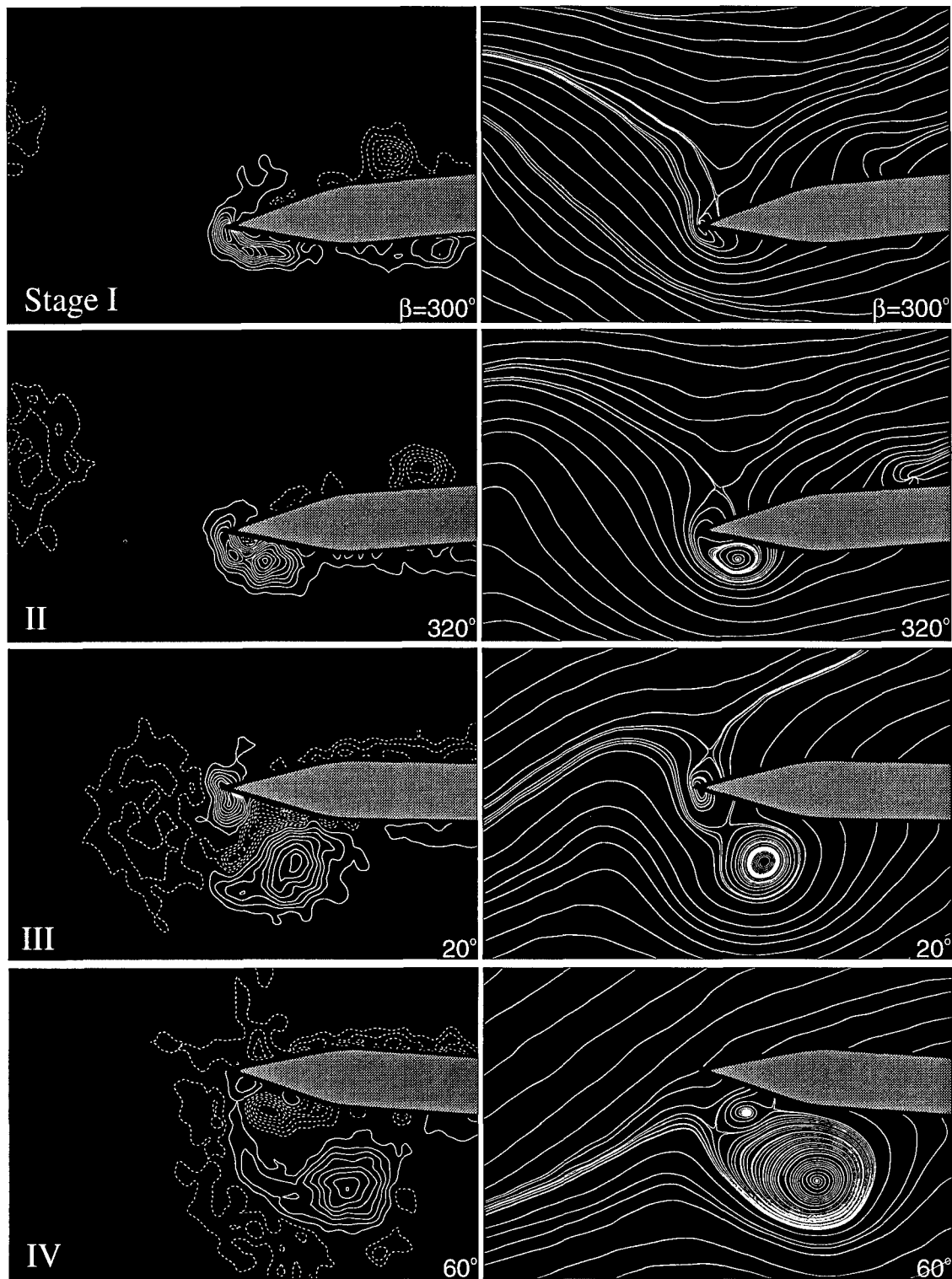
Figure 6.15: Instantaneous vorticity distributions and streamline patterns in the laboratory reference frame depicting the stages of tip vortex development for a leading-edge oscillating at $\phi=0°$ with respect to an incident clockwise vortex. $|\omega_{min}| = 5$ sec^{-1}; negative contour interval is $\Delta\omega = 5$ sec^{-1} and positive contour interval is $\Delta\omega = 10$ sec^{-1}. Re = 6,250.

143
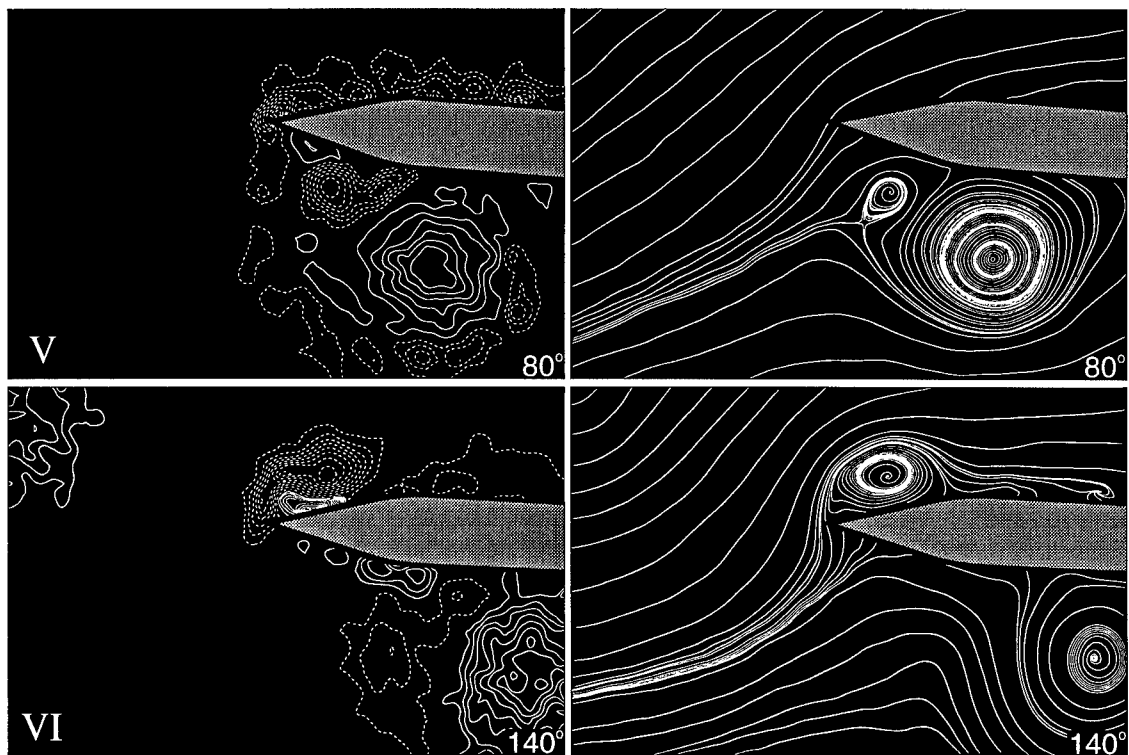
Figure 6.15: (Continued)
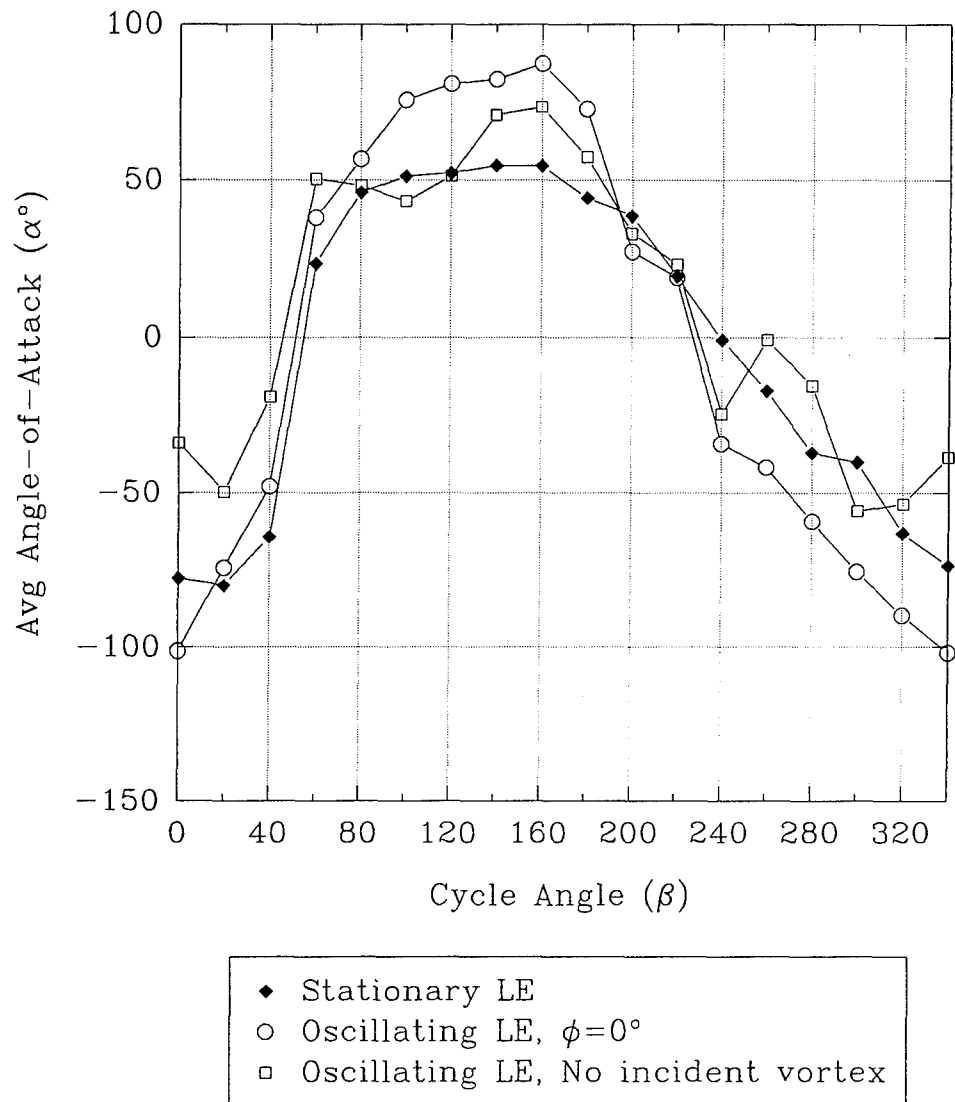
Figure 6.16: Average induced angle-of-attack at the tip of a leading-edge
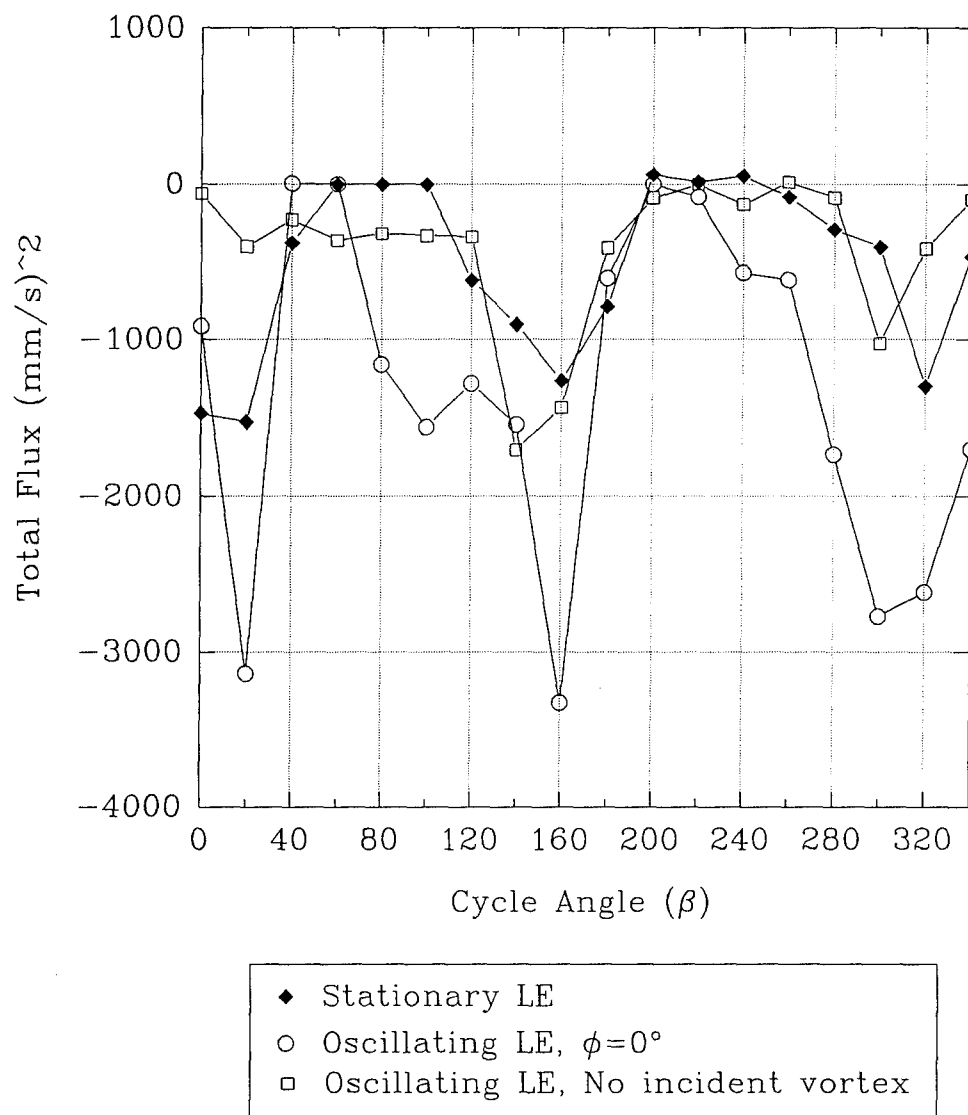
Figure 6.17: Total vorticity flux orthogonal to the line of symmetry of a leading-edge

7.0 CONCLUSIONS AND RECOMMENDATIONS

Interactions of a quasi-two-dimensional vortex with a stationary and an oscillating leading-edge were examined using a scanning laser version of high-image-density particle image velocimetry (PIV). This technique allows the instantaneous velocity field to be obtained over an entire plane with high spatial resolution and accuracy. Instantaneous streamlines and vorticity are calculated from the velocity field.

A NACA 0012 airfoil was oscillated sinusoidally about its leading-edge to produce a vortex street that impinged on the tapered leading-edge of a flat plate. The incident vortex street was observed to be phase-locked with the motion of the upstream airfoil, convecting past a stationary leading-edge at a reduced frequency equal to that of the oscillating airfoil. When the leading-edge of the downstream flat plate was oscillated at the same reduced frequency, the phase angle between the oscillating leading-edge and the incident vortex could be varied.

PIV images of the leading-edge region were obtained for two values of Reynolds number at specific time intervals over one cycle of either the incident vortex street or the oscillating leading-edge. At the lower Reynolds number, a well resolved time sequence of the interactions was obtained and allowed a better understanding of the flow physics.

7.1 Summary

The structure of the incident vortex, at mid-span, appears to remain two-dimensional within the core until it impinges the stationary leading-edge. When the leading-edge oscillates, however, three-dimensional structure is induced within the core while the vortex is still upstream of the edge. The convection speed of the incident vortex depends on whether the leading-edge is stationary or oscillating and varies as it approaches the edge. The velocity induced at the tip of the stationary leading-edge by

the approaching vortex closely matches the induced velocity of a leading-edge oscillating at an amplitude of 5 degrees without an incident vortex.

This investigation provides the first quantitative description of the distinctive features of the vortex-stationary edge interaction, including the approach, deformation and splitting of an incident clockwise vortex and the generation of tip and surface vortices on the lower surface of the leading-edge. When the incident vortex distorts around the tip, the portion passing below the surface of the edge is distended and fragmented by the development of the tip vortex. The portion of the incident vortex on the upper surface appears to roll along the surface as it convects downstream.

The circulation of the tip vortex attains a magnitude greater than that of the incident vortex. The circulation of the surface vortex increases as the circulation of the tip vortex grows, but its magnitude is always much less than the tip vortex. The manner in which the tip vortex splits into two vortices A and B implies that vorticity ceases to be fed into the tip vortex before splitting. The transient process associated with this cessation of vorticity flux may result in the two distinct vortices A and B. This hypothesis contrasts with the view that the surface vortex actually cuts off the supply of vorticity into vortex A.

The development, splitting and convection of the tip vortex and the formation of the surface vortex can be clearly seen for an oscillating leading-edge without an incident vortex. It appears that the vorticity flux from the tip region ceases prior to the occurrence of tip vortex splitting and that the surface vortex does not erupt into the external flow when the tip vortex splits. A nearly symmetric flow develops about the instantaneous $\alpha=0°$ position of the oscillating leading-edge.

Although similar in some ways to vortex interactions with the stationary leading-edge, the development of the tip and surface vortices is more intense for a leading-edge oscillating at $\phi=0°$ relative to an incident clockwise vortex. The circulation of the tip

148

vortex reaches nearly three times, and the surface vortex three-fourths times, the value of circulation of the incident vortex. At some instants, tip and surface vortices exist simultaneously on both the upper and lower surface of the leading-edge.

The tip vortex along the lower surface splits into two distinct vortices, A and B, at two different stages during interaction with the incident vortex. Vorticity continues to accumulate within the tip vortex when it first splits, but the vorticity flux ceases prior to the second split. These differences suggest that different mechanisms are involved each time the tip vortex splits.

When an incident clockwise vortex interacts with a leading-edge that is oscillating at $\phi=180°$, the incident vortex does not collide with the leading-edge, but convects above the upper surface. Moreover, the flow field near the leading-edge appears to depend on whether the influence of the leading-edge oscillation or the influence of the incident vortex dominates. At certain cycle angles, the observed flow field exhibits characteristics that suggest the two influences are balanced. Velocities induced by the incident vortex and the edge oscillation produce nearly symmetrical distributions of vorticity along the upper and lower surfaces. Consequently no tip vortex is formed. This suggests that at the tip, the velocity induced by the edge oscillation nearly cancels the velocity induced by the incident vortex.

For a sharp oscillating leading-edge, the general flow development and structure appear nearly independent of Reynolds number (Re). As may be expected, the most significant effect of Re is to alter the interaction of the tip vortex with the lower surface. A higher value of Re appears to advance the growth of the surface vortex which may cause early splitting of the tip vortex.

Vortex interactions with a stationary leading-edge are compared with those of an oscillating leading-edge without an incident vortex. The average measured velocity orthogonal to the line of symmetry of the leading-edge, and the induced angle-of-attack

149

for both cases varies sinusoidally, at the same frequency and phase, and corresponds to the movement of the stagnation line or saddle point from one surface to the other. The magnitude of the average orthogonal velocity at the tip of a stationary leading-edge varies with transverse position of the incident vortex. Furthermore, in both cases, if appears that the average orthogonal velocity is also significantly affected by the presence of a tip vortex.

The superposition of local circulation, total vorticity flux, average velocity and angle-of-attack from the interactions of a vortex with a stationary leading-edge, and an oscillating leading-edge without an incident vortex, is compared for a leading-edge oscillating at $\phi=0°$ and $\phi=180°$. Superposition is appropriate upstream of the leading-edge, where the flow is essentially inviscid. However, superposition does not predict magnitudes accurately where the effects of separation at the tip and the interactions of the tip vortex with the surface are prevalent.

Varying the phase angle of the leading-edge oscillation with respect to an incident clockwise vortex has a dramatic effect. In general, the flow structure and topology observed during vortex interactions with a stationary leading-edge are enhanced when the leading-edge oscillates at $\phi=0°$, and essentially attenuated when oscillating at $\phi=180°$. Similarly, the level of local circulation along the surface of the stationary leading-edge is amplified three times when the leading-edge oscillates at $\phi=0°$ and entirely disappears when oscillating at $\phi=180°$. The transverse position of the incident vortex is also observed to shift in a direction opposite to the motion of the edge, suggesting that the velocity field induced by the oscillating leading-edge has considerable upstream influence and causes the shift.

Six stages of tip vortex development were defined as a baseline during vortex interactions with a stationary leading-edge. Nearly all of the stages could be identified when the leading-edge oscillates without an incident vortex and at $\phi=0°$ relative to an

150

incident vortex. However, the vorticity distributions or topology of an identified stage often did not exactly match those of the baseline stage.

In general, the development of the tip vortex in the first three stages depends significantly on the incident flow field and the resulting production and flux of vorticity from the upper surface. The development of the tip and surface vortices for stages four through six depends more upon the local interaction between the individual vortices and the surface.

7.2 Implications for Unsteady Loading

Although the unsteady pressure field or force was not measured during this investigation, a relative assessment of the loading near the leading-edge may be implied, based on the results of other studies which did measure these forces. Ziada and Rockwell (1982) found the amplitude of the induced force on a sharp leading-edge increased with secondary vortex shedding. Moreover, Kaykayoglu and Rockwell (1985) determined that secondary vortex shedding from a sharp leading-edge caused the pressure field to be wave-like, with a maximum amplitude at the tip and different phase speeds along the upper and lower surfaces of the leading-edge.

In each of these earlier studies, the leading-edge was stationary and at $\alpha=0°$. Therefore, by relating the secondary vortex in these studies to the tip vortex formed during vortex interactions with a stationary leading-edge, implications for the vortex component of the force can be deduced for the present investigation. This approach suggests that the induced force on the stationary leading-edge is greatest when the incident vortex is split and the tip vortex distends the lower portion of the incident vortex. Consequently, the vortex-induced force on the edge will be much greater with the leading-edge oscillating at $\phi=0°$, and substantially reduced when the edge oscillates

151

at $\phi=180°$ with respect to the incident vortex. This suggests the phase angle of the leading-edge oscillation may be used to control the unsteady loading and noise generation resulting from vortex interactions.

7.3 Control of Vortex Interactions

If the existence of a tip vortex causes increased loading on the edge, then prevention of its development suggests that unsteady loading and noise will be reduced or eliminated. As noted previously, oscillation of the leading-edge at $\phi=180°$ with respect to the incident vortex suppresses the formation of a tip vortex in the stationary edge case. It appears that by oscillating the leading-edge at this phase angle, with the frequency of the convecting vortex street, and at the proper amplitude, the induced velocity from the motion of the edge balances the velocity induced by the incident vortex on the tip. Consequently, separation at the tip is avoided and the tip vortex never develops.

It is probable that this technique could be used to control quasi-two-dimensional interactions of a vortex of known strength, which occur at a known frequency. These type of "ideal" conditions may exist somewhat for blade-vortex interactions on a helicopter or wind turbine. However, it's obvious that a more robust method should be developed which may incorporate the essential features of varying the phase angle, but could be applied on a stationary leading-edge for any incident vortex, convecting at an arbitrary frequency.

The objective of such a method is to cancel the velocity induced by the incident vortex on the tip. This may be accomplished by using an array of orifices along the surface of a stationary leading-edge which may either inject or remove fluid. These orifices would produce a jet of variable velocity on the surface where the stagnation

152

point occurs, as the incident vortex approaches. These jets would be oriented normal to the chord of the airfoil and pulsed according to the frequency of vortex convection. The location of the stagnation point would be used as feedback to determine the velocity of the jets and their duration.

7.4 Recommendations for Further Study

This investigation did not incorporate direct measurement of the unsteady pressure or force. It would be beneficial to measure the unsteady force, while simultaneously acquiring the instantaneous velocity field of the stationary and oscillating flat plate, using PIV. This would allow direct correlation of the velocity and the induced force. Moreover, if the entire flat plate is visible within the PIV image, and the time resolution is sufficiently high, the unsteady force on the flat plate may be determined using the results of PIV and compared to the measured results. The force may be calculated using the approach of Lighthill (1986) or Howe (1989).

Investigating three-dimensional vortex interactions with a stationary and oscillating leading-edge, using PIV techniques, is another interesting extension of the present study. This could be accomplished first by replacing the parallel, rectangular flat plate in this investigation, with a swept flat plate. Following an assessment in that study of the effects of oscillation, a streamwise vortex could be generated that impinges on the original leading-edge. These studies would help clarify major unresolved issues involving instances of tail buffeting in high performance aircraft.

Finally, a PIV study using feedback to control the oscillation of the leading-edge for various frequencies of an incident vortex would establish the effectiveness of real-time control. Based on its success, an alternative control technique, such as proposed in the

previous section, could be applied to the leading-edge. The effectiveness of this approach could then be compared to the results obtained using an oscillating edge.

REFERENCES

Acharya, M. and Metwally, M. H., "Unsteady Pressure Field and Vorticity Production over a Pitching Airfoil," *AIAA Journal*, Vol. 30, No. 2, 1992, pp. 403-411.

Adrian, R.J., "An Image Shifting Technique to Resolve Directional Ambiguity in Double-Pulsed Laser Velocimetry", *Applied Optics*, Vol. 25, 1986, pp. 3855-3858.

Adrian, R.J., "Particle-Imaging Techniques for Experimental Fluid Mechanics", *Annual Review of Fluid Mechanics*, Vol. 23, 1991, pp. 261-304.

Booth, E.R., "Experimental Observations of Two-Dimensional Blade-Vortex Interaction," *AIAA Journal*, Vol. 28, August 1990, pp. 1353-1359.

Chong, M.S., Perry, A.E. and Cantwell, B.J., "A General Classification of Three-Dimensional Flow Fields", *Physics of Fluids A*, Vol. 2, 1990, pp. 765-777.

Doligalski, T.L., Smith, C.R. & Walker, J.D.A., "Vortex Interactions with Walls," *Annual Review of Fluid Mechanics*, Vol 26, 1994, pp. 573-616.

Gursul, I. & Rockwell, D., "Vortex Street Impinging upon an Elliptical Leading Edge," *Journal of Fluid Mechanics*, Vol. 211, 1990, pp. 211-242.

Hardin, J.C. and Lamkin, S.L., "Concepts for Reduction of Blade/Vortex Interaction Noise," *Journal of Aircraft*, Vol. 24, No. 2, 1987, pp. 120-125.

Horner, M.B., "An Examination of Blade-Vortex Interaction Utilizing Pressure Measurements and Particle Image Velocimetry", *Doctoral Dissertation*, University of Colorado, Boulder, Colorado, 1994.

Howe, M.S., "On Unsteady Surface Forces and Sound Produced by Normal Chopping of Rectilinear Vortex", *Journal of Fluid Mechanics*, Vol. 206, 1989, pp. 131-153.

Kaya, M.O., and Kaykayoglu, C.R., "Numerical Simulation of a Self-Sustained Wake-Edge Interaction", *Journal of Fluids and Structures*, Vol 10, 1996, pp. 215-236.

Kaykayoglu, C.R., "Active Control of a Mixing Layer by Upstream Influence from an Oscillating Edge", *Journal of Fluids and Structures*, 1989, pp. 1-16.

Kaykayoglu, R. & Rockwell, D., "Vortices Incident Upon a Leading Edge: Instantaneous Pressure Fields", *Journal of Fluid Mechanics*, Vol. 156, 1985, pp. 439-461.

Keane, R.D., and Adrian, R.J., "Theory of Cross-Correlation Analysis of PIV Images", *Applied Scientific Research*, Vol. 49, No. 3, 1992, pp.191-215.

Kelley, N.D., "Defining the Normal Turbine Inflow Within a Wind Park Environment," *NREL/TP-442-5619*, June 1993.

Kemp, N.H., "On the Lift and Circulation of Airfoils in Some Unsteady-Flow Problems", *Journal of the Aeronautical Sciences*, Oct., 1952, pp. 713-714.

Laursen, T.S., Rasmussen, J.J., and Stenum B., "Formation of a 2D Vortex Pair and its 3D Breakup: An Experimental Study", 1996.

Lighthill, J., "Fundamentals Concerning Wave Loading of Off-Shore Structures", *Journal of Fluid Mechanics*, Vol. 173, 1986, pp. 667-681.

Lin, J.-C., "NFILVB", software, Fluid Mechanics Lab., Lehigh University, 1994.

Lin, J.-C., "Bi-Linear Interpolation Program, BLINTP", software, Fluid Mechanics Lab., Lehigh University, 1995.

Lourenco, L.M., Krothapalli, A., and Smith, C.A., "Particle Image Velocimetry", *Advances in Fluid Mechanics Measurements, Lecture Notes in Engineering*, Vol. 45 (ed. M. Gad-el-Hak), Spring-Verlag, 1989, pp. 127-199.

Magness, C., "Streaming Function Generator, SFG", software, Fluid Mechanics Lab., Lehigh University, 1990.

Magness, C. and Troiano, J. "Automatic Laboratory Technician, ALT", Softwar, Fluid Mechanics Lab., Lehigh University, 1991.

Nakagawa, T., "On Unsteady Airfoil-Vortex Interaction," *Acta Mechanica*, Vol. 75, 1988, pp. 1-13.

Oschwald, M., Bechle, S., and Welke, S., "Systematic Errors in PIV by Realizing Offsets with the Rotating Mirror Method", *Experiments in Fluids*, Vol. 18, 1995, pp. 329-334.

Perry, A.E. and Steiner, T.R., "Large-Scale Structures in Turbulent Wakes Behind Bluff Bodies, Part 1. Vortex Formation Processes", *Journal of Fluid Mechanics*, Vol. 174, 1987, pp. 233-270.

Reuss, D.L., Adrian, R.J., Landreth, C.C., French, D.T., and Fansler, T.D., "Instantaneous Planer Measurements of Velocity and Large-Scale Vorticity and Strain Rate in an Engine Using Particle Image Velocimetry", *SAE Technical Paper 890616*, International Congress and Exposition, Detroit, MI, Feb. 27-Mar. 3.

156

Reynolds, W.C. and Carr, L.W., "Review of Unsteady, Driven, Separated Flows", *AIAA Paper No. 85-0527*, 1985.

Robinson, O., "ENSAV Post-Processing Software", Fluid Mechanics Lab, Lehigh-University, 1991.

Robinson, O., "V3 Post-Processing Software", Fluid Mechanics Lab, Lehigh-University, 1992.

Rockwell, D., "Unsteady Loading of Leading-Edges in Unstable Flows: An Overview," *AIAA Paper 84-2306*, October 1984.

Rockwell, D. and Lin, J.-C., "Quantitative Interpretation of Complex, Unsteady Flows via High-Image-Density Particle Image Velocimetry", *SPIE International Symposium on Optics, Imaging and Instrumentation*, San Diego, CA, July 1993.

Rockwell, D., Magness, C., Robinson, O., Towfighi, J., Akin, O., Gu, W., and Corcoran, T., "Instantaneous Structure of Unsteady Separated Flows via Particle Image Velocimetry", *Report PI-1*, Fluid Mechanics Lab., Lehigh University, Bethlehem, PA, 1992.

Rockwell, D., Magness, C., Towfighi, J., Akin, O., and Corcoran, T., "High Image-Density Partical Image Velocimetry Using Scanning Techniques", *Experiments in Fluids*, Vol. 14, 1993, pp. 181-192.

Rogler, H., "The Interaction between Vortex-Array Representations of Free-stream Turbulence and Semi-infinite Flat Plates," *Journal of Fluid Mechanics*, Vol. 87, 1978, pp. 583-606.

Schlichting, H., "*Boundary Layer Theory*", McGraw-Hill, 1968, pp 102-109.

Sears, W.R., "Some Aspects of Non-Stationary Airfoil Theory and Its Practical Application", *Journal of the Aeronautical Sciences*, Vol. 8, No. 3, 1941, pp. 104-108.

Seke, E., "PIV3", Interrogation Software, Fluid Mechanics Lab., Lehigh University, 1993.

Seke, E., "VCOR2", Vorticity Correlation Software, Fluid Mechanics Lab., Lehigh University, 1993.

Sheridan, J., Lin, J.-C., Rockwell, D., "Flow Past a Cylinder Close to a Free-Surface," Submitted to *Journal of Fluid Mechanics*, 1995

157

Shih, C., Ho, C-M, "Vorticity Balance and Time Scales of a Two-Dimensional Airfoil in an Unsteady Free Stream," *Physics of Fluids*, Vol. 6, No. 2, Feb. 1994, pp. 710-723

Shih, C., Lourenco, L.M. and Krothaplli, A., "Investigation of Flow at Leading and Trailing Edges of Pitching-Up Airfoil," *AIAA Journal*, Vol. 33, No. 8, 1995, pp. 1369-1376.

Smith, C.R., Walker, J.D.A., Haidari, A.H., Sobrun, U., "On the Dynamics of Near-Wall Turbulence," *Phil. Trans. R. Soc. London Ser. A*, Vol. 336, 1991, pp. 131-175.

Staubli, T. and Rockwell, D., "Interaction of an Unstable Planar Jet with an Oscillating Leading-Edge", *Journal of Fluid Mechanics*, Vol. 176, 1987, pp. 135-167.

Towfighi, J. and Rockwell, D., "Flow Structure from an Oscillating Non-Uniform Cylinder: Generation of Patterned Vorticity Concentrations", *Physics of Fluids*, Vol. 6, No. 2, 1994, pp. 531-536.

Tuncer, I. H., Wu, J.C., & Wang, C.M., "Theoretical and Numerical Studies of Oscillating Airfoils," *AIAA Journal*, Vol. 28, No. 9, 1990, pp. 1615-1624.

Visbal, M. R., and Shang, J. S., "Investigation of the Flow Structure Around a Rapidly Pitching Airfoil," *AIAA Journal*, Vol. 27, No. 8, August 1989, pp. 1044 - 1051

Visbal, M.R. and Gordnier, R.E., "Crossflow Topology of Vortical Flows," *AIAA Journal*, Vol 32, No. 5, 1993, pp. 1085-1087.

Vorobieff, P.V, "Trace-S", Software for Boundary Tracing and Particle Tracking, Fluid Mechanics Lab, Lehigh-University, 1994.

Vorobieff, P.V., "Multiple-Actuator Control of Vortex Breakdown On a Maneuvering Delta Wing and Related Issues of Flow Analysis and Topology", *Ph.D. Dissertation*, Lehigh University, 1996.

Wilder, M.C., "Airfoil-Vortex Interaction and the Wake of an Oscillating Airfoil," *Ph.D. Dissertation*, Virginia Polytechnic Institute and State University, 1992.

Ziada, S. & Rockwell, D., "Vortex-Leading-Edge Interaction", *Journal of Fluid Mechanics*, Vol. 118, 1982, pp. 79-107.

APPENDIX A: TREATMENT OF BOUNDARIES IN PIV DATA

A.1   Spatial Resolution of PIV

In a two-dimensional sense, fluid within an interrogation window is considered a single fluid element bearing one value of velocity. As particle images are interrogated into displacement vectors, the spatial resolution is limited by the interrogation window size and overlap ratio. According to the Nyquist criterion, the velocity field (in the physical plane) should be sampled on a grid which has a spacing (d_p) less than half the window size. In other words, the overlap should be no less than 50% (Reuss et al. 1989). Therefore, the grid size is one half of the window size. For example, an interrogation window size d_i=1.0 mm, with a magnification factor M=0.4, and an overlap ratio of interrogation P=50%, will yield a grid size in the physical plane, d_p=d_i(P/M)=1.25 mm. This corresponds to the smallest resolvable length scale in the velocity field. Thus it is imperative to keep in mind the order of magnitude of the structures of most interest when choosing values for these parameters.

In the region near a solid object, a thin layer develops which cannot be resolved unless the flow field is sufficiently magnified to resolve the extremely small length scales. In this investigation, the flow field near the leading-edge required a grid size larger than the boundary layer thickness. Consequently, only those velocities outside of the boundary layer, on the order of one grid size away, may be resolved. Furthermore, other factors such as the shifting of the boundary and low particle density adjacent to the surface of the boundary may add to the uncertainty of the flow field. However, specific steps were taken to overcome many of these uncertainties to obtain data as close to the boundary as the grid resolution will allow.

A.2 Treatment of Data Adjacent to the Boundary

The location of a surface in the image field usually does not coincide with the interrogation grid. Wherever the surface boundary intersects the grid, part of the interrogation window will lack particle images, and the cross-correlation calculation in PIV3 will be corrupted. This will influence the results of PIV, most likely causing an erroneous displacement vector.

The program TRACE-S enables the user to define the location of a boundary in the field of interest by tracing it with the cursor in the digitized image. The coordinates of this boundary are then stored in a file containing x-y pairs, which can be used as input to NFILV, as described in the next section. In addition, while viewing the file of particle images superimposed on the corresponding displacement vectors via TRACE-S, the user may select a window in which to invoke the manual particle tracking capabilities. If the start and end points of a particle path are selected, TRACE-S will calculate a displacement vector to be used as the average vector in that window. In this way, it is possible to retrieve information that exists close to a solid object, but could not be interrogated due to inadequate particle image density in the finite window size or to the effects of an image of the surface within the window which dominates the cross-correlation results. The traced boundary should delimit the area of the image which contains no PIV data.

In most cases, due to refraction and reflection from the surface and image biasing, the actual location of the solid body or free surface does not coincide with the aforementioned boundary. Thus, for purposes of presentation, it is also necessary have a clear definition of the physical boundary. Using TRACE-S, this can be traced from the center of a biased image, or a corresponding unbiased image.

160

A.3 Data Processing

With the boundary defined and any appropriate particle tracking performed to complete the field of measurable displacement vectors, the program NFILV is used to fill in any missing data via interpolation and to smooth the vectors to reduce the effects of noise in the image. In conjunction with this process, the boundary profile is used to exclude the area within the boundary from consideration in the interpolation of the velocity field. Inclusion of these values in the interpolation would be analogous to imposing a no-slip condition along a solid surface. In order to justify the application of such a boundary condition, the grid size would need to be an order of magnitude smaller than the boundary layer thickness. In this investigation, the grid size is larger than the boundary layer. Therefore, no boundary conditions are assumed.

A.4 Outline of Procedure

Based on the above discussion, it is possible to formulate an outline, as followed in the present research, for processing data containing a boundary in the field of interest.

(i) *TRACE-S*: From the digitized image, define the location of the solid boundary. Also define any region containing data considered unreliable, due to insufficient lighting or particle density.

(ii) *TRACE-S*: Employ manual particle tracking in the interrogation windows adjacent to the surface where clear particle traces are seen but erroneous displacement vectors have been calculated by PIV3. Examine the remainder of the flow field and discard any additional bad vectors here or in V3.

(iii) *NFILV*: Interpolate and smooth the vector field, specifying the boundary containing unreliable data as the region in which the data is to be ignored.

161

(iv) *Presentation*: Specify the spatial resolution, using the parameters described in sections 2.4 and B.1. Present the flow field with the location of the solid object clearly displayed, surrounded by a narrow band, void of data, to indicate the region of uncertainty. The thickness of this band will correspond approximately to one grid size.

APPENDIX B: CALCULATION OF VORTICITY AND CIRCULATION

B.1 Calculation of Vorticity

The interrogation program PIV3 actually determines the "displacement" field rather than the "velocity" field. The resolution of the digitizing process establishes the length scale of the image in millimeters. After interrogation, calculation of physical quantities such as velocity and vorticity are then carried out using the interpolation routine within NFILV. The velocity is obtained by specifying values of scanning frequency f_{sc}, magnification factor M and a unit conversion factor C, to scale the displacements obtained from PIV3. The velocity scale, $S_v=(f_{sc}/M)C$ is calculated and used as input to NFILV to convert the interrogation length scale to the physical scale of the flow. After conversion of length and velocity, vorticity is also calculated in NFILV according to

$$\omega = \frac{\partial v}{\partial x} - \frac{\partial u}{\partial y}, \text{ for grid points along a boundary or at a corner, or}$$

$$\omega = \frac{\oint \overline{u} \cdot d\overline{s}}{A}, \text{ for inner grid points,}$$

where u and v are the components of the velocity in the x and y-directions, respectively.

B.2 Calculation of Circulation

Circulation (Γ) is calculated by the in-house developed software, V3 and NV, and by the program CIRFLUX, used specifically in this investigation for determining local circulation. By definition, $\Gamma = \oint \overline{u} \cdot d\overline{s}$, where s is along the path of integration. If velocity and length are accurately converted into a physical quantity in NFILV, Γ will automatically bear a unit of L^2/sec, where L is the unit of length. In calculating

circulation, it should be noted that the circuit of integration must avoid boundaries of the velocity field in order to reduce error. Therefore, the local circulation cells did not extend completely to the indicated boundary (refer to figure 4.3) of the leading-edge but remained at least one grid away.

VITA

[redacted] In 1982, he graduated from Lewis-Palmer High School in Monument, Colorado, was awarded an Air Force ROTC scholarship, and began a degree program in Aerospace Engineering at the University of Colorado at Boulder. From 1983 to 1985, Rhett took a leave of absence from his studies to serve in the Venezuela-Caracas Mission of the Church of Jesus Christ of Latter-Day-Saints. On August 1, 1987, he married Melecia Moore of Niwot, Colorado. In May, 1988, he graduated with a B.S. degree in Aerospace Engineering and was commissioned a Second Lieutenant in the United States Air Force. Following completion of a M.S. degree, in Aerospace Engineering in 1989, Rhett entered active duty as an Airframe Aerodynamics Engineer in the Flight Dynamics Directorate of Wright Laboratory, Wright-Patterson AFB, Ohio. During his four years at the lab, he managed wind tunnel and flight tests to improve low-speed performance, stability and control of air vehicles using innovative aerodynamic control devices. More importantly, his experience also included the birth of his daughter Madison in 1990 and his son Garrett in 1993.

Rhett was assigned to the Civilian Institutions Program of the Air Force Institute of Technology in 1993 to earn a Ph.D. in the field of unsteady fluid mechanics at Lehigh University. After completing degree requirements, he will return to the Air Force way of life as an engineer in the Armament Directorate of Wright Laboratory at Eglin AFB, Florida. Rhett's publications include "Influence of a Rotating Leading-Edge in Accelerating Starting Flow Over an Airfoil", AIAA Paper 90-0583; "Robotic Air-to-Air Combat Vehicle: A Combat Force Multiplier", AIAA Paper 90-3283; "Cost Effectiveness of a Robotic Air-to-Air Combat Vehicle", Proceedings of the 1990 AIAA Missile Sciences Conference, Monterey, CA, Vol. 3; and "Interactions of a Vortex with an Oscillating Leading-Edge", submitted November 17, 1995 to *AIAA Journal*.